Multi-Parametric Fluorescence Computational Microscopy

by

Niklas Gahm

A dissertation submitted in partial fulfillment of the requirement for the degree of

Doctor of Philosophy

(Biomedical Engineering)

at the

UNIVERSITY OF WISCONSIN - MADISON

2022

Date of final oral examination: November 22nd, 2022

BME Thesis Committee:
Dr. Kevin Eliceiri (BME/MedPhys), mentor
Dr. Melissa Skala (BME)
Dr. Andreas Velten (BMI/ECE)
Dr. Mohit Gupta (CS)
Dr. Filiz Yesilkoy (BME)

Table of Contents

Acknowledgements

I would like to thank Dr. Kevin Eliceiri, Dr. Melissa Skala, Dr. Louise Pape, the Computational Informatics in Biology and Medicine program, and everyone at Morgridge and LOCI for the support I have received over the years for my research. More specifically, this research was supported by National Institutes of Health grants R44MH065724, R01GM102924, U54CA268069, and P41GM135019 and additional funding from the UW-Madison Graduate School, Morgridge Institute for Research, the Semiconductor Research Corporation, and the Chan Zuckerberg Initiative. The Bement Lab was funded by NIH grant GM052932. Matthew Larson was funded in part by the UW Medical Scientist Training Program. We wish to thank Jeff Stuckey, Dale Osterlie, Dan Daugherty, John Ritz and Michael Szulczewski of Bruker Nano Surfaces FM for useful testing, scanning firmware modifications and advice on the SSFC system. We acknowledge the efforts of Jayne Squirrell, Thomas R. Mackie. Julie Last, Trillian Gregg and Brian Burkel of LOCI and Elizabeth A. Harvie and Anna Huttenlocher of the Department of Medical Microbiology and Immunology for system use and project input. I also wish to thank Photometrics Inc. for assistance with cameras and the Bement, Heideman, Halberg, Schuler, and Otegui laboratories for specimens for imaging. Additionally we acknowledge the contributions of Dr. Paul Barber, Dasong Gao and Curtis Rueden to FLIMlib.

Dedication

Here's to my cat Freja, without whom I would have had to do a lot kml nbbbbbbbbbbbbbblmk nbbbbb less revisions, and to Moo who claims he helped ru6yhtegj55555ss, eafrdwxsiuhx,by sitting on my keyboard while I write this. And while those two chaos demons provide Serotonin, a significant thank you to friends and family who have helped keep me focused on writing more.

Abstract

(412/350)

The increased accessibility of processing power and emergence of novel computational methods has created opportunities for applications to imaging. Biological optical microscopy is a particularly good target for the application of these methods due to the speed and relative ease for adoption of new methods and magnitude of new information unlocked through methods as opposed to clinical imaging. Before computational power was readily accessible, microscopy was largely limited to what could be achieved through physics to generate human interpretable data at the eyepiece/camera. With this new computational power a emerging field of microscopy has opened up, namely computational microscopy. Wherein we are no longer only bound to physical hardware alone that produce human interpretable images, but rather can leverage any property of light and any light-sample interaction for data collection. Through the use of computational microscopy we can mathematically reconstruct human interpretable data from the raw data output by these specialized microscopes. To do this effectively requires a knowledge of image processing programming and algorithms, which are not often very accessible to the typical biologist that may have minimal training in these areas. This imaging expertise need requires technology translators with an understanding of software, hardware, and biology to develop tools to make these new and powerful computational microscopes accessible for researchers. To this purpose my thesis is significantly focused on developing processing algorithms that have easy to use interfaces to make accessing certain forms of computational microscopy easier for other researchers. For my thesis work, three primary types of computational microscopes were selected. First was the spectrally split swept-field confocal microscope. This methodology aims to build a data set of images with each image containing multiple spectral channels, similar to hyperspectral imaging, but with more background rejection. Second was the sequential erosion of tissue imaging microscope, which provides a high-speed and low-cost-optical and physical alternative to the previously published proposal of a microtome paired with a confocal microscope. It operates through using projected patterns from a digital light projector for background rejection through structured illumination. Finally, the third project is the real-time fluorescence lifetime imaging microscopy estimation system. This system is being integrated with our open source OpenScan acquisition system to provide an early warning system for potential artifacts or other problems in fluorescence lifetime imaging microscopy which has a notoriously long period of time between starting data collection and seeing the final results. These projects produced three unique tools for researchers to use to improve access to computational microscopy.

Chapter 1: Introduction

Optics

Optical Imaging Contrast

Ever since the invention of the first microscopes in the late 16th century, they have been intimately tied to biological applications. The first microscopes which were little more than improved magnifying glasses led to the discovery of cells in 1665 and bacteria in 1675 thereby revolutionizing medicine and how we see organisms [1–3]. Ever since then microscopes have been under development trying to push the bounds of how humans can interpret visual data and push the lower limit of imaging resolution further and further through physics [4–6]. With each advancement finer and finer details of biology and the world around us were revealed and more fields started to find usage for these devices. With metallurgy to study the composition of various materials and how their structures react under different stress conditions [7]. Or for the use of studying pigment composition and painting layers of art works [8–10]. While microscopy has expanded to other fields, its primary development and usage remains tied to biological and medical applications [4,6]. As microscopes developed, they not only pushed for better resolution, but also expanded into finding alternate modes of contrast than the standard brightfield. These contrast modes were developed from advances in optical physics and chemistry. From the optical physics development side, polarization was integrated into microscopy which enabled differentiating and visualizing the co-localization of structures that reflect or pass differently polarized light [11,12]. Furthermore polarization led to the development of Differential Interference Contrast (DIC) microscopy. This form utilizes constructive and destructive self interference to generate contrast that visualizes the combined changes to the light path caused by thickness and refractive index changes from the specimen [13–15]. From the chemistry side, the development of stains which altered the coloration of the sample and then later targetable stains provided a new form of contrast, namely spectral contrast, that was able to highlight specific cellular structures [16,17]. Notably stains such as Hematoxylin and Eosin, Gram, and Trichrome stains have found a permanent home in modern medicine [18–21]. Similar to staining in that it develops contrast from the sample, fluorescence was introduced to microscopy [22]. Fluorescence can be introduced to a sample through either staining or genetic modification which can specifically target cellular structures and genetic expression [23–31]. With the further development of sensitivity to fluorescence, auto fluorescence was discovered. Auto-fluorescence is the phenomena where certain biological molecules are inherently fluorescent without any modification [32]. Normally these molecules are only weakly fluorescent, but since they do not need any modification for fluorescence microscopy, they are very powerful [33]. They provide a snapshot into the exact localizations of these inherent molecules without any interference from sample preparation [34]. NADH and FAD are notable examples, since they are auto-fluorescent and deeply tied to the cellular metabolic process of all biological life [35–38]. While these forms of fluorescence provide spectral contrast they further provide another form of contrast. Specifically due to the inherent nature of the fluorescent molecules

there are differences in the time between excitation and emission, even for the same molecule dependent on the local microenvironment and protein bindings [39–41]. This is known as Fluorescence Lifetime Imaging Microscopy (FLIM) and is incredibly powerful to elucidate the details of biological processes in the cellular microenvironment [42–44]. All of these contrast methods provide insights into studies ranging from protein co-localizations, cellular structure changes, various marker detections, and more. With microscopy having been primarily a source of visual data, spatial information has classically been core to the technology.

Deep Imaging

Spatial information is incredibly useful to biologists since it provides sub-cellular information on tagged molecules locations within the larger structure of the cell, such that hypotheses can be tested on whether certain proteins interact with each other, are only expressed in specific cellular structures, or regulate aspects of structures [45,46]. Wherein there is interest in optically thick samples, since this can provide information across a larger scale and biological gradient than available in thin samples [47].

Thick samples are very difficult to image since there is an inherent imageable depth limit dependent on the light attenuation primarily due to the inherent scattering of the sample material [48]. Specifically, as light travels through the sample it can interact with molecules and structures that scatter some of the light at random angles, therefore the more material light needs to travel through, the more of the light is scattered [49]. Given that the deeper in a sample one tries to image, the more light is scattered by the material, and our collected intensity is therefore reduced. This primarily limits the maximal image depth. Furthermore, the maximal image depth is also reduced by the refractive index mismatch of the interfaces the collected light needs to pass through. Specifically the interfaces between the microscope objective and the imaging medium such as air, water, or oil, plus the interface between the imaging medium and the sample. Wherein some light is refracted by each interface out of the optical path thereby attenuating the intensity [50]. Additionally, thicker samples have an increased problem with out-of-field fluorescence. This refers to where the excitation light excites the fluorophores located above and below the focal plane, which will contribute to the captured signal, thereby reducing the Signal to Noise Ratio (SNR) of the collected image [22]. Out-of-field fluorescence is a significant problem and to address this, two modern microscopy methods have been developed, confocal and multiphoton microscopy [48,51–53]. Both of these are further discussed below, but in essence are centered around rejecting background light and only exciting the in-focus point . Though these methods do significantly improve the SNR, they are still constrained by light attenuation. Collectively within biological samples this results in a maximum depth from which we can collect useful spatial information of only around one millimeter from the sample surface, meaning we effectively can only capture superficial information of the sample [48,54].While both these methods reduce or fully eliminate out-of-field fluorescence, they do not directly address the issue of light attenuation.

Sectioning

To address this need for deeper imaging both physical sectioning and optical sectioning based techniques have been proposed as separate solutions and more recently as possible combined strategies. Physical sectioning generally sequentially removes thin slices from the sample which are then imaged to build a three-dimensional image [55]. This method can image whole thick-tissue samples, but it still suffers from the inherent issue of needing to register the images between slices for three dimensional reconstruction, and out-of-focus fluorescence [55]. Alternatively, optical sectioning with structured illumination can be used to reject out-of-focus light thereby providing better SNR in the imaged plane [56]. These approaches do not require registration between images, since the XY position is not altered between images, but are limited by the maximal physical imaging depth since they do not remove the physical material between the sample's top surface and the focal plane [57]. Therefore, by combining these two sectioning approaches a whole thick-tissue can be imaged without having problems with out-of-focus fluorescence and running into a maximal imaging depth but does still retain the inherent problem of requiring registration between sequential images [57–59]. As such it is of interest to develop accessible open-source computational imaging versions that improve the quality of the available spatial information in depth that require minimal registration. This is further developed in Chapter 3.

Confocal

Confocal microscopy inserts a pinhole mask into the emission optical path at an aperture plane, thereby eliminating off-axis light which is coming from out-of-field fluorescence [48,55]. This does have the drawback that since light is being rejected post-excitation, the collected intensity from the imaged focal plane is reduced since some of that light is also being rejected. Meaning we need to increase the brightness of our illumination to get an equivalent brightness on our image. This paired with the need to scan the sample leads to an increased risk of photo-bleaching in the sample [48].

Multiphoton

An improvement on confocal microscopy is multiphoton microscopy [51]. Multiphoton microscopy leverages the phenomenon of two-photon absorption [60]. Specifically, a fluorophore can absorb either a single photon with a certain excitation energy, or simultaneously absorb two (or more) photons that are each half (or a third, etc.) of the excitation energy [60]. This double absorption event only occurs when there is a high-concentration of photons at a point, which in microscopy occurs at the focal point of the objective. Meaning that double photon absorption and the resultant fluorescence is effectively limited to a small area at the focal point of the objective with no out-of-field fluorescence [52].

Fluorescence

Fundamentals

Optical Microscopy has experienced a major revolution in the last 25 years with the advent of significantly advanced optical imaging technology from classical brightfield microscopes to highly advanced approaches like super resolution microscopy [61]. In particular fluorescence imaging has been significantly expanded and developed since it is capable of correlating phenotypic function and genetics [62,63]. This has led to the usage of fluorescence microscopy in a wide number of biological research areas including cancer biology, cell trafficking, and pathogenetic studies [63–67]. Given the importance of this method, I have focused my thesis work on developing improved computational imaging methods to exploit the contrast gained from fluorescence [68]. Fluorescence utilizes an external light source to illuminate a sample with fluorescent molecules in it. These molecules can be intrinsic to the sample such as NADH or FAD auto-fluorescence, fluorescence probes genetically tagged to a protein such as GFP, or a fluorescent stain for structural contrast such as Texas Red fluorescent dye [23,29,35].

When these molecules are hit with photons of specific energies they can absorb the photon, thereby exciting electrons into a higher energy state which is a higher electron orbital [69]. Wherein, the excited electrons will return to their ground state over time which is the basis for our contrast through fluorescent lifetime information. This source of contrast can be measured through Fluorescence Lifetime Imaging Microscopy (FLIM) as introduced below and its useability is further developed in Chapter 4 [70]. In the process of returning to the ground state the electron will go through multiple energy levels which are the electron orbitals in the same orbital group the electron releases the excess energy as radiative heat, but when it jumps down between orbitals the excess energy can be radiated as a photon of lower energy than the absorbed photon. Meaning the emitted light is of a longer wavelength than the illumination wavelength [69]. This difference in photon energy is known as the Stoke's shift and enables many fluorescence microscope designs since a dichroic mirror based on wavelength can be used to branch the optical arms [71]. Unfortunately, this process cannot be repeated indefinitely before the fluorescent molecule is damaged. This leads to an effect known as photo-bleaching when a fluorescent sample has been exposed to enough light that it cannot fluoresce anymore [30,72].

This also provides us with valuable information that can be used as contrast, namely contrast through emitted spectra. This is commonly leveraged through hyperspectral imaging systems and fluorescence microscopes that do sequential imaging with different emission filters to image only specific wavelengths [73]. This source of contrast is further developed in Chapter 2. Additionally, the relative intensity and location of imaged fluorophores provides structural information and relative fluorophore density within our field of view. This is further developed in Chapter 3.

Common Fluorophores

To leverage contrast through spectra, a sample needs to include multiple fluorophores of either unique emission or unique excitation wavelengths. The two methods operate separately in terms of how the individual signals are split. For a set of unique emission spectra, the fluorescent signal has to be split either through a series of dichroics picking off wavelengths or being spread out with a prism then imaged in a point scanning or line-scanning system [54]. This puts more hardware requirements on the collection arm of a microscope. Conversely a set of fluorophores with unique excitation spectra can be imaged by encoding the unique signals temporally [53]. Meaning that different wavelengths of light are used sequentially to illuminate the sample and an image is captured for each illumination. This requires synchronization between the camera and a light source capable of producing multiple wavelengths. Given the correct hardware, these methods can even be combined to enable usage of more fluorophores in a sample. These fluorophores can be used in a vast range of applications. Notably fluorophores such as Green Fluorescent Protein (GFP), Red Fluorescent Protein (RFP), and Blue Fluorescent Protein (BFP) can be used as genetic markers since they are DNA strings that can be inserted through CRISPR and other methods at specific locations in genomes [24–26,74,75]. This in turn means that the respective fluorescent protein will only be produced if the tagged section is expressed [24,27,76]. Additionally fluorophores such as Alexa Fluor, Texas Red, and fluorescein isothiocyanate (FITC) can be conjugated to proteins and antibodies which are used to target specific cell types and structures, thereby showing the presence and structure of their conjugate [29,31,77–80]. It is further notable that some fluorophores have different fluorescent lifetimes depending on what their conjugate is bound to which enables an additional source of contrast and discrimination between micro-environmental states.

Fluorescence Lifetime Imaging Microscopy (FLIM)

FLIM has seen increased adoption by biologists in recent years as quantitative sensing of the state of cellular micro-environments spatially and temporally [39,81]. While fluorescence lifetime has previously been used by chemists to detect the pH of a micro-environment, the binding state of a molecule, and more, FLIM provides imaging based information of the spatial distribution of these metrics within a sample [81,82]. To explore the cellular microenvironment in a label free manner using intrinsic fluorescence, there has been significant research centered around the autofluorescent redox ratio (NADH/FAD) of cells which can be further separated into the bound and unbound states and delve into Fluorescent Lifetime Imaging Redox Ratio (FLIRR) [82,83]. This metric is currently being utilized as an indicator of glycolytic versus oxidative energy states of a cell [83]. Further work has been done to improve the redox ratio metric and embed more lifetime information into it, this led to the development of the Optical Metabolic Index [84].

Paired with the increasing computational power available in modern computers, the lifetime imaging collection hardware has steadily shifted from being fully on a single expensive board that does all image capture processing and then reads out the image to the computer; to being able to stream the collected data in a First In, First Out (FIFO) manner to the attached computer which builds the collected image. In particular, this is a shift for researchers using a technique

known as Time Correlated Single Photon Counting (TCSPC). This technique typically uses specialized hardware which is capable of counting the number of photons arriving in picosecond intervals [85]. These intervals are small enough that they can capture the effective time between excitation, peak emission, and capture the shape of the emission time distribution of individual fluorophores. Thereby researchers can capture how long a fluorophore takes from excitation to emission and separate spectrally similar fluorophores based on how long it takes for them to emit [86].

FLIM has also been approached from a frequency-domain direction, which encodes a fluorophore's lifetime in the phase shift and modulation of the emitted intensity relative to a pulsed light source [87]. By modulating/gating the imaging sensor with the same pulse frequency as the light source but shifting the phase of the imaging sensor gating relative to the light source, a curve of phase vs counts is captured. The peak of this curve is the phase of the fluorophore lifetime and can be used to calculate the modulation of the fluorophore as well [40]. While this approach is powerful, for biological imaging applications more hardware development and commercial availability has gone into the development of TCSPC [88,89]. Furthermore, the collected frequency and modulation information can be calculated from raw time data, thereby enabling the application of frequency-domain processing to time-domain collected data [90].

Unfortunately most current FLIM analysis frameworks are highly dependent on the underlying collection hardware. This means that from a user perspective their workflow will involve a third party proprietary algorithm from the same manufacturer as the hardware for data processing. Specifically, these systems have a workflow of the user viewing a real time image of the total fluorescence intensity as would be captured by classical fluorescence microscopy. This intensity image is used to find a focal plane and a Field Of View (FOV). Once this FOV is found and in focus the user sets up the FLIM parameters and sets the system to collect. Unfortunately, this collection is done completely blind. Meaning, the user has no idea whether there are differentials in the lifetime of fluorophores within the FOV. The user will collect this data and then in post-analysis find out if there were lifetime differentials [70]. Wherein it should be noted the collection of differences between fluorophore lifetimes is primarily dependent on the resolution and number of time gates used. There are empirical limits on the smallest lifetime available wherein the detector noise plays a critical role [91]. With the acquired raw data collected, the user feeds it and the imaging parameters used into a 3rd party proprietary algorithm. Due to the proprietary nature of the algorithm it is completely black box and non-extendable meaning that users cannot build further analysis into the software nor experiment with the processing pipeline for artifact correction etc. These algorithms are typically centered around Levenberg-Marquardt (LM) model fitting which separately operates on each pixel in the FOV. The time data from each pixel has Poisson curves fit to it using a non-linear least squares approach defined in LM. Each fitted curve is then used to calculate the lifetime and amplitude [92–94]. As such all these factors combine to the fact the user has no knowledge whether they have usable lifetime data until after collection once they have performed post-analysis. Due to this, frequently data sets need to be discarded since the imaging parameters were not tuned to the sample. Therefore, there is a strong need for FLIM microscopy methods to have not only a processing framework that functions across multiple hardware acquisition platforms, but also a real time viewfinder

display that can quickly estimate a resultant FLIM lifetime image directly built into the acquisition software. Wherein a viewfinder display ideally has fast enough processing that it operates at close to the acquisition rate of a given system and displays not only the current FOV of the microscope, but also estimates of the metrics that will be collected.

Spectral Analysis

One commonly used method to gain information about structure and co-localization of proteins is by imaging fluorophores of different emitted wavelengths and collecting those emissions separately, then combining the raw images into one image with each raw image representing a different wavelength [95]. This is commonly done by changing the excitation wavelength used to excite different fluorophores and switching filters in the emission collection path to only collect the light emitted by the selected fluorophore [96]. This effectively separates the fluorophores but is inherently slow due to needing to physically switch a filter to the point that fast biological events cannot be captured since the temporal resolution of the hardware is limited so severely by the physical switching [97]. To get around this slow-down various approaches have been used such as utilizing a prism or grating to spread the spectral information across the imaging sensor [73,98]. While effective, this requires scanning a single line across the sample in what is known as a pushbroom approach while the imaging sensor collects a raw image at each line position, and then reconstructs the field of view from the raw images [99]. Similarly, to improve image sensor readout speeds, there are approaches which use a line-detector (i.e. one dimensional imaging sensor) and then scan a single point across the sample in what is known as a whiskbroom approach [100]. While scanning a line or point across the sample is faster than switching filters, it is still not ideal. Therefore other approaches are focused on encoding spectral information in other ways. A common approach is to encode the spectral and spatial information into the captured image via patterning which can then be separated through a mathematical transform. This approach does not require any component to move physically during imaging, but rather is centered around projecting sequential patterns (generated by a Spatial Light Modulator (SLM) or Digital Micromirror Device (DMD)) [73,101]. Wherein, most modern SLMs utilize an array of liquid crystal elements which can be individually addressed to turn dark, thereby generating a pattern mask which can be added into the optical path [102,103]. DMDs on the other hand operate through an array of miniature mirrors where each can either reflect incident light on or off the optical path, thereby generating a pattern by selecting which mirrors are reflecting on the optical path [104]. These methods necessitate the capture of multiple raw images and significant processing to transform the raw images into usable images [101]. Collectively any form of hyperspectral microscopy requires some form of post-processing spectral unmixing to separate the fluorophores [105]. Wherein if the fluorophores are known a priori this can be done using multivariate curve fitting [106]. These a priori methods can be extended via machine learning into being blind to the underlying fluorophores where the method learns the spectral curves of unknown fluorophores, but in turn runs into the machine learning problem of requiring a lot of images [107].To avoid both the necessity for a priori knowledge and a lot of images per sample, a brute-force approach that uses all the spectral data collected to estimate not only how many fluorophores are present, but also their relative spectra assuming an effectively Gaussian distribution to estimate reasonable

spectral thresholds between fluorophores can be utilized. While this presents highly useful spatial information it is still limited by the inherent optical properties of the sample.

Computational Optics

While these above described microscopy methods are very powerful, they all can be further improved through integration of computational methods. Computational methods have been integrated into biological and clinical imaging for years, notably in the forms of Magnetic Resonance Imaging (MRI) and Computed Tomography (CT) [108–111]. These methods exemplify the field of computational imaging since they require intensive processing to convert raw data into human interpretable formats. Computational Imaging also contains the sub-field of Computational Optics which is focused on all light based computational imaging. These methods retain the need for intensive processing of raw data for the production of human-interpretable data. This includes methods such as Light Detection and Ranging (LIDAR) which uses light to sense the surrounding 3D environment [112,113]. While Computational Microscopy is included within Computational Optics, it focuses specifically on the integration of computational methods with microscopes.

Computational Microscopy

With the ever increasing computational power available to researchers, there have been multiple new and interesting ways to leverage that for system control and image analysis from denoising to segmentation and reconstruction problems [57–59]. A key factor of computational microscopy is the consideration of the whole life cycle of a data set from collection to final processing within the hardware design. To this end most computational microscopes leverage some interesting combination of mathematics and optics to enable data capture that is not accessible through traditional microscopy. Within the field there are multiple application examples such as lensless imaging which heavily utilizes deconvolution of the point spread function of captured light and uses no optical lenses at all or approaches for generating super-resolution images through photo-activated localization microscopy (PALM) [114,115]. All of these methods are reliant on computational power to generate an image from the raw data, and as such tend to each have their own unique processing software. Some of which even go so far as to do runtime analysis to effectively provide the user a live view of the sample as an optical image rather than blind collection of the raw images and then processing them into an optical image [116]. This presents an inherent problem for transferability and wide-spread adoption of these computational microscopy approaches. There are some open source software frameworks such as OpenScan, μManager, FIJI, and KNIME which have been used in multiple computational microscopy platforms [117–120]. All these open-source frameworks have a few key factors in common, particularly, that their underlying code is not only available to a user, but also has no barriers to deployment. Meaning that open-code software that is implemented in a commercial framework such as MATLAB has an inherent barrier to deployment since it requires the user to possess a MATLAB license or to put in work to transfer the MATLAB code to a different language [121]. While these open source frameworks do cover many imaging applications, there are some emerging imaging modalities such as Fluorescence Lifetime

Microscopy (FLIM) (Chapter 4) where computation needs improved implementation and performance.

Programming Methods/Tools

Image Analysis

All the computational microscopy methodologies described are heavily reliant on processing of the acquired raw data. As such, these approaches tend to heavily leverage code developed specifically for the methodology rather than a more general framework. But, once the raw data has been processed this data can be treated as regular microscope images and further analyzed with readily available open source image analysis tools such as CellProfiler, CellTracker, MATLAB, and FIJI [119,121–123]. These tools and many others all permit quantitative analysis of the captured images. Furthermore, they allow direct manipulation of the images to perform adjustments such as brightness and contrast adjustment to help visualize the data in a more human interpretable manner.

MATLAB

Wherein MATLAB forms a particularly useful tool as a testing ground for new algorithmic image based processes since it is primarily focused on operating on whole matrices rather than needing to operate on each individual line sequentially [124]. By treating images as matrices we can leverage this capacity to quickly test various methods and approaches to determine which is optimal for our needs. Furthermore MATLAB has a large user base and support which means there are plenty of libraries, functions, and plugins already available for use [125]. Because of this MATLAB was used for prototyping the algorithms used in the SSFC (Chapter 2), SETI (Chapter 3), and RT-FLIM (Chapter 4) projects. Unfortunately while MATLAB scripts can be open-source, the framework as a whole is not. Therefore, while it is a convenient testing ground, more promising image processing accessibility lies with open-source frameworks such as the ImageJ ecosystem or Python code [126–131].

Python

As an open source framework, Python has rapidly become the emerging tool of choice for scientific processing. It's aimed at being a high-level dynamically typed programming language that works to avoid the forced syntax that other prominent languages have to decrease the barrier to entry [130,132]. Because of this it has become prominent for use with scientific data and many incredibly useful open-source libraries have been developed for it such as scikit and Napari [133,134]. Both of which enable faster and better processing and viewing of data. Both of these libraries are utilized in the RT-FLIM project (Chapter 4) for the actual implementation of the viewfinder [135]. Additionally there has been significant work done to make other programming and analysis frameworks accessible from within Python. Notably MATLAB, R, and ImageJ are accessible [131,136,137]. The cross accessibility to ImageJ through PyImageJ is of interest since it significantly expands ImageJ's capabilities which can be leveraged for scripting

[126,131]. This is leveraged in the Image Processing Tools in ImageJ Scripting (Chapter 5) project.

ImageJ/FIJI

Of particular interest is FIJI, since it is a distribution package of ImageJ which bundles multiple useful functionalities into one ready to go distribution that is one of the most widely used biological imaging software packages [63,138]. In particular this software is highly interesting from the perspective of method sharing, since the underlying ImageJ framework was always focused on extensibility via toolkits/plugins and being open source [138].

ImageJ has grown and eventually developed the FIJI distribution, FIJI is centered around being a parts-included variant for microscopy image analysis. This framework has enabled ready access to image processing for programmers, bench biologists, and non-programmers alike [63,138]. It to this day is open source and highly extensible, meaning much of the processing code that is currently highly specific to individual microscope methodologies can be integrated and this framework can encompass the processing pipeline from raw data to post-analysis [139]. With the further benefit that by integrating these methodologies into an open source framework other researchers can improve upon them, giving all an ever improving image processing approach. While this is highly promising and is starting to be implemented in a few approaches, it requires strong computational and imaging knowledge to actually transfer. Therefore while FIJI is used in all of my projects, it was utilized primarily for the final image presentation for Chapters 2-4. It is explored in depth in the Image Processing Tools in ImageJ Scripting (Chapter 5) project that I was lead author on. As further development works on integrating more and more methodologies within the ImageJ/FIJI framework through macros and plugins, additional frameworks have started popping up to assist with this process in a more high-level fashion, which are focused on workflow integration for data science and are capable of interfacing across multiple frameworks and programming language to bind raw data, processing code, and post-processing analysis into one workflow [138,140].

MicroManager

Another particularly interesting variant building off of ImageJ is MicroManager. MicroManager utilizes the core mechanics of ImageJ and interfaces with hardware directly, thereby forming a steering framework that can be used to control most microscopes [118,141]. This is an open-source framework, with a programming interface, so not only can it be used to operate microscopes, but also to automate them. Automation is particularly useful for computational microscopy, since many of the methodologies require multiple images to be collected with specific conditions to form a single image. Therefore if any form of raster scanning is desired, automation removes the issue of human error invalidating a given frame since some detail did not get set right for an individual sub-image [142–144]. Automation through scripts provides a further benefit of enabling code sharing so specific imaging modalities can be readily transferred between similar systems. MicroManager has been further expanded as the basis for OpenScan which is specifically aimed at operating fluorescence lifetime imaging microscopes [117]. This open source usage is further explored in Chapters 3 and 4.

All of this is centered around building an array of tools that can ideally readily address the specific needs of a biologist or medical expert wanting to gather data on some specific structure, protein location over time, growth over time, other biological markers, or some combination thereof. Wherein we want to integrate the frameworks we develop into FIJI and MicroManager such that they are readily shareable between researchers.

Chapter 1 References

1. Lawson I. Crafting the microworld: how Robert Hooke constructed knowledge about small things. Notes Rec R Soc J Hist Sci. 2016 Mar 20;70(1):23–44.
2. Gest H. The discovery of microorganisms by Robert Hooke and Antoni van Leeuwenhoek, Fellows of The Royal Society. Notes Rec R Soc Lond. 2004 May 22;58(2):187–201.
3. Lane N. The unseen world: reflections on Leeuwenhoek (1677) 'Concerning little animals.' Philos Trans R Soc B Biol Sci. 2015 Apr 19;370(1666):20140344.
4. Croft WJ. Under The Microscope: A Brief History Of Microscopy. World Scientific; 2006. 153 p.
5. Singer C. Notes on the Early History of Microscopy. Proc R Soc Med. 1914 May;7(Sect_Hist_Med):247–79.
6. La Berge AEF. The History of Science and the History of Microscopy. Perspect Sci. 1999;7(1):111–42.
7. Borrajo-Pelaez R, Hedström P. Recent Developments of Crystallographic Analysis Methods in the Scanning Electron Microscope for Applications in Metallurgy. Crit Rev Solid State Mater Sci. 2018 Nov 2;43(6):455–74.
8. Best SP, Clark RJH, Withnall R. Non-destructive pigment analysis of artefacts by Raman microscopy. Endeavour. 1992 Jun 1;16(2):66–73.
9. Clark RJH. Raman microscopy: application to the identification of pigments on medieval manuscripts. Chem Soc Rev. 1995;24(3):187.
10. Hernanz A, Mas M, Gavilán B, Hernández B. Raman microscopy and IR spectroscopy of prehistoric paintings from Los Murciélagos cave (Zuheros, Córdoba, Spain). J Raman Spectrosc. 2006;37(4):492–7.
11. Inoué S. Polarization Microscopy. Curr Protoc Cell Biol. 2002;13(1):4.9.1-4.9.27.
12. Israel Y, Rosen S, Silberberg Y. Supersensitive Polarization Microscopy Using NOON States of Light. Phys Rev Lett. 2014 Mar 12;112(10):103604.
13. Pluta M. Nomarski's DIC microscopy: a review. In: Phase Contrast and Differential Interference Contrast Imaging Techniques and Applications [Internet]. SPIE; 1994 [cited 2022 Nov 12]. p. 10–25. Available from: https://www.spiedigitallibrary.org/conference-proceedings-of-spie/1846/0000/Nomarskis-DIC-microscopy-a-review/10.1117/12.171873.full
14. Cogswell CJ, Sheppard CJR. Confocal differential interference contrast (DIC) microscopy: including a theoretical analysis of conventional and confocal DIC imaging. J Microsc. 1992;165(1):81–101.
15. Fu D, Oh S, Choi W, Yamauchi T, Dorn A, Yaqoob Z, et al. Quantitative DIC microscopy using an off-axis self-interference approach. Opt Lett. 2010 Jul 15;35(14):2370–2.
16. Bordoloi B, Jaiswal R, Siddiqui S, Singh RB. A HISTORY OF EVOLUTION OF SPECIAL STAINS. 2017;(2456):9.

17. Alturkistani HA, Tashkandi FM, Mohammedsaleh ZM. Histological Stains: A Literature Review and Case Study. Glob J Health Sci. 2016 Mar;8(3):72–9.
18. Titford M. The long history of hematoxylin. Biotech Histochem Off Publ Biol Stain Comm. 2005 Apr;80(2):73–8.
19. Foot NC. The Masson Trichrome Staining Methods in Routine Laboratory Use. Stain Technol. 1933 Jan 1;8(3):101–10.
20. Kopeloff N, Beerman P. Modified Gram Stains. J Infect Dis. 1922;31(5):480–2.
21. Lauer BA, Reller LB, Mirrett S. Comparison of acridine orange and Gram stains for detection of microorganisms in cerebrospinal fluid and other clinical specimens. J Clin Microbiol. 1981 Aug;14(2):201–5.
22. Stelzer. Contrast, resolution, pixelation, dynamic range and signal-to-noise ratio: fundamental limits to resolution in fluorescence light microscopy. J Microsc. 1998 Jan;189(1):15–24.
23. Prasher DC, Eckenrode VK, Ward WW, Prendergast FG, Cormier MJ. Primary structure of the Aequorea victoria green-fluorescent protein. Gene. 1992 Feb 15;111(2):229–33.
24. Chalfie M, Tu Y, Euskirchen G, Ward WW, Prasher DC. Green Fluorescent Protein as a Marker for Gene Expression. Science. 1994 Feb 11;263(5148):802–5.
25. Lee S, Lim WA, Thorn KS. Improved Blue, Green, and Red Fluorescent Protein Tagging Vectors for S. cerevisiae. PLOS ONE. 2013 Jul 2;8(7):e67902.
26. Chalfie M. Green Fluorescent Protein. Photochem Photobiol. 1995;62(4):651–6.
27. Remington SJ. Green fluorescent protein: A perspective. Protein Sci. 2011;20(9):1509–19.
28. Mauring K, Krasnenko V, Miller S. Photophysics of the blue fluorescent protein. J Lumin. 2007 Jan 1;122–123:291–3.
29. Titus JA, Haugland R, Sharrow SO, Segal DM. Texas red, a hydrophilic, red-emitting flourophore for use with flourescein in dual parameter flow microfluorometric and fluorescence microscopic studies. J Immunol Methods. 1982 Apr 29;50(2):193–204.
30. Demchenko AP. Photobleaching of organic fluorophores: quantitative characterization, mechanisms, protection*. Methods Appl Fluoresc. 2020 Feb;8(2):022001.
31. Lindhoud S, Westphal AH, Visser AJWG, Borst JW, Mierlo CPM van. Fluorescence of Alexa Fluor Dye Tracks Protein Folding. PLOS ONE. 2012 Oct 8;7(10):e46838.
32. Andersson H, Baechi T, Hoechl M, Richter C. Autofluorescence of living cells. J Microsc. 1998 Jul 1;191(Pt 1):1–7.
33. Monici M. Cell and tissue autofluorescence research and diagnostic applications. In: Biotechnology Annual Review [Internet]. Elsevier; 2005 [cited 2022 Nov 12]. p. 227–56. Available from: https://www.sciencedirect.com/science/article/pii/S1387265605110072
34. Wong Kee Song LM, Banerjee S, Desilets D, Diehl DL, Farraye FA, Kaul V, et al. Autofluorescence imaging. Gastrointest Endosc. 2011 Apr 1;73(4):647–50.
35. Bartolomé F, Abramov AY. Measurement of Mitochondrial NADH and FAD Autofluorescence in Live Cells. In: Weissig V, Edeas M, editors. Mitochondrial Medicine [Internet]. New York, NY: Springer New York; 2015 [cited 2021 Dec 1]. p. 263–70. (Methods in Molecular Biology; vol. 1264). Available from: http://link.springer.com/10.1007/978-1-4939-2257-4_23
36. Gorbunova IA, Sasin ME, Golyshev DP, Semenov AA, Smolin AG, Beltukov YM, et al. Two-Photon Excited Fluorescence Dynamics in Enzyme-Bound NADH: the Heterogeneity of Fluorescence Decay Times and Anisotropic Relaxation. J Phys Chem B. 2021 Sep 2;125(34):9692–707.
37. Lakowicz JR, Szmacinski H, Nowaczyk K, Johnson ML. Fluorescence lifetime imaging of free and protein-bound NADH. Proc Natl Acad Sci. 1992 Feb 15;89(4):1271–5.
38. Skala MC, Riching KM, Gendron-Fitzpatrick A, Eickhoff J, Eliceiri KW, White JG, et al. In vivo multiphoton microscopy of NADH and FAD redox states, fluorescence lifetimes, and cellular morphology in precancerous epithelia. Proc Natl Acad Sci. 2007 Dec 4;104(49):19494–9.

39. Kalinina S, Breymayer J, Schäfer P, Calzia E, Shcheslavskiy V, Becker W, et al. Correlative NAD(P)H-FLIM and oxygen sensing-PLIM for metabolic mapping. J Biophotonics. 2016;9(8):800–11.
40. Verveer PJ, Hanley QS. Chapter 2 Frequency domain FLIM theory, instrumentation, and data analysis. In: Laboratory Techniques in Biochemistry and Molecular Biology [Internet]. Elsevier; 2009 [cited 2021 Mar 27]. p. 59–94. (Fret and Flim Techniques; vol. 33). Available from: https://www.sciencedirect.com/science/article/pii/S0075753508000028
41. van Munster EB, Gadella TWJ. Fluorescence Lifetime Imaging Microscopy (FLIM). In: Rietdorf J, editor. Microscopy Techniques: -/- [Internet]. Berlin, Heidelberg: Springer; 2005 [cited 2021 Aug 2]. p. 143–75. (Advances in Biochemical Engineering). Available from: https://doi.org/10.1007/b102213
42. Ishikawa-Ankerhold HC, Ankerhold R, Drummen GPC. Advanced Fluorescence Microscopy Techniques—FRAP, FLIP, FLAP, FRET and FLIM. Molecules. 2012 Apr;17(4):4047–132.
43. Suhling K, Hirvonen LM, Levitt JA, Chung PH, Tregidgo C, Le Marois A, et al. Fluorescence lifetime imaging (FLIM): Basic concepts and some recent developments. Med Photonics. 2015 May 1;27:3–40.
44. Gadella TWJ, Jovin TM, Clegg RM. Fluorescence lifetime imaging microscopy (FLIM): Spatial resolution of microstructures on the nanosecond time scale. Biophys Chem. 1993 Dec 1;48(2):221–39.
45. Hammarström L, Ritzén M, Ullberg S. Combined autoradiography and fluorescence microscopy. Localization of labelled 5-hydroxy-tryptophan in relation to endogenous 5-hydroxytryptamine in the gastrointestinal tract. Experientia. 1966 Apr 1;22(4):213–5.
46. Stojanovski D, Koutsopoulos OS, Okamoto K, Ryan MT. Levels of human Fis1 at the mitochondrial outer membrane regulate mitochondrial morphology. J Cell Sci. 2004 Mar 1;117(7):1201–10.
47. Juette MF, Gould TJ, Lessard MD, Mlodzianoski MJ, Nagpure BS, Bennett BT, et al. Three-dimensional sub–100 nm resolution fluorescence microscopy of thick samples. Nat Methods. 2008 Jun;5(6):527–9.
48. Nwaneshiudu A, Kuschal C, Sakamoto FH, Rox Anderson R, Schwarzenberger K, Young RC. Introduction to confocal microscopy. J Invest Dermatol. 2012 Dec;132(12):1–5.
49. Kervrann C, Legland D, Pardini L. Robust incremental compensation of the light attenuation with depth in 3D fluorescence microscopy. J Microsc. 2004;214(3):297–314.
50. Hell S, Reiner G, Cremer C, STELzer EHK. Aberrations in confocal fluorescence microscopy induced by mismatches in refractive index. J Microsc. 1993;169(3):391–405.
51. Denk W, Strickler JH, Webb WW. Two-Photon Laser Scanning Fluorescence Microscopy. Science [Internet]. 1990 Apr 6 [cited 2021 Sep 3]; Available from: https://www.science.org/doi/abs/10.1126/science.2321027
52. Helmchen F, Denk W. Deep tissue two-photon microscopy. Nat Methods. 2005 Dec;2(12):932–40.
53. Paddock SW. Confocal Laser Scanning Microscopy. BioTechniques. 1999 Nov 1;27(5):992–1004.
54. Diaspro A, Chirico G, Federici F, Cannone F, Beretta S, Robello M, et al. Two-photon microscopy and spectroscopy based on a compact confocal scanning head. J Biomed Opt. 2001 Jul;6(3):300–10.
55. Amos WB, White JG, Fordham M. Use of confocal imaging in the study of biological structures. Appl Opt. 1987 Aug 15;26(16):3239–43.
56. Buist A, Müller M, Squier J, Brakenhoff G. Real time two-photon absorption microscopy using multi point excitation. J Microsc. 1998 Nov;192(2):217–26.
57. de Haan K, Rivenson Y, Wu Y, Ozcan A. Deep-Learning-Based Image Reconstruction and Enhancement in Optical Microscopy. Proc IEEE. 2020 Jan;108(1):30–50.
58. Boulanger J, Kervrann C, Bouthemy P, Elbau P, Sibarita JB, Salamero J. Patch-Based

Nonlocal Functional for Denoising Fluorescence Microscopy Image Sequences. IEEE Trans Med Imaging. 2010 Feb;29(2):442–54.
59. Chen X, Zhou X, Wong STC. Automated segmentation, classification, and tracking of cancer cell nuclei in time-lapse microscopy. IEEE Trans Biomed Eng. 2006 Apr;53(4):762–6.
60. Pawlicki M, Collins HA, Denning RG, Anderson HL. Two-Photon Absorption and the Design of Two-Photon Dyes. Angew Chem Int Ed. 2009;48(18):3244–66.
61. Schermelleh L, Ferrand A, Huser T, Eggeling C, Sauer M, Biehlmaier O, et al. Super-resolution microscopy demystified. Nat Cell Biol. 2019 Jan;21(1):72–84.
62. Blake DJ, Weir A, Newey SE, Davies KE. Function and Genetics of Dystrophin and Dystrophin-Related Proteins in Muscle. Physiol Rev. 2002 Apr 1;82(2):291–329.
63. Giepmans BNG, Adams SR, Ellisman MH, Tsien RY. The Fluorescent Toolbox for Assessing Protein Location and Function. Science. 2006 Apr 14;312(5771):217–24.
64. Chinen AB, Guan CM, Ferrer JR, Barnaby SN, Merkel TJ, Mirkin CA. Nanoparticle Probes for the Detection of Cancer Biomarkers, Cells, and Tissues by Fluorescence. Chem Rev. 2015 Oct 14;115(19):10530–74.
65. Lamm MH, Ke PC. Cell Trafficking of Carbon Nanotubes Based on Fluorescence Detection. In: Balasubramanian K, Burghard M, editors. Carbon Nanotubes: Methods and Protocols [Internet]. Totowa, NJ: Humana Press; 2010 [cited 2021 Jul 14]. p. 135–51. (Methods in Molecular Biology). Available from: https://doi.org/10.1007/978-1-60761-579-8_12
66. Lagendijk EL, Validov S, Lamers GEM, De Weert S, Bloemberg GV. Genetic tools for tagging Gram-negative bacteria with mCherry for visualization in vitro and in natural habitats, biofilm and pathogenicity studies. FEMS Microbiol Lett. 2010 Apr 1;305(1):81–90.
67. Gahm Th, Reinhardt ER, Witte S. Analysis of the wall permeability of blood vessels in the rat mesentery. Res Exp Med (Berl). 1984 Mar 1;184(1):1–15.
68. YOUNG MR. Principles and Technique of Fluorescence Microscopy. J Cell Sci. 1961 Dec 1;s3-102(60):419–49.
69. Jaffe HH, Miller AL. The fates of electronic excitation energy. J Chem Educ. 1966 Sep;43(9):469.
70. Becker W. The bh TCSPC Handbook 8th ed. [Internet]. 8th ed. 2019 [cited 2021 Aug 2]. Available from: https://www.becker-hickl.com/literature/documents/flim/the-bh-tcspc-handbook/
71. Rosenberg HM, E. Eimutis. Solvent shifts in electronic spectra—I. Stokes shift in a series of homologous aromatic amines. Spectrochim Acta. 1966 Oct 1;22(10):1751–7.
72. Diaspro A, Chirico G, Usai C, Ramoino P, Dobrucki J. Photobleaching. In: Pawley JB, editor. Handbook Of Biological Confocal Microscopy [Internet]. Boston, MA: Springer US; 2006 [cited 2022 Nov 8]. p. 690–702. Available from: https://doi.org/10.1007/978-0-387-45524-2_39
73. Li Q, He X, Wang Y, Liu H, Xu D, Guo F. Review of spectral imaging technology in biomedical engineering: achievements and challenges. J Biomed Opt. 2013 Oct;18(10):100901.
74. Shaner NC, Campbell RE, Steinbach PA, Giepmans BNG, Palmer AE, Tsien RY. Improved monomeric red, orange and yellow fluorescent proteins derived from Discosoma sp. red fluorescent protein. Nat Biotechnol. 2004 Dec;22(12):1567–72.
75. Campbell RE, Tour O, Palmer AE, Steinbach PA, Baird GS, Zacharias DA, et al. A monomeric red fluorescent protein. Proc Natl Acad Sci. 2002 Jun 11;99(12):7877–82.
76. Shaner NC, Patterson GH, Davidson MW. Advances in fluorescent protein technology. J Cell Sci. 2007 Dec 15;120(24):4247–60.
77. Gunduz N. The use of FITC-conjugated gated monoclonal antibodies for determination of S-phase cells with fluorescence microscopy. Cytometry. 1985;6(6):597–601.
78. Schubert W, Bonnekoh B, Pommer AJ, Philipsen L, Böckelmann R, Malykh Y, et al. Analyzing proteome topology and function by automated multidimensional fluorescence

microscopy. Nat Biotechnol. 2006 Oct;24(10):1270–8.
79. Gebhardt C, Lehmann M, Reif MM, Zacharias M, Gemmecker G, Cordes T. Molecular and Spectroscopic Characterization of Green and Red Cyanine Fluorophores from the Alexa Fluor and AF Series**. ChemPhysChem. 2021;22(15):1566–83.
80. Berlier JE, Rothe A, Buller G, Bradford J, Gray DR, Filanoski BJ, et al. Quantitative Comparison of Long-wavelength Alexa Fluor Dyes to Cy Dyes: Fluorescence of the Dyes and Their Bioconjugates. J Histochem Cytochem. 2003 Dec 1;51(12):1699–712.
81. Ryder AG, Power S, Glynn TJ, Morrison JJ. Time-domain measurement of fluorescence lifetime variation with pH. In: Biomarkers and Biological Spectral Imaging [Internet]. International Society for Optics and Photonics; 2001 [cited 2021 Jul 14]. p. 102–9. Available from: https://www.spiedigitallibrary.org/conference-proceedings-of-spie/4259/0000/Time-domain-measurement-of-fluorescence-lifetime-variation-with-pH/10.1117/12.432487.short
82. Lebakken CS, Kang HC, Vogel KW. A Fluorescence Lifetime–Based Binding Assay to Characterize Kinase Inhibitors. J Biomol Screen. 2007 Sep 1;12(6):828–41.
83. Kolenc OI, Quinn KP. Evaluating Cell Metabolism Through Autofluorescence Imaging of NAD(P)H and FAD. Antioxid Redox Signal. 2019 Feb 20;30(6):875–89.
84. Walsh AJ, Skala MC. Optical metabolic imaging quantifies heterogeneous cell populations. Biomed Opt Express. 2015 Feb 1;6(2):559–73.
85. Becker W. Advanced Time-Correlated Single Photon Counting Techniques. Springer Science & Business Media; 2005. 414 p.
86. O'Connor D. Time-correlated single photon counting. Academic Press; 2012. 299 p.
87. Raspe M, Kedziora KM, van den Broek B, Zhao Q, de Jong S, Herz J, et al. siFLIM: single-image frequency-domain FLIM provides fast and photon-efficient lifetime data. Nat Methods. 2016 Jun;13(6):501–4.
88. Becker & Hickl GmbH [Internet]. Becker & Hickl GmbH. [cited 2021 Mar 27]. Available from: https://www.becker-hickl.com/
89. PicoQuant GmbH [Internet]. PicoQuant. [cited 2021 Mar 27]. Available from: https://www.picoquant.com/
90. Lakner PH, Monaghan MG, Möller Y, Olayioye MA, Schenke-Layland K. Applying phasor approach analysis of multiphoton FLIM measurements to probe the metabolic activity of three-dimensional in vitro cell culture models. Sci Rep. 2017 Feb 13;7(1):42730.
91. Gerritsen HC, Agronskaia AV, Bader AN, Esposito A. Chapter 3 Time domain FLIM: Theory, instrumentation, and data analysis. In: Laboratory Techniques in Biochemistry and Molecular Biology [Internet]. Elsevier; 2009 [cited 2021 Dec 1]. p. 95–132. (Fret and Flim Techniques; vol. 33). Available from: https://www.sciencedirect.com/science/article/pii/S007575350800003X
92. Levenberg K. A method for the solution of certain non-linear problems in least squares. Q Appl Math. 1944 Jul 1;2(2):164–8.
93. Zhu X, Zhang D. Efficient Parallel Levenberg-Marquardt Model Fitting towards Real-Time Automated Parametric Imaging Microscopy. PLOS ONE. 2013 Oct 10;8(10):e76665.
94. Moré JJ. The Levenberg-Marquardt algorithm: Implementation and theory. In: Watson GA, editor. Numerical Analysis. Berlin, Heidelberg: Springer; 1978. p. 105–16. (Lecture Notes in Mathematics).
95. Lu G, Fei B. Medical hyperspectral imaging: a review. J Biomed Opt. 2014 Jan;19(1):010901.
96. Tsuchiya A, Endo I. Optical switching apparatus for a reflected fluorescence microscope [Internet]. US5633752A, 1997 [cited 2021 Dec 1]. Available from: https://patents.google.com/patent/US5633752A/en
97. Lichtman JW, Conchello JA. Fluorescence microscopy. Nat Methods. 2005 Dec;2(12):910–9.

98. Gao Liang, Smith RT. Optical hyperspectral imaging in microscopy and spectroscopy – a review of data acquisition. J Biophotonics. 2015;8(6):441–56.
99. Gehm ME, Kim MS, Fernandez C, Brady DJ. High-throughput, multiplexed pushbroom hyperspectral microscopy. Opt Express. 2008 Jul 21;16(15):11032–43.
100. Klein L, Žídek K. Collection of micromirror-modulated light in the single-pixel broadband hyperspectral microscope. Rev Sci Instrum. 2020 Jun 1;91(6):063701.
101. Jin S, Hui W, Wang Y, Huang K, Shi Q, Ying C, et al. Hyperspectral imaging using the single-pixel Fourier transform technique. Sci Rep. 2017 Mar 24;7(1):45209.
102. Proll KP, Nivet JM, Voland C, Tiziani HJ. Application of a liquid-crystal spatial light modulator for brightness adaptation in microscopic topometry. Appl Opt. 2000 Dec 1;39(34):6430–5.
103. Cho DJ, Thurman ST, Donner JT, Morris GM. Characteristics of a 128 x 128 liquid-crystal spatial light modulator for wave-front generation. Opt Lett. 1998 Jun 15;23(12):969–71.
104. Dudley D, Duncan WM, Slaughter J. Emerging digital micromirror device (DMD) applications. In: MOEMS Display and Imaging Systems [Internet]. SPIE; 2003 [cited 2021 Dec 1]. p. 14–25. Available from: https://www.spiedigitallibrary.org/conference-proceedings-of-spie/4985/0000/Emerging-digital-micromirror-device-DMD-applications/10.1117/12.480761.full
105. Dobigeon N, Altmann Y, Brun N, Moussaoui S. Chapter 6 - Linear and Nonlinear Unmixing in Hyperspectral Imaging. In: Ruckebusch C, editor. Data Handling in Science and Technology [Internet]. Elsevier; 2016 [cited 2021 Dec 1]. p. 185–224. (Resolving Spectral Mixtures; vol. 30). Available from: https://www.sciencedirect.com/science/article/pii/B9780444636386000061
106. Xu H, Rice BW. In-vivo fluorescence imaging with a multivariate curve resolution spectral unmixing technique. J Biomed Opt. 2009 Nov;14(6):064011.
107. McRae TD, Oleksyn D, Miller J, Gao YR. Robust blind spectral unmixing for fluorescence microscopy using unsupervised learning. PLOS ONE. 2019 Dec 2;14(12):e0225410.
108. Friston KJ, Jezzard P, Turner R. Analysis of functional MRI time-series. Hum Brain Mapp. 1994;1(2):153–71.
109. Westbrook C, Talbot J. MRI in Practice. John Wiley & Sons; 2018. 418 p.
110. Buzug TM. Computed Tomography. In: Kramme R, Hoffmann KP, Pozos RS, editors. Springer Handbook of Medical Technology [Internet]. Berlin, Heidelberg: Springer; 2011 [cited 2022 Nov 11]. p. 311–42. (Springer Handbooks). Available from: https://doi.org/10.1007/978-3-540-74658-4_16
111. Miles KA. Functional computed tomography in oncology. Eur J Cancer. 2002 Nov 1;38(16):2079–84.
112. Collis RTH. Lidar. Appl Opt. 1970 Aug 1;9(8):1782–8.
113. Raj T, Hashim FH, Huddin AB, Ibrahim MF, Hussain A. A Survey on LiDAR Scanning Mechanisms. Electronics. 2020 May;9(5):741.
114. Antipa N, Kuo G, Heckel R, Mildenhall B, Bostan E, Ng R, et al. DiffuserCam: lensless single-exposure 3D imaging. Optica. 2018 Jan 20;5(1):1–9.
115. Shroff H, White H, Betzig E. Photoactivated Localization Microscopy (PALM) of Adhesion Complexes. Curr Protoc Cell Biol. 2013;58(1):4.21.1-4.21.28.
116. Zuo C, Sun J, Chen Q. Adaptive step-size strategy for noise-robust Fourier ptychographic microscopy. Opt Express. 2016 Sep 5;24(18):20724–44.
117. OpenScan – Laboratory for Optical and Computational Instrumentation [Internet]. [cited 2021 Aug 2]. Available from: https://eliceirilab.org/openscan/
118. Edelstein AD, Tsuchida MA, Amodaj N, Pinkard H, Vale RD, Stuurman N. Advanced methods of microscope control using μManager software. J Biol Methods. 2014;1(2):e10.
119. Schindelin J, Arganda-Carreras I, Frise E, Kaynig V, Longair M, Pietzsch T, et al. Fiji: an

open-source platform for biological-image analysis. Nat Methods. 2012 Jul;9(7):676–82.
120. Berthold MR, Cebron N, Dill F, Gabriel TR, Kötter T, Meinl T, et al. KNIME - the Konstanz information miner: version 2.0 and beyond. ACM SIGKDD Explor Newsl. 2009 Nov 16;11(1):26–31.
121. MATLAB [Internet]. The Mathworks, Inc.; 2021. Available from: https://www.mathworks.com/products/matlab.html
122. Jones TR, Kang IH, Wheeler DB, Lindquist RA, Papallo A, Sabatini DM, et al. CellProfiler Analyst: data exploration and analysis software for complex image-based screens. BMC Bioinformatics. 2008 Nov 15;9(1):482.
123. Piccinini F, Kiss A, Horvath P. CellTracker (not only) for dummies. Bioinformatics. 2016 Mar 15;32(6):955–7.
124. Davis TA. MATLAB Primer. CRC Press; 2010. 232 p.
125. Knight A. Basics of MATLAB and Beyond. New York: Chapman and Hall/CRC; 2019. 216 p.
126. Gahm NA, Rueden CT, Evans III EL, Selzer G, Hiner MC, Chacko JV, et al. New Extensibility and Scripting Tools in the ImageJ Ecosystem. Curr Protoc. 2021;1(8):e204.
127. Schindelin J, Rueden CT, Hiner MC, Eliceiri KW. The ImageJ ecosystem: An open platform for biomedical image analysis. Mol Reprod Dev. 2015;82(7–8):518–29.
128. Rueden CT, Schindelin J, Hiner MC, DeZonia BE, Walter AE, Arena ET, et al. ImageJ2: ImageJ for the next generation of scientific image data. BMC Bioinformatics. 2017 Nov 29;18(1):529.
129. Schroeder AB, Dobson ETA, Rueden CT, Tomancak P, Jug F, Eliceiri KW. The ImageJ ecosystem: Open-source software for image visualization, processing, and analysis. Protein Sci. 2021;30(1):234–49.
130. Lutz M. Programming Python. O'Reilly Media, Inc.; 2001. 1300 p.
131. Rueden CT, Hiner MC, Evans EL, Pinkert MA, Lucas AM, Carpenter AE, et al. PyImageJ: A library for integrating ImageJ and Python. Nat Methods. 2022 Nov;19(11):1326–7.
132. G. van Rossum (Guido). Python reference manual [Internet]. Department of Computer Science [CS]. CWI; 1995 [cited 2022 Nov 12]. Available from: https://ir.cwi.nl/pub/5008
133. Walt S van der, Schönberger JL, Nunez-Iglesias J, Boulogne F, Warner JD, Yager N, et al. scikit-image: image processing in Python. PeerJ. 2014 Jun 19;2:e453.
134. Sofroniew N, Lambert T, Evans K, Nunez-Iglesias J, Bokota G, Winston P, et al. napari: a multi-dimensional image viewer for Python [Internet]. 2022 [cited 2022 Apr 29]. Available from: https://github.com/napari/napari
135. Chityala R, Pudipeddi S. Image Processing and Acquisition using Python. 2nd ed. New York: Chapman and Hall/CRC; 2020. 451 p.
136. Jurica P, Van Leeuwen C. OMPC: an open-source MATLAB®-to-Python compiler. Front Neuroinformatics [Internet]. 2009 [cited 2022 Nov 12];3. Available from: https://www.frontiersin.org/articles/10.3389/neuro.11.005.2009
137. Xia XQ, McClelland M, Wang Y. PypeR, A Python Package for Using R in Python. J Stat Softw. 2010 Jul 30;35:1–8.
138. Waller L, Tian L. Machine learning for 3D microscopy. Nature. 2015 Jul;523(7561):416–7.
139. Auran JD, Koester CJ, Kleiman NJ, Rapaport R, Bomann JS, Wirotsko BM, et al. Scanning Slit Confocal Microscopic Observation of Cell Morphology and Movement within the Normal Human Anterior Cornea. Ophthalmology. 1995 Jan 1;102(1):33–41.
140. Castellano-Muñoz M, Peng AW, Salles FT, Ricci AJ. Swept Field Laser Confocal Microscopy for Enhanced Spatial and Temporal Resolution in Live-Cell Imaging. Microsc Microanal Off J Microsc Soc Am Microbeam Anal Soc Microsc Soc Can. 2012 Aug;18(4):753–60.

141. Edelstein A, Amodaj N, Hoover K, Vale R, Stuurman N. Computer Control of Microscopes Using μManager. Curr Protoc Mol Biol. 2010;92(1):14.20.1-14.20.17.
142. Schroeder J l., Bakalar M, Pohida T j., Balaban R s. Rapid overlapping-volume acquisition and reconstruction (ROVAR): automated 3D tiling for high-resolution, large field-of-view optical microscopy. J Microsc. 2011;243(1):103–10.
143. Becker J. Scanning tunneling microscope computer automation. Surf Sci. 1987 Mar 1;181(1):200–9.
144. Agkland BD, Weste NH. The edge flag algorithm — A fill method for raster scan displays. IEEE Trans Comput. 1981 Jan;C–30(1):41–8.

Chapter 2: Spectrally-split Swept-Field Confocal (SSFC)

Computational microscopy tends to build highly specialized custom microscopes, but the underlying principles can readily extend further than the individual microscope [1–6]. As such the SSFC project looked to utilize the pinholes of a swept-field confocal and a prism to generate distinct points corresponding to specific spectral components in a field of view [7–9]. The hardware side of the project was done prior to my work in collaboration with Bruker Nano Surfaces FM, Middleton, WI. Unlike traditional hyperspectral imaging, it is unique in that it was implemented through a modification of a swept-field confocal, and therefore has better background rejection [10–12]. Furthermore since it is a fairly simple modification of an existing system, there will be other scan head geometries that are suited for having this method added.

The hardware led to an interesting computational reconstruction problem that was solved through an approach I developed. For reconstruction the individual spectral bands in each image are found then each pixel is mapped to a wavelength interpolated from the calibrated wavelength range of the system. Multiple imaging corrections are implemented to make this work reliably. Furthermore, through the variety of corrections that it utilizes for reconstruction it provides more ready access for others to implement similar corrections to improve their data quality, since each correction is functionalized and can be used as a stand alone method. Even the built in tiling method is easily split out and can be used for any dataset with an associated xy position file. This approach was implemented in MATLAB but the scripts, algorithms, and methods are available open source on Github and the interface was generalized such that it can work with any optical imaging modality that produces a sequence of images with distinct bands that contain spectral information [13]. Therein making it available for further development and adaptation. As the field of computational microscopy expands, this project provides an open source basis for future spectral based methods.

Adapted from “Hyperspectral Multipoint High-Speed Confocal Microscopy” Gahm, Niklas A., Velten Andreas, Fong, Jimmy J., Swider, Zachary T., Haynes, Elizabeth, Vogt, William, Plavicki, Jessica, Larson, Matthew E., Gu, Yimeng, Thite, John G., Halloran, Mary, Bement, William M., Eliceiri, Kevin W., PlosOne (in Review)

Abstract:

Live imaging of biological processes often necessitates the combination of high-speed acquisition with high spatial resolution while tracking multiple fluorescently labeled components. This need has driven many advances in optical microscopy including the development of improved spectral detectors, optical sectioning techniques, high speed imaging, and sophisticated analysis approaches that can isolate fluorescence signals of interest from interfering background in space and time. We report the development of a hyperspectral confocal microscope that leverages the high-speed, high sensitivity capabilities of multipoint confocal designs with an Amici prism dispersing element and paired spectral analysis software. This hyperspectral, multipoint scanner can image multiple spectral channels simultaneously at high-speed while retaining high spatial resolution and sensitivity and is extensible to generic multipoint confocal systems.

Introduction

Over the last thirty years laser scanning microscopy (LSM) has become an indispensable tool in biological research. This is largely due to LSM's unrivaled ability to provide high-resolution images of fluorescence optical sections of living structures together with their dynamics. Fluorophores can range from endogenous metabolites (e.g. reduced nicotinamide adenine dinucleotide, NADH) and genetically engineered proteins (e.g. GFP::tubulin) to exogenous probes (e.g. FM series lipid probes or the Ca++ indicator Fura). LSM techniques such as confocal laser scanning microscopy (CLSM) [10–12,14] and multiphoton laser scanning microscopy (MPLSM) [15–17] microscopes have been developed to provide images from within a solid specimen that are largely free of interference from out-of-focus signals arising from fluorescent structures above and below the plane of focus. Stacks of optical sections can be collected enabling the three-dimensional structures of living specimens to be visualized over time [11,18]. Development of fast confocal scanning technologies such as multipoint, spinning disc [19,20] and slit scanners [7] have allowed high speed image collection of rapid biological events such as calcium transients in neuronal signaling [21]. Information on the nature and physiological milieu of a fluorophore can be gleaned from its emission spectrum. Non-confocal, push-broom [22,23] and confocal [24] slit scan systems have been used with spectral detection. These systems are relatively slow as only one column (or row) of pixels is captured at a time (the other axis being used for spectral information). The non-confocal systems provide little out-of-focus rejection. The confocal slit systems only provide rejection of out-of-focus light that is proportional to the distance from the focal plane. In contrast, point-scanning confocals achieve rejections proportional to the square of the distance. This renders slit scanners less suited for imaging at depth in scattering specimens. Slit scanning systems also may not be ideal when used with a square EMCCD or sCMOS sensor typically used on a microscope. In a standard slit scanning setup this leads to a resolution in the spectral axis equal to the resolution in both spatial axes and consequently a poor spatial resolution or an excessive spectral resolution resulting in slow data collection. Unfortunately, despite advances in speed and

detection, fast confocals are currently limited when dealing with multiple fluorophores, particularly those with overlapping spectra. Many approaches have been developed for spectral detection with confocal microscopes [25–29], most using a filter or grating technology. However, these approaches are often light inefficient and can slow the imaging due to either longer collection times needed for acquisition of sufficient light, or to exchange optical filters. This is a major problem when imaging multiple fluorophores in biological specimens where rapid capture of events is required. This issue and the large number of physiological reporters available and the frequent requirement to observe the dynamics of biological phenomena, all underscore the need for high-speed confocal imaging that provides spectral resolution with negligible sensitivity penalties.

Uses of color discrimination in optical microscopy

Spectral information is critical in biological microscopy to obtain functional information when examining endogenous or exogenous fluorescent reporters [30–33]. Efficient discrimination of spectral signals is important for isolating a fluorescence signal of interest from background, be it intrinsic fluorescence such as NADH in metabolism studies, or an extrinsic label such as GFP-labeled signaling proteins in a subcellular trafficking study. Spectral analysis can be used not only to establish the identity of a fluorophore but also to study more complex phenomena, such as the spectral shifts produced by fluorescence resonance energy transfer (FRET [34]).

Requirement for high speed and quantum efficiency in live cell imaging

When imaging dynamic or sensitive samples, such as in vivo specimens, the benefits of increased spatial and spectral resolution need to be balanced with requirements for fast capture and minimal light exposure to the sample. Dynamic biological events can change on timescales ranging from fractions of a second to minutes or hours. Exposure to light can cause heating or other phototoxic effects that can damage the specimen [35]. It is therefore essential to optimally utilize the fluorescence signal from the sample. This involves not only detecting the fluorescence photons with high efficiency and low noise but also extracting a maximum amount of information from every detected photon.

Multipoint Confocals

Image capture speed with bright fluorescent signals is largely limited by technical factors, such as detector readout, fluorescence excited state lifetime and data acquisition speeds. However, with in vivo specimens, signals are typically very low intensity because of the low abundance of fluorophore. High levels of excitation cannot compensate for this limited intensity because of fluorophore saturation (caused by ground-state depletion [36]) and phototoxicity. These factors, along with the sensitivity of the detectors, present fundamental limits to the speed at which images of sufficient signal-to-noise ratio for analysis can be captured. Weak fluorescent signals are common in many biological applications for reasons ranging from either dim intrinsic fluorescence signals, low expression of genetic fluorescence markers, non-ideal staining, weak antibody fluorescence labeling or signal attenuation due to scatter. Traditional laser scanning confocal microscopes [10,37] operating with a single aperture and using photomultipliers (PMT)

as single pixel readouts are limited in image acquisition rate by the speed of the scanning mirrors and the limited quantum efficiency of the PMT detector. Furthermore, fluorophore saturation provides a fundamental limitation to the achievable signal level. A practical and demonstrated solution involves scanning multiple apertures simultaneously, using a high quantum efficiency multipixel area detector such as a Charge Coupled Device (CCD) camera. This technique is used in spinning disc confocal microscopes [38], and other multipoint non-confocal microscope designs [18,39]. Multipoint confocals have better out-of-focus rejection than slit scanning systems; however cross-talk between adjacent pinholes (which occurs when the light cones from individual pinholes overlap) causes them to have inferior out-of-focus rejection compared to single point confocals. This cross-talk depends on the separation between pinholes. In the swept-field confocal design that we describe as a linear array of 32 pinholes scans the field of view, which is considerably fewer than that used in a typical spinning disk system. The performance of the swept-field confocal is therefore intermediate between a spinning disk and a single-point confocal system.

A disadvantage of confocal imaging is that signals emanating away from the focal plane are blocked. This often leads to high levels of illumination being used to compensate for a loss of brightness. This in turn can lead to increased levels of photobleaching compared to a bright-field or structured illumination microscope. This is due to the nonlinearity of photobleaching as a function of light intensity [40,41]. Even though a confocal microscope may deliver the same amount of excitation light as a bright-field microscope on average, the highly concentrated beam at the focus results in a much higher local peak intensity and therefore more bleaching. This added bleaching increases as the confocality increases, with bright-field systems having the least bleaching followed by slit scanners, multipoint confocals, and finally single-point confocals that cause the most bleaching.

Spectral Confocal Microscopy

Spectral resolution in confocal microscopes is often obtained by multiple exposures, using a succession of different color optical filters. This technique is easy to implement but can require a priori knowledge of the signals and is slow and inefficient in the use of the fluorescent signal [42]. An alternate approach uses a dispersive element (usually a diffraction grating) to spatially separate different wavelength components [43,44]. The spectrum of a single pixel is collected by a multichannel detector, such as a multi-channel PMT. Unfortunately, currently available conventional multi-channel PMTs have low quantum efficiencies (<40%), limited by their photocathodes. The large physical size of the PMT channels requires a high-dispersion grating to separate the spectrum. Simple gratings are inefficient (< 50%) when used with the broadband unpolarized light created by a fluorophore. Prisms, in contrast, are generally more efficient. With the use of custom multilayer coatings, prisms can provide efficiencies well above 95% [45]. However, due to the low dispersion achievable by prisms, it can be challenging to effectively combine a prism with a multichannel PMT. Nevertheless, simple prisms can be used to spread spectra across the limited distance of a few pixels on an Electron Multiplying Charge Coupled Device (EMCCD) area detector to capture the spectra. This is an attractive strategy as EMCCD frame imaging cameras can have very high quantum efficiencies (>90%). Elliott et. al. [46] demonstrated a hyperspectral detector based on optical remapping of the hyperspectral image

information on a two dimensional detector [46]. However, this system requires the collection of hundreds or thousands of frames, making this method slow in practice.

In all these approaches, the spectral element necessarily changes the optical path, necessitating a complete redesign of the microscope scan head. This often means that hyperspectral scanning and regular monochrome filter based confocal scanning cannot simply be performed on the same instrument.

A spectral element that does not change the optical path can of course always be achieved using multiple optical elements like mirrors or prisms to lead the beam back to the original optic axis after passing the spectral element. An efficient design based on this principle is the prism grating prism configuration (PGP) [47] used in some commercial line imaging spectrometers (e.g. ImSpector V8E used in Schultz et al., 2001 [22]) [23,24,48]. This approach requires multiple aligned elements rather than one monolithic bonded part and is therefore typically more complex and space consuming than an Amici prism. Because of the grating used it is still significantly less efficient than a prism (The manufacturer of ImSpector states >50% efficiency for unpolarized light).

Another way of capturing spectrally resolved bright field images on a two dimensional sensor is through different forms of coding such as Hadamard transforms. This technique is, for example employed in Hanley et. al. [49] The encoding process removes the need for scanning of the sample but does not reduce the total amount of data that needs to be recorded for a given spectral and spatial resolution. Instead of actuating scanning mirrors, the system requires a series of patterns to be applied to the light in the optical path using a spatial light modulator and a series of coded spectral images to be captured from which the hyperspectral image can be reconstructed. Capturing and processing an individual image takes about 30 minutes. Assuming the system was not limited by hardware and processing speed and only by the fundamental issue of fluorophore saturation, the collection could be faster than scanning systems with speed, bleaching, and depth and spatial resolution comparable to a bright field microscope. The system does not have built in confocality. Instead Hanley et. al. [49] use point spread function deconvolution to achieve some amount of out-of-focus rejection.

Our Approach: Prism-based Hyperspectral Multipoint Confocal

For the purposes of imaging dynamic biological events we sought to develop a novel system that combines the benefits of multipoint confocal, prism-based spectral discrimination, and high quantum efficiency array detection all in one modular and flexible platform with generalizable automated analysis software. Here we develop a prism-based approach for adaptation of multipoint confocal microscope designs for fast spectral capture. This approach combines the comparably low loss of prism-based systems along with the speed, signal-to-noise and viability advantages of multipoint confocal scanning while addressing the inherent image processing needs of utilizing a prism-based approach. In addition, our method has a key practical implementation advantage in that it allows easy switching from a regular confocal to a hyperspectral system. Furthermore, we present analysis software that can automatically detect and separate fluorophores in a spectrally split imaging approach of this nature.

Our design is based on a multipoint confocal microscope equipped with a sCMOS camera with a modified double Amici prism [50] as the dispersive element. Amici prisms provide wavelength separation without deflecting the mean direction of the beam and can therefore be easily added to existing systems. They are a low-cost solution commonly employed in hand-held spectrometers. By scanning several pinholes in parallel and collecting light with a sCMOS camera, our spectral multipoint confocal system achieves high capture speeds of up to 4 frames per second with 15 channels of spectral resolution. The high quantum efficiency of the sCMOS and the low loss of the prism provide high sensitivity and low noise. We demonstrate that the addition of hyperspectral imaging does not affect overall image quality and signal-to-noise ratio significantly.

Results

Capture Speed

The fastest technically possible capture speed is determined by the highest possible frame rate of the readout camera. Since one spectral image is composed of at least 15 frames, the fastest speed is 15 times slower than the frame rate of the readout camera, which is 400 frames per second for the ORCA-Flash4.0 V2 sCMOS (Hamamatsu, Hamamatsu City, Japan), 66 frames per second for the Evolve 512 Delta EMCCD (Photometrics, Tucson, AZ), and 31.5 frames per second for the QuantEM:512 SC (Photometrics, Tucson, AZ), resulting in a spectral frame rate of about 27, 4, and 2 frames per second respectively.

Noise Comparison

The signal-to-noise ratio in an image can generally be attributed to three different sources. (1) Readout noise: all noise introduced by the readout of the image from the camera. This noise depends on the number of readouts and is independent of exposure time or the strength of the detected signal. This noise is small if the EM gain of the camera is used to boost signal and could be eliminated completely with the use of photon counting. (2) Background noise: noise generated by the detector dark current and by stray ambient light. The amount of background noise is dependent on the exposure time. (3) Amplification (e.g. electron multiplication) noise: noise dependent on the gain provided by the sensor. This could, in principle, be eliminated entirely by using photon counting.

Adding spectral resolution capabilities to the microscope will influence the signal-to-noise ratio in captured images in two ways: (1) Losses introduced by the prism will weaken the signal and scattering in the prism may provide background noise. (2) Readout noise from the camera is summed due to the fact that at least 15 readouts are required to capture the data for one image.

To evaluate the loss introduced by the spectral separation, we imaged a FluoCells prepared slide (Invitrogen, Carlsbad, CA) of BPAE cells labeled with three different stains. Filamentous actin in these cells was labeled with Texas Red phalloidin, tubulin was labeled with BODPIPY FL-GAM, and nuclei were labeled with DAPI. The slide was imaged with four different configurations (Fig 1): (i) A non-spectral single frame exposure (i.e. no Amici prism in path) with multipoint confocal microscope. This image represents the optimally achievable signal quality (Fig 2.1a). (ii) The complete spectral system (i.e., Amici prism in path) using a total of 16 frames to compose one image (Fig 2.1d). (iii)The data captured with the spectral system but showing the sum of all color channels to obtain a monochrome image comparable to the optimal image (i) but containing the noise of the spectral image (ii) (Fig 2.1c). (iv) Finally, a frame average of 16 frames without the spectral system in place. This image contains noise due to readout but does not contain the noise due to loss and scattering in the prism (Fig 2.1b). In all cases, a four band Sedat emission filter with notches at 405/488/561/640m (Chroma, Bellow Falls, VT) was used to block emission lasers. The settings in all cases are otherwise identical with the exposure time chosen such that the aggregate exposure times are identical in all cases. The difference between Figs 1a and 1b is caused by the noise resulting from additional readouts. The difference between 1b and 1c, is due to the loss introduced by the Amici prism; image distortion incurred during image reconstruction is practically imperceptible.

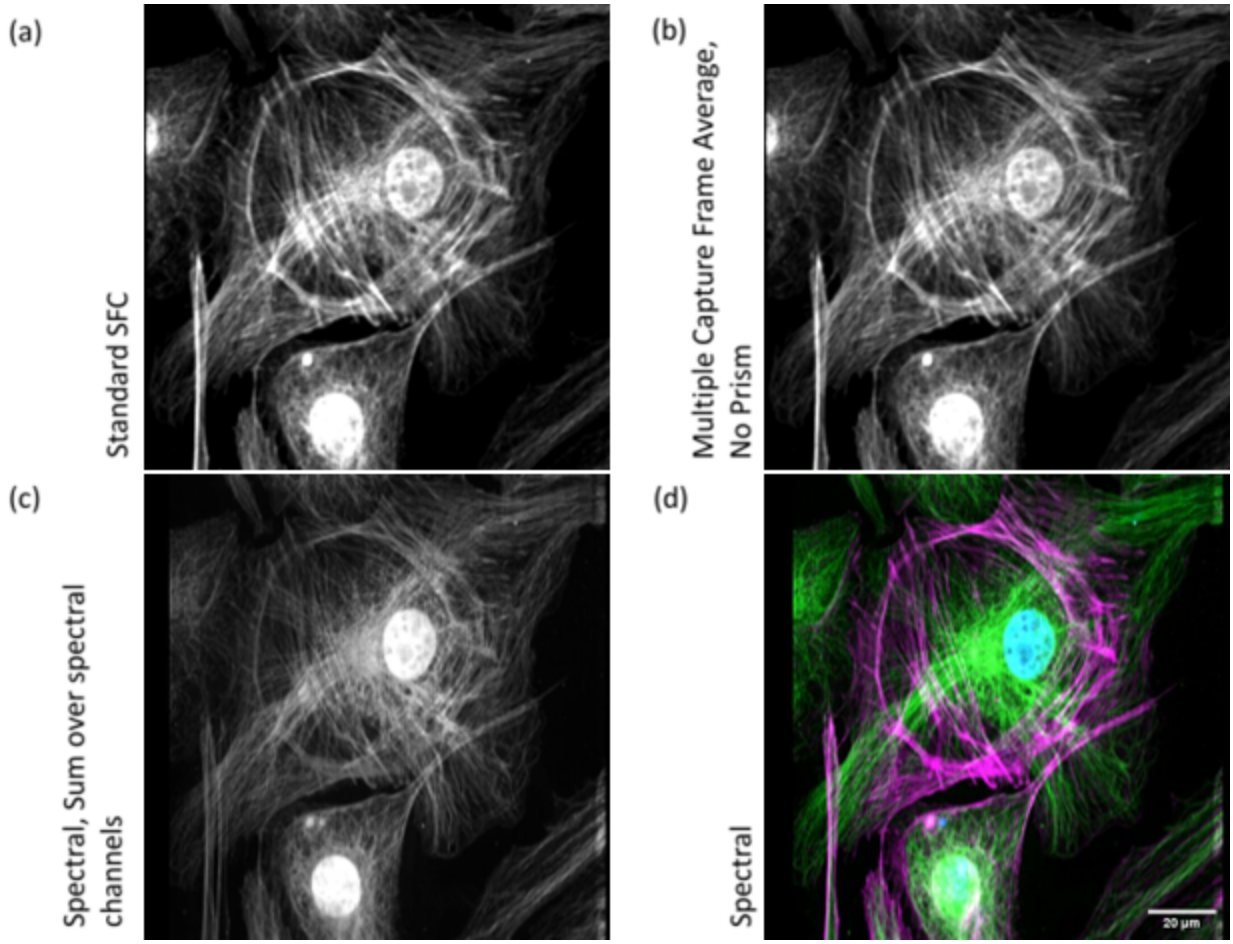

Figure 2.1: Noise analysis for low gain: (a) Single exposure image, 600 ms (b) 16 frames, 35ms frame average. (c) Sum of spectral channels 16 frames, 35 ms each. (d) Spectral image, 16 frames 35 ms each. The sample is the BPAE cells also shown in Figure 2.6. The image was captured with the sCMOS detector and filter configuration 2 (see section “System Dichroics and Emission Filters”).

Biological Specimen Testing

A number of fixed and live specimens were imaged to show the spectral sensitivity of the device for imaging biological samples. Fig 2.2 shows an image of a specimen of fixed BPAE cells labeled with three different fluorophores (Life Technologies, Carlsbad, CA) captured with a 60x oil 1.4 NA objective (Nikon, Mehlville, NY). This figure illustrates clear separation of the three labels. BPAE cells labeled with three different stains. Filamentous actin in these cells was labeled with Texas Red phalloidin, tubulin was labeled with BODIPY FL-GAM, and nuclei were labeled with DAPI.

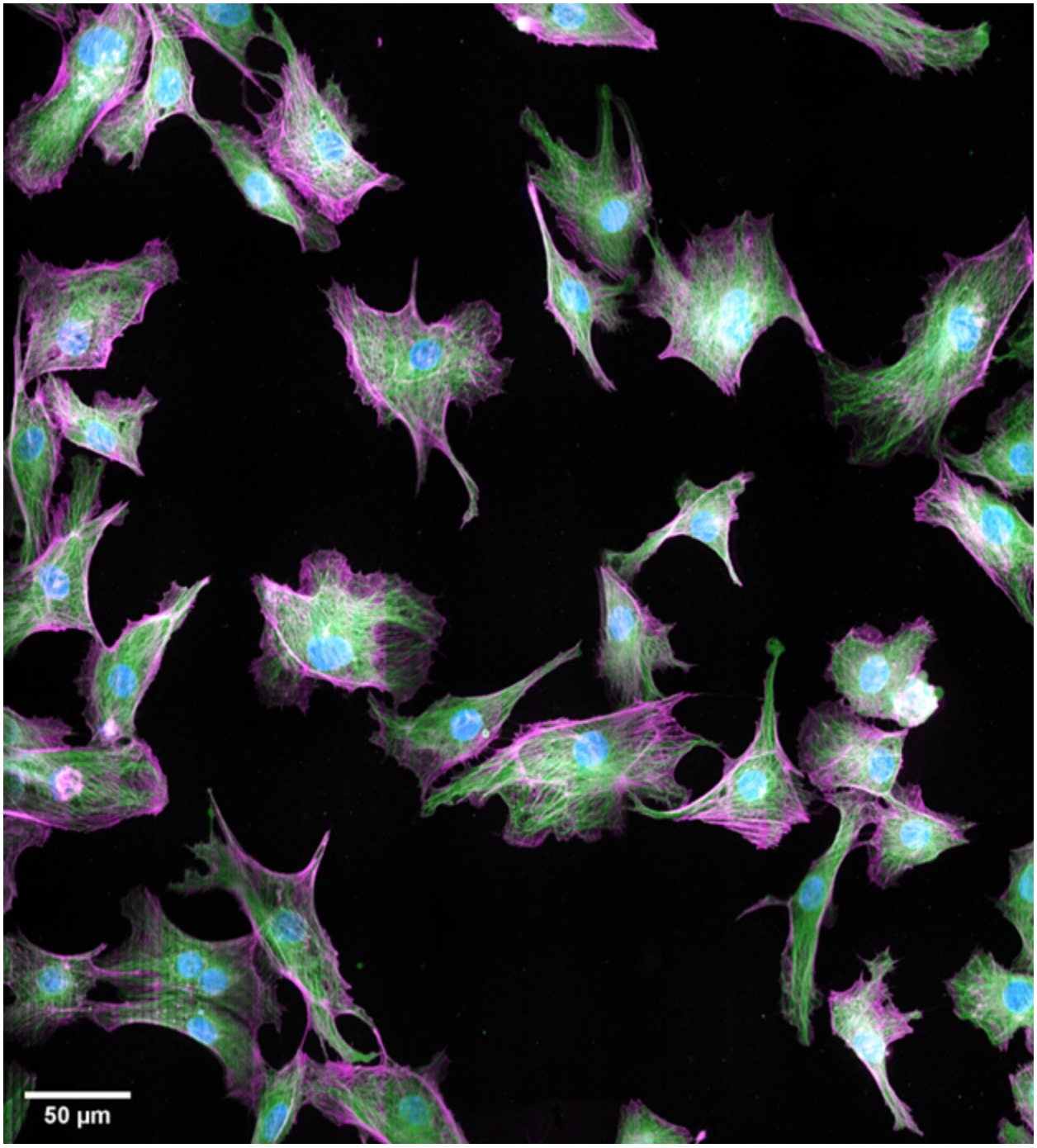

Figure 2.2: False color rendering of a 5x5 tiled mosaic of FluoCells commercial prepared slide (Invitrogen, Carlsbad, CA): BPAE Cells #2. Filamentous actin (green) in these cells was labeled with Texas Red phalloidin, tubulin (magenta) was labeled with BODIPY FL-GAM, and nuclei (blue) were labeled with DAPI. The image was captured with the sCMOS detector and filter configuration 2 (see section “System Dichroics and Emission Filters”) using a 60x oil objective and excitation at 488 nm, 561 nm, and 640 nm.

In addition to the commercially prepared BPAE slide, additional samples were examined to have more variety in fluorophores for spectral system performance evaluated. Fig 2.3 shows an image of our fixed sample of a zebrafish larva. The vasculature is shown in green and cell bodies in blue. The red stain shown did not penetrate the sample well, and only shows the outermost layer of the larva. As with the BPAE slide, the zebrafish sample showed good spectral fidelity with the expected fluorophore spectra.

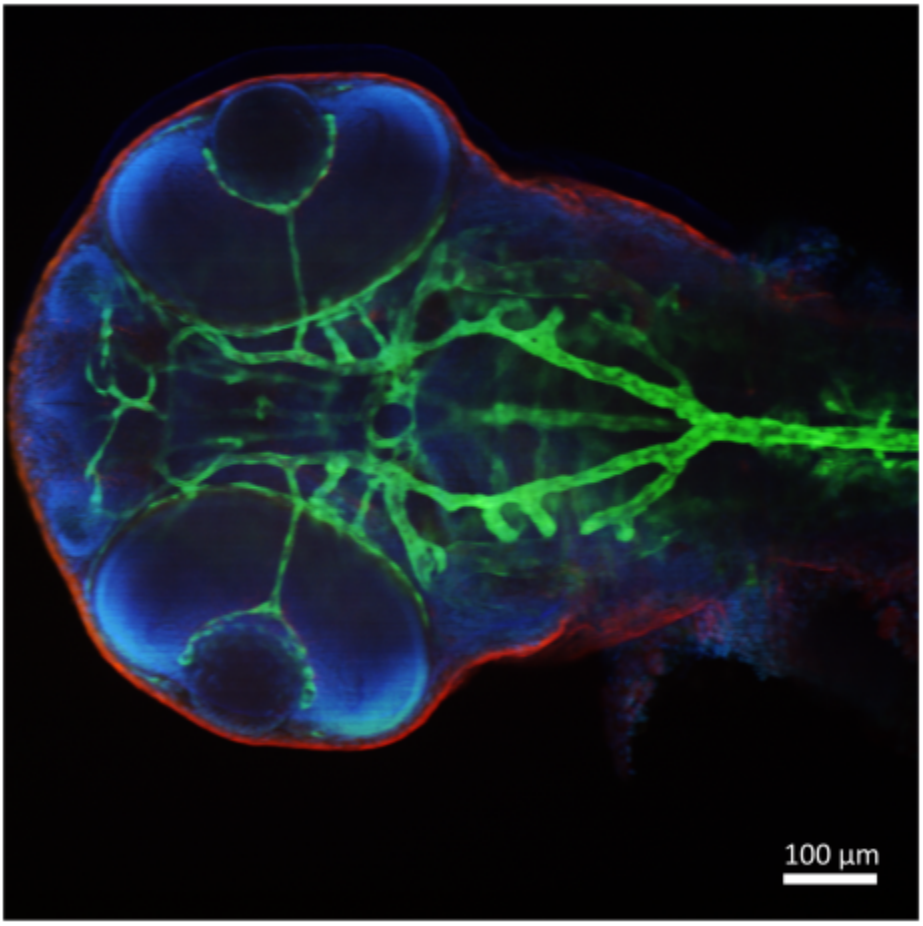

Figure 2.3: Transgenic zebrafish embryo (Tg(kdrl:GFP) also known as Tg(flk1:GFP) stained for glial fibrillary acidic protein (GFAP) labeled with Alexa 568 (red) which did not penetrate the sample well and mounted in Vectashield mounting medium containing 4,′6′-diaminido-2-phenylindole (DAPI) (blue) (Vector Laboratories, Burlingame, CA). The developing vasculature is marked by kdrl driven GFP expression (green). The image was captured with EMCCD detector and filter configuration 2 (see section “System Dichroics and Emission Filters”) using a 10x air objective and excitation at 405 nm, 488 nm, 561 nm, and 640 nm.

As the strength of the hyperspectral multipoint system described is the ability to collect spectral images at high speed, two live samples are demonstrated. Neuronal growth and movement in a live zebrafish embryo is shown in S2.1 Movie. Frames were captured every minute with a 200 ms exposure. A maximum intensity projection of one time point is shown in Fig 2.4 The sensory neurons shown in green are labeled with membrane-targeted GFP and motor neurons shown in magenta are labeled with mCherry.

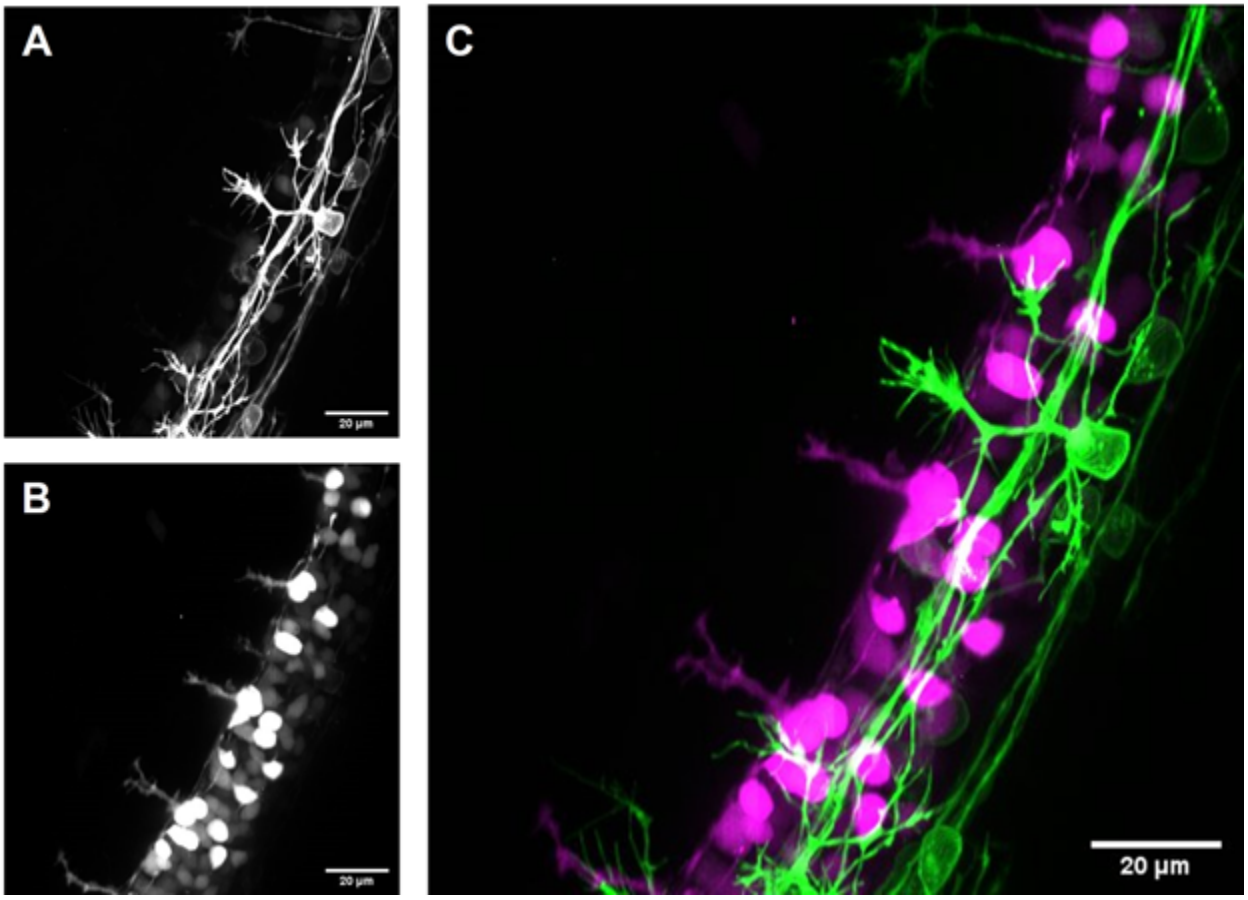

Figure 2.4: Frame from a video of neuronal growth in live transgenic zebrafish embryo showing the separation of fluorophores. (A) Sensory neurons (green) are labeled with GFP and (B) motor neurons (magenta) are labeled with mCherry. (C) False colored composite. A video of the growth is provided in supplementary movie 2.1. The image was captured with a sCMOS detector and filter configuration 2 (see section "System Dichroics and Emission Filters") frames were taken every minute with a 40x oil objective.

Additionally, mitosis in a live *Xenopus laevis* embryo is shown in S2.2 Movie. This movie was captured with a 75 ms exposure every 5 seconds. A single hyperspectral frame at 75 ms exposure time is shown in Fig 2.5. The cell membrane was labeled with mTagBFP::CAAX and

shown in blue, microtubules were labeled with mCherry-a tubulin displayed in cyan, and chromatin is visualized with miRFP670::H2B shown in magenta.

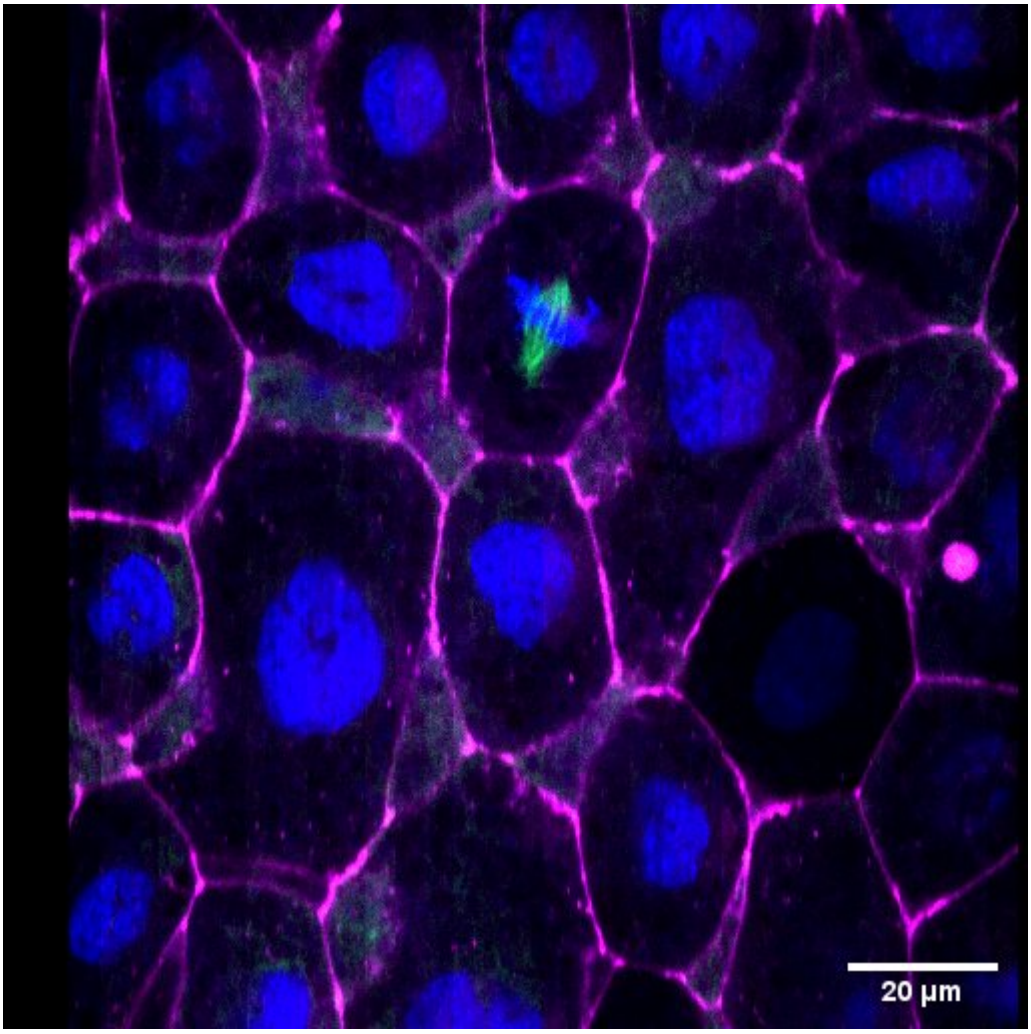

Figure 2.5: Frame from a video of mitosis in live transgenic Xenopus embryo showing the separation of fluorophores. Wherein we can see the cellular membranes (magenta) labeled with mTagBFP::CAAX; chromatin (blue) labeled with miRFP670::H2B; and mitotic spindles (green) labeled with mCherry:α-tubulin. The image was captured with a sCMOS detector and filter configuration 2 (see section "System Dichroics and Emission Filters") frames were taken every minute with a 60x oil objective and excitation at 405 nm, 561 nm, and 640 nm.

Discussion

Our Amici prism dispersion element can be integrated into an existing multipoint confocal design, such as the Opterra multipoint confocal (Bruker Nano Surfaces FM, Madison, WI), if post-processing code is utilized to compensate for the effects introduced with the prism. It adds spectral resolution while only moderately impacting other important parameters of the system,

most importantly the sensitivity and capture speed, but requires multiple computational corrections post-collection which can slow down processing speed. Our analysis (Figure 2.1) shows that the bulk of added noise is introduced by the additional required detection readouts. The readout noise is dependent on the gain applied to the camera and this difference can be small for high EM amplification factors and could disappear in a photon counting setup. The noise consequences of the Amici prism are hard to detect (if at all) by simple visual analysis of the images. We conclude that in most practical cases, the losses due to spectral capture are so small that there is no need for regular (non-spectral) confocal capture, if proper calibration is done. Traditional monochrome images can still be created from the hyperspectral data if desired, but the available additional spectral information can still be accessed if needed. The only scenario that still requires traditional monochrome or filter based capture is if frame rates exceeding 27 full frames per second are required or if a live processed image is desired. Specifically, the live view in the spectrally split mode is visually difficult to determine any useful information before processing.

Spectral PSF

Apart from the technical limitation of the achievable pixel size, the spectral resolution of our system is limited by the optical point spread function (PSF) of the Amici prism spectrometer. The width of this PSF is expected to be proportional to the size of the pinhole in use. The spectra of a monochromatic source imaged using different pinholes (shown in S2.1 Fig) indicate that the point-spread function of our system is smaller than a pixel of our current camera. If the spread of the peaks shown in the figure was due to the system PSF, the peak would have to be twice as wide for a 60 micron pinhole as it is for a 30 micron pinhole. The widths are however practically identical. We attribute the detected spread to electron leakage between adjacent EMCCD pixels.

Once the camera resolution approaches the spectral PSF, spectral resolution could be further increased by insertion of a longer beam path for the Amici prism along with a mask with fewer pinholes. This would sacrifice speed to improve spectral resolution. It may also be possible to place two or more Amici prisms in series to allow additional flexibility in the choice of spectral resolution.

Prism spectrometers are typically nonlinear in their mapping of frequency to separation distance. The Amici prism used was designed to minimize nonlinearities using Zemax simulations. Linearity was also tested with the different calibration methods. The prism is found to be linear to within the current resolution of the instrument and the calibration methods used (17 nm per channel) (Fig. 2.2c).

Spatial PSF

The spatial point spread function is not affected by the insertion of the Amici prism and the reconstruction process. The point spread function in all dimensions on a reconstructed hyperspectral image is shown in S2.2 Fig. A direct comparison of the PSF of the standard swept field confocal microscope with the PSF of a spectral channel is shown in S2.3 Fig.

Capture Speed

The capture speed of the Amici multipoint system is directly related to the frame rate of the readout camera. The Hamamatsu ORCA Flash4.0-V2 provides the current (2020) state of the art of 400 full frames per second at 512 by 512 pixels resulting in about 27 hyperspectral images per second. In addition to future faster readout cameras, the hyperspectral frame rate could be increased through binning or the use of regions of interest, resulting in an improved frame rate at the expense of spectral or spatial resolution or field of view. It is also possible to undersample the images by taking less than the required 16 frames to compose one image. For example, using 2x2 binning and capturing 8 frames per hyperspectral image would halve the spatial and spectral resolution but provide about 50 spectral images per second. These are the raw capture speeds, if a live video feed that has been processed is needed, the bottleneck will be the processing speed of the algorithm since the current implementation is designed for bulk post-capture processing.

The shorter exposure time for raw images can improve the effective resolution of the images by reducing motion blur even if the acquisition process does not require a fast continuous capture. This is shown in Fig 2.5 in an image of an oocyte cell during mitosis captured with a 60X oil immersion lens and 75ms exposure time. While longer exposure times make the image seem less noisy, details like the dynamic microtubules are only discernible in the short exposure image due to motion blur.

Spectral Resolution

We achieve a spectral resolution of about 17 nm per channel over 15 channels. The spectral resolution is determined by the pixel pitch of the readout camera (in this case the ORCA-Flash4.0 V2, Hamamatsu, Hamamatsu City, Japan) Other camera models like the QImaging Rolera EM (QImaging, Surrey, BC, Canada) have roughly half the pixel pitch of our currently used cameras and would double the spectral resolution to about 30 channels and 8.5 nm per channel. The spectral bandwidth of about 255 nm could be adjusted by designing a different Amici prism.

High Speed Spectral Resolution

Hyperspectral images eliminate the need for specialized fluorophore dependent filters and allow the selection and adjustment of spectral filtering after the capture process. Much of the potential of hyperspectral datasets may be realized through our post-capture computational spectral analysis. With our automated method (see https://github.com/uw-loci/SSFC/) acquiring a 3D spectrally split data cube with multiple time points is easy with the further benefit of being readily usable for further analysis through FIJI and other image analysis tools. These tools can be used to extend the information extracted from samples and explore further elements of the data set.

Application to Spinning Disc Multipoint Confocals

Spinning disc multipoint confocals use a rapidly spinning disc with separated pinholes to scan the sample rather than scanning an array of pinholes using mirrors. The pinholes are arranged

such that after one rotation of the disc the entire sample has been scanned and a complete continuous image has been projected onto the readout camera. It is conceivable that a spinning disc system using an Amici prism could be devised. For example, a typical spinning disk system has a field of view that at any one time passes through an arc of around 1/12 of the circumference of the disk. The aperture pattern on the disk could be arranged such that at each 30-degree sector the apertures sweep lines spaced 12 pixels apart. The intervening pixels can then be used to read out the spectral channels separated by an Amici prism as we describe. When one sector has been completed the camera is read out. The pinholes in the next sector are displaced one pixel radially. The procedure is repeated for this sector. In this manner all twelve sectors in a revolution are sequentially read out and an image with 12 spectral channels assembled. The number of spectral channels could be increased using a larger disk where the field of view is contained in a smaller angular width, thereby giving more sectors.

Extension through Linear Unmixing

If there is spectral overlap between multiple markers in a sample, those markers will appear together in several channels. In the presence of this crosstalk, signal processing techniques are required to isolate the signals of individual fluorophores. Many approaches are available for the unmixing of spectral information, often transferred from fields that also commonly utilize hyperspectral data [51,52]. One approach applied in gamma ray spectroscopy and analytical chemistry is known as spectral stripping and allows the removal of strong unwanted known spectra by subtracting them from the collected data [53]. A hyperspectral image containing only the emission of known fluorophores can be expressed as a superposition of a set of known fluorophore spectra. Which can be used to separate the fluorophores in the image. This technique is known as linear unmixing [33,54] and is widely employed in spectral analysis of microscopy data. Since this method requires a priori knowledge of the dye spectra, it is however not suited for samples with unknown fluorescent emitters.

More importantly, small variations in the fluorescence spectrum as frequently occur in response to such factors as different chemical environments, embryonic developmental stage, and refractive effects in the sample can decrease the performance of the methods [55]. The methods will also fail if the system is not sufficiently calibrated and detected spectra no longer match the reference spectra in the library (for example because of the effects of any excitation blocking filters). This is a common problem of unmixing methods that is difficult to diagnose and rectify. It is especially challenging in the analysis of live samples where the sample preparation is time consuming, has significant potential for errors, and a large, expected variation in different samples.

A cytofluorogram [9] is a simple method that allows the separation of small numbers of unknown dye spectra. This method has also been used to handle changes in dye spectra due to chemical environment and can be implemented through Nonnegative Matrix Factorization (NNMF) [56]. NNMF is available as a MATLAB (MathWorks, Natick, MA) software function. Approaches similar to NNMF, such as Multivariate Curve Resolution, have been applied to microscopy data of high spectral resolution [57,58]. We find that for low noise spectral data of limited complexity, NNMF can be implemented and used to separate overlapping fluorophores. To illustrate this, a

test specimen of Focal Check Green-Green double stained fluorescent beads (Life Technologies, Carlsbad, CA) is shown in S2.4 Fig along with the result of a three-component nonnegative matrix factorization. The beads are 6 microns in diameter and contain a dye with a fluorescence peak at 525 nm in their core and a dye peaking at 512 nm in their shell [29,59]. The spectra were found and separated without significant crosstalk by the algorithm in the regions where the spectra were not saturated (see S2.4 Fig). Saturation is present in the center of the image and prevents the separation. More involved methods are a subject of further research and beyond the scope of this publication that focuses on the capabilities of the capturing hardware, performing spectral separation only as a means of assessing the system performance.

We present a multipoint confocal microscope with 15 channel spectral resolution captured efficiently, without degrading the speed and sensitivity of the system and spectral analysis software to correct and process the raw data into a usable data cube. Spectral and spatial data are orthogonal sources of information. Increasing spectral resolution therefore significantly increases the information content obtained from microscope images. Putting this information to optimal use is, however, not trivial. The establishment of new techniques in microscopy and data processing are driven by availability and wide acceptance by the biomedical community. We believe that the facility of hyperspectral imaging in light microscopy will enable users to explore this rich information source and find applications beyond current uses, for example in the adoption of new intrinsic and extrinsic fluorescent labels.

Conclusions

This approach leverages the intrinsic unused space of the detection camera in a multipoint confocal setup. As such it is capable of capturing a higher density of information than normal multipoint confocals. Making it an attractive option to retrofit onto existing systems. Whilst we present a functional image processing algorithm for image reconstruction. Future work can integrate and streamline this processing into the acquisition software, thereby enabling a real-time view of the sample, and decreasing the time between data acquisition and analysis.

Materials and Methods

The Opterra scan head

We modified the scan head of an Opterra multipoint swept field confocal (SFC) microscope [8,60,61] (Bruker Nano Surfaces FM, Middleton, WI) combined with a CMOS readout camera (ORCA-Flash4.0 V2, Hamamatsu, Hamamatsu City, Japan). We also tested this with an EMCCD readout camera (Photometrics QuantEM and Photometrics Evolve Delta, Photometrics, Tucson, AZ). Laser excitation sources at 405 nm, 488 nm, 561 nm, and 640 nm were incorporated in our prototype. The beam path inside the scan head is shown in Fig 2.6. The excitation light is directed through a set of 32 pinholes and focused on the sample via a dichroic mirror (Chroma zT405/488/561/640rdc or Chroma z488rdc). A series of disconnected points in

the sample is illuminated, and the excited fluorescence is imaged through a second set of apertures onto the sensor. An emission filter can be inserted to remove unwanted excitation light from the image. The scan head has a galvanometer actuated mirror to scan the illuminated points horizontally, and a set of piezo scanning mirrors to direct the beam vertically. In normal operation the system sweeps an entire line across the sensor with the galvanometer, exposing a series of non-contiguous lines on the sensor (Fig 2.6d). After exposure, piezo mirrors shift the beams vertically by one row and horizontal scanning with the galvanometer is continued. This process is repeated 32 times until a complete continuous plane in the sample has been exposed. The image can then be read off the camera or the exposure process can be repeated to accumulate more light. The image creation process is outlined in Fig 2.6. This is adaptable onto any multipoint confocal system by altering the number of exposures as dependent on the number of pinholes.

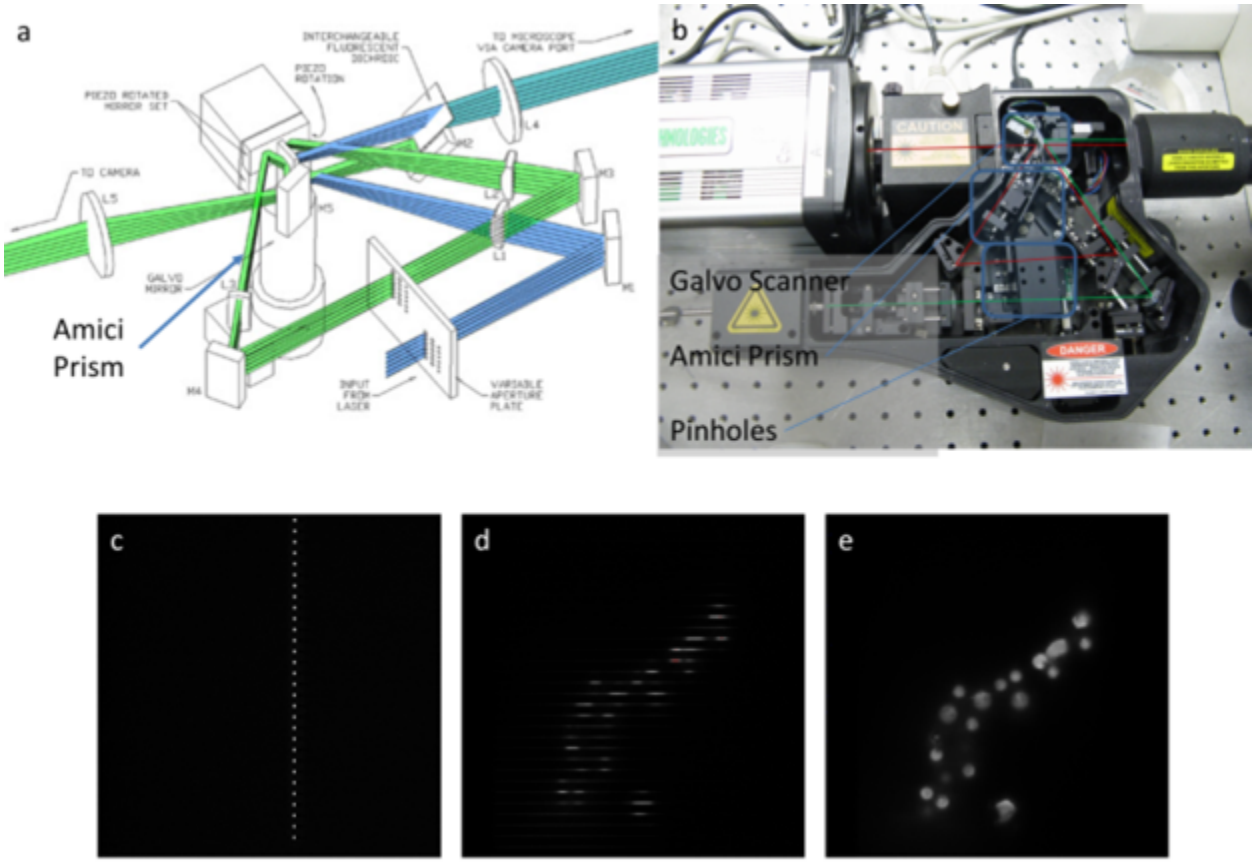

Figure 2.6: Hardware setup and monochrome image acquisition. (a) Schematic of the Opterra multipoint confocal scan head. (b) Photograph of the scan head with the prism and the EMCCD. The prism is mounted on a plunger and can be moved in and out of the beam path. (c) Image captured by the readout EMCCD when the beam scanners are inactive. (d) Image captured by the readout EMCCD while scanning only with the horizontal (galvanometer) scanners. (e) Image

captured by the readout EMCCD while scanning both the horizontal and the vertical (piezo) scanners.

The Amici prism

We reversibly modified the scan head by inserting a four component double Amici prism for separation into spectral components into the beam path. Three component Amici prisms have originally been used for the investigation of stellar spectra and today find application as compact wavelength discriminators, such as handheld spectrometers. They are inexpensive and provide wavelength separation without changing the mean beam direction and with minimal loss. We add a fourth component to the prism design to improve the linearity of the spectral separation. The light path inside the prism is shown in Fig 2.7. The prism consists of four wedges of different materials with different refractive indices and dispersion characteristics bonded together with UV cured optical cement. The entrance and exit faces are coated with a broadband multilayer anti-reflection coating. A simpler design of an amici prism consists of just two materials and translates the optic axis upon transmission. To distinguish from this configuration, the three-prism configuration our system is based on is often referred to as a double amici prism. We use the term Amici prism for brevity but always refer to our modification of the more advanced three component design by Amici. This prism is designed to pass a central wavelength of 561 nm without deflection while other wavelengths are deflected as indicated in Fig 2.7 with linear dispersion over the range 450-700nm (Fig 2.7c). We measured the overall transmission of the prism to be 94% at 632 nm. The loss is mostly due to residual reflectance and scattering in the interfaces between different wedges, as well as the entrance and exit interfaces. This dispersion requires mapping and binning in post-processing to enable image reconstruction from the captured images. The Amici prism can be moved in and out of the beam path using a plunger.

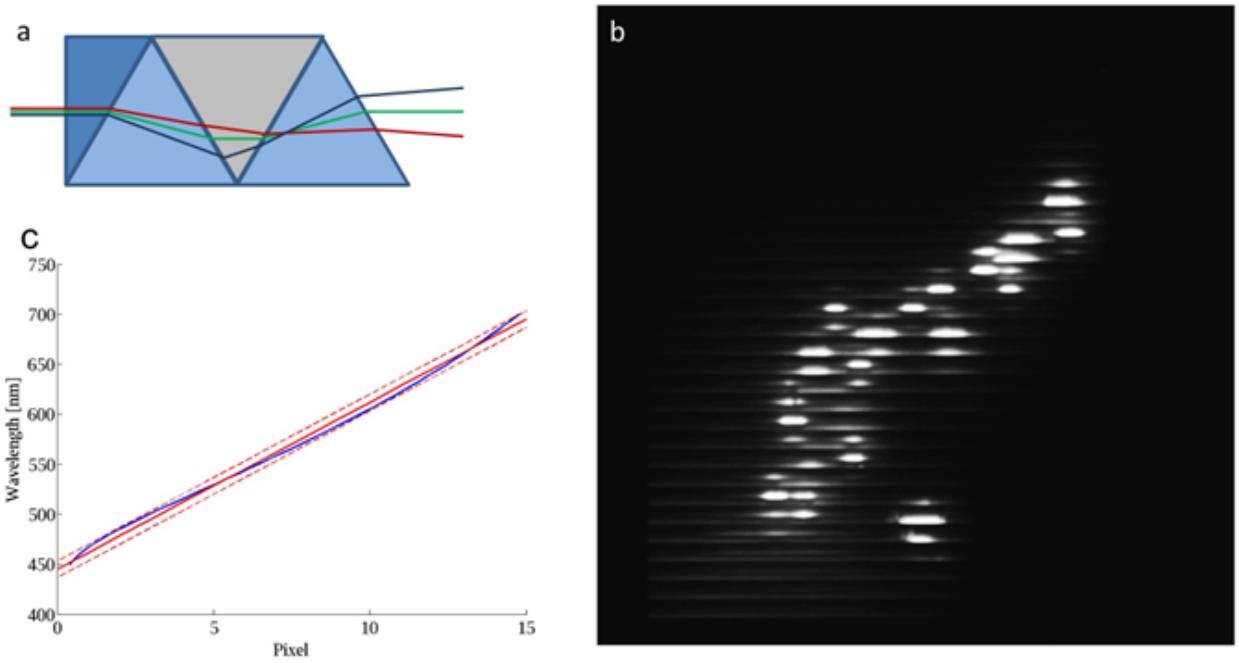

Figure 2.7: Wavelength separation with the Amici prism. (a) The Amici prism is a compound prism that separates different wavelengths without changing the beam direction. (b) When the Amici prism is in the beam path, an image exposed while operating only the horizontal (galvanometer) scanners contains the spectra of 32 lines in the sample. (c) Spectral separation of the Amici prism on the detector simulated with Zemax (blue line). The pixel pitch is 16 micron. The red line indicates an ideal linear separation and the dashed red lines delineate an area of pixel or spectral channel around the ideal. The Amici prism is thus linear within the spectral resolution of our microscope.

Image Capture and Reconstruction

After readout, the piezo actuators adjust the field of view horizontally to image an adjacent set of lines in the sample. A second set of spectra is read out as a spectral image . This process is repeated until a continuous region of the sample has been imaged. The result is a frame stack s_{ijk}. The data are then processed to obtain a stack M_{abl} of images of 15 spectral channels by rearranging the elements according to

$$a = fix(\frac{j}{15}) + k$$

$$b = j$$

$$l = mod(j, 15)$$

This simple treatment assumes that the separation between different pinholes is exactly 15 pixels throughout the sensor area. If this assumption does not apply, aliasing effects need to be taken into account if sub pixel accuracy is desired. The false color rendering of a reconstructed image of fluorescent beads, along with the 15 individual color channels is shown in Fig 2.8.

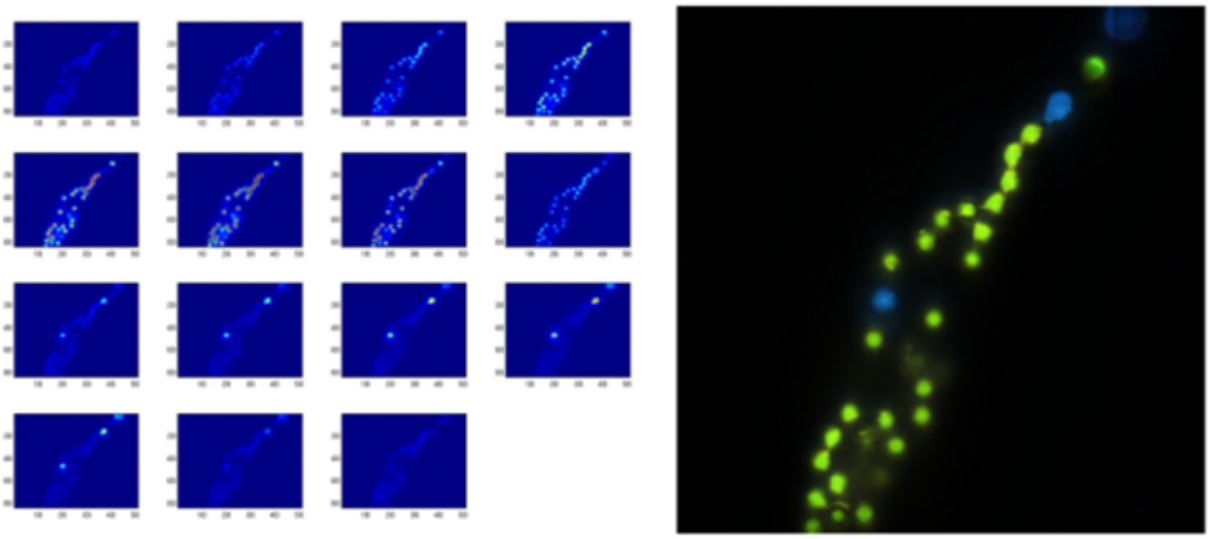

Figure 2.8: The 15 Spectral channels of a sample of fluorescent beads (Molecular Probes F-21010 and F-8842), as well as a false color rendering. Captured with EMCCD detector and filter configuration 1 (see section “System Dichroics and Emission Filters”).

Image Processing

To reconstruct an image from the captured data all the calibration images are analyzed for tilt. This is since with the plunger mounting, the amici prism is not guaranteed to be inserted perfectly vertically in the optical path and therefore can cause the spectral lines to be tilted. This tilt needs to be corrected for further processing to succeed and is performed using a Hough transform. All captured images are corrected for any tilt discovered using this method. Then using the wavelength calibration described later every pixel is assigned a wavelength and a pinhole. The wavelengths are used in Otsu’s method for determining optimal thresholds on wavelength bin counts gathered from the wavelength maps and the captured images to determine optimal bounds between the fluorophores discovered in the sample [62,63]. These bounds are used to convert the calibrated wavelength mapping into binning masks. Every captured image is split into its spectral bins with these masks. Then the split sub-images from individual imaging positions are combined to build a reconstructed image of each spectral bin at that imaging position. These spectral image stacks are then combined via mosaicking to generate a single image cube (X, Y, Z, T, C) of the captured data set that is spectrally split. The

implementation of this process for this microscope is available at:
https://github.com/uw-loci/SSFC/

System Dichroics and Emission Filters

We implemented two dichroic/filter configurations to prevent light from the excitation laser from being detected by the camera: (1) A dichroic filter directing the excitation laser at 488 nm (Chroma z488rdc) to the sample with a filter bandwidth of ±10 nm and passing all other light between 400 and 800 nm back to the camera. This dichroic is combined with a 500 nm long pass emission filter (Chroma ET500LP) placed directly in front of the camera. In this configuration the system uses only the excitation laser at 488 nm and can capture light from 500 nm to 800 nm. (2) A dichroic mirror (Chroma zT405/488/561/640rdc) designed for excitation at 405 nm, 488 nm, 561 nm, and 640 nm, again with a width of about ±10 nm for each wavelength. This dichroic also acts to block the four excitation wavelengths at the camera. In this configuration all four excitation lasers can be used in parallel and light across the entire sensitivity range of the instrument from about 400 nm to about 800 nm can be collected. At the excitation wavelength, no light is detected. Custom dichroic designs can be used to minimize the spectral width of the components blocked in this process. The current width of 20 nm creates clearly visible dips in the collected spectra. The spectral width of the lasers used is less than 5 nm. Custom designed dichroics may reduce the bandwidth of the blocked light to about 5-10 nm, which is less than the width of one channel in the microscope. Rather than being completely blocked, the affected channels then detect a reduced amount of light, which can be compensated in post processing at the expense of additional noise in those channels.

Ghosting Correction

Each pinhole has assigned to it 15 pixel rows on the CMOS sensor corresponding to 15 color channels. At about 17 nm per channel, this corresponds to a spectral bandwidth of about 255 nm. By selecting which 15 sensor rows are assigned to which pinhole, it is possible to computationally adjust which 250 nm band within the sensitivity range of the microscope should be imaged. If the light emitted by a sample exceeds the 250 nm bandwidth, we observe ghosting in which the red light of a certain pinhole falls onto the same pixel row as the blue light of an adjacent pinhole. This effect is only apparent in the images when bright spectral signatures at the extremes of the spectral range of the instrument are encountered. It can in some situations be avoided by computational selection of appropriate wavelength bins or by choice of appropriate excitation lasers and fluorophores in a sample. It could also be removed by a 250 nm wide band pass filter placed in front of the camera. In practice we used a filter with a pass band from 450 nm to 650 nm (Semrock, Rochester, NY) since it is available as off the shelf item. In addition, we are investigating approaches to computationally remove this effect in certain situations. None of the specimens presented in this work required this filter.

Oversampling

To obtain a continuous image, the scanner piezos need to advance the field of view by, at most, the equivalent of one camera pixel between captures. Since the images of different pinholes are

approximately 15 pixels apart, 15 images have to be taken. We have the option to adjust the step in scope piezo voltage along with the number of captured images to allow us to zoom the image in one dimension. For example, we can capture 30 frames for one image, moving the field of view by the equivalent of about ½ pixel between captures. The resulting image then contains 15 channels with a spatial resolution of 512 by 1024 pixels. In the images presented here a slight oversampling was chosen so that 16 on the CMOS and 18 on the EMCCD make up one image.

Wavelength calibration

The beam path through the scan head has been simulated with Zemax software (Radiant Zemax, Redmond, WA) and wavelength separation is designed to be approximately linear. Due to the complexity of the setup and the unpredictable effects of potential small alignments in any of the components, it is necessary to calibrate the system using a known source after insertion of the Amici prism. The calibration method uses the excitation lasers of the microscope. For calibration, a reflective slide is placed on the sample holder and the emission filter is removed. Individual frames are captured with each of the excitation lasers illuminating the slide. The resultant calibration data is shown in Fig 2.9. These images are then used for calibration. First, we use a Hough transform to determine whether how the prism was inserted is causing any deviation from horizontal or vertical lines in our readout (prism angle). Any deviation is corrected for by rotating the image by the prism angle. Then we determine the number of pinholes in the image by summing the dimension perpendicular to the pinhole spread and finding the number of peaks and their locations for each calibration image. With this information we generate a linear fit and use it to assign each pixel in each pinhole's band a wavelength. Finally, we create a 512 by 512 pixel map assigning a wavelength and pinhole to every pixel of the readout sensor. This method must be used before or immediately after each sample capture.

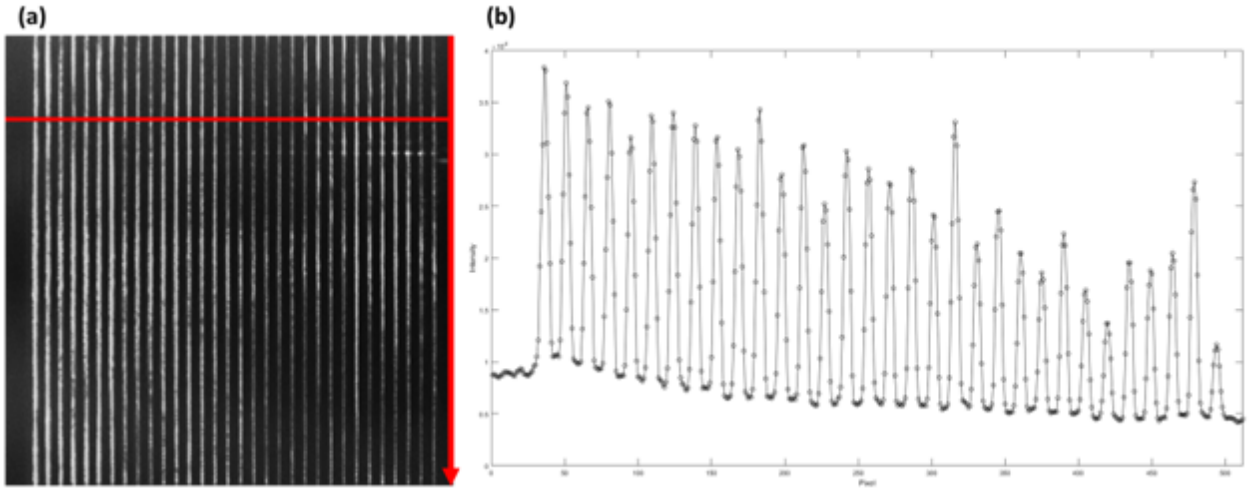

Figure 2.9: Calibration Data. To calibrate and test the microscope we image a reflective sample. Subfigure (a) shows a single frame taken of a calibration data set at 561 nm. Subfigure (b)

shows the sum of all columns in (a) The positions of the 32 peaks in this plot, are the positions on the sensor where 561 nm light from the 32 pinholes is detected.

Pinhole Selection

Three different pinhole sizes are evaluated by imaging the spectrum of a red laser diode. The diode illuminates a diffuser placed on the specimen holder of the microscope. The spectrum of the laser measured by the CCD is shown in S2.1 Fig for different pinholes. The results indicate that the 45 micron pinhole offers the best tradeoff between resolution and signal strength for a 40x lens (NA 1.3).

Color Rendering

To render images in false color, we generate a transform matrix that converts a 15-element vector into a 3 element RGB pixel value. For a true color representation the matrix is composed of the 15 element absorption spectra of the three kinds of cones in the human eye. A simpler transform is a 3x15 identity matrix mapping channels 1 to 5 to red, channels 6 to 10 to green and channels 11 to 15 to blue. False color images computed with an identity matrix along with selected individual spectra are shown in Fig 2.3. For false color renderings in all other images, the mapping is adjusted to map the channels that contain the respective fluorophore contributions to the red, green and blue color channels.

Biological Sample Methods

Fixed transgenic Zebrafish

To demonstrate spectral imaging in biologically relevant specimens we use a zebrafish larva from the flk1:GFP vascular endothelial transgenic line [64] stained for glial fibrillary acidic protein (GFAP). The vasculature is labeled with GFP, GFAP is labeled with Alexa 568 (red) and cell bodies are labeled with DAPI (Vector Laboratories, Burlingame, CA). We also use a second fixed zebrafish larva from the sox9b:EGFP transgenic line [65] in which collagen type II is labeled with Alexa 568 (red). The specimen is mounted in Vectashield with DAPI (blue) labeling the cell nuclei.

Cell mitosis in a live Xenopus laevis embryo

X. laevis embryos were prepared as described in Kita et al. [66] Briefly, albino X. laevis embryos were microinjected at the two-cell stage with a 5nl volume of the following mRNA mixture: 40ng/µl mTagBFP::CAAX (farnesylated BFP, which labels the plasma membrane), 14ng/µl mCherry:α-tubulin (which labels the mitotic spindle), and 4ng/µl miRFP670::H2B (histone H2B, which labels chromatin). All mRNA was transcribed using the mMESSAGE mMACHINE SP6 Transcription Kit (Ambion) from pCS2 backbones. Embryos were cultured at 14ºC in 0.1x MMR and imaged approximately 72 hours post fertilization.

Neuronal growth in live zebrafish larva

Double transgenic zebrafish embryos marked by the minimal neurogenin-1 promoter Tg(-3.1ngn:mCherry-caax) crossed with the transgenic line labeled by HB9 promotor Tg(HB9:GFP) were used [67–69]. Embryos were anesthetized in 0.02% tricaine (ethyl 3-amino-benzoate; Sigma-Aldrich, St. Louis, MO) and mounted in 1% low melting agarose in 10 mM HEPES E3 medium as described previously [70]. Anesthetized embryos were settled onto the bottom of a custom-made, glass-bottom slide.

Chapter 2 References

1. Ling R, Tahir W, Lin HY, Lee H, Tian L. High-throughput intensity diffraction tomography with a computational microscope. Biomed Opt Express. 2018 May 1;9(5):2130–41.
2. Kim G, Menon R. An ultra-small three dimensional computational microscope. Appl Phys Lett. 2014 Aug 11;105(6):061114.
3. McNally JG, Preza C, Conchello JA, Thomas LJ. Artifacts in computational optical-sectioning microscopy. JOSA A. 1994 Mar 1;11(3):1056–67.
4. Kam Z, Hanser B, Gustafsson MGL, Agard DA, Sedat JW. Computational adaptive optics for live three-dimensional biological imaging. Proc Natl Acad Sci. 2001 Mar 27;98(7):3790–5.
5. Tian L, Liu Z, Yeh LH, Chen M, Zhong J, Waller L. Computational illumination for high-speed in vitro Fourier ptychographic microscopy. Optica. 2015 Oct 20;2(10):904–11.
6. Waller L, Tian L. Machine learning for 3D microscopy. Nature. 2015 Jul;523(7561):416–7.
7. Auran JD, Koester CJ, Kleiman NJ, Rapaport R, Bomann JS, Wirotsko BM, et al. Scanning Slit Confocal Microscopic Observation of Cell Morphology and Movement within the Normal Human Anterior Cornea. Ophthalmology. 1995 Jan 1;102(1):33–41.
8. Castellano-Muñoz M, Peng AW, Salles FT, Ricci AJ. Swept Field Laser Confocal Microscopy for Enhanced Spatial and Temporal Resolution in Live-Cell Imaging. Microsc Microanal Off J Microsc Soc Am Microbeam Anal Soc Microsc Soc Can. 2012 Aug;18(4):753–60.
9. Demandolx D, Davoust J. Multicolour analysis and local image correlation in confocal microscopy. J Microsc. 1997;185(1):21–36.
10. White JG, Amos WB, Fordham M. An evaluation of confocal versus conventional imaging of biological structures by fluorescence light microscopy. J Cell Biol. 1987 Jul 1;105(1):41–8.
11. Carlsson K, Danielsson PE, Lenz R, Liljeborg A, Majlöf L, Åslund N. Three-dimensional microscopy using a confocal laser scanning microscope. Opt Lett. 1985 Feb 1;10(2):53–5.
12. Paddock SW. Confocal Laser Scanning Microscopy. BioTechniques. 1999 Nov 1;27(5):992–1004.
13. MATLAB [Internet]. The Mathworks, Inc.; 2021. Available from: https://www.mathworks.com/products/matlab.html
14. Sheppard CJR, Shotton DM. Confocal laser scanning microscopy [Internet]. 1997 [cited 2021 Apr 14]. Available from:

https://www.bcin.ca/bcin/detail.app;jsessionid=B80BB1B15FB4613A283AE25B7780F2BA?lang=en&id=181737&asq=&csq=&csa=&ps=50&pId=1
15. Denk W, Strickler JH, Webb WW. Two-Photon Laser Scanning Fluorescence Microscopy. Science [Internet]. 1990 Apr 6 [cited 2021 Sep 3]; Available from: https://www.science.org/doi/abs/10.1126/science.2321027
16. Helmchen F, Denk W. Deep tissue two-photon microscopy. Nat Methods. 2005 Dec;2(12):932–40.
17. Zipfel WR, Williams RM, Webb WW. Nonlinear magic: multiphoton microscopy in the biosciences. Nat Biotechnol. 2003 Nov;21(11):1369–77.
18. Saggau P. New methods and uses for fast optical scanning. Curr Opin Neurobiol. 2006 Oct 1;16(5):543–50.
19. Lam P ying, Fischer RS, Shin WD, Waterman CM, Huttenlocher A. Spinning Disk Confocal Imaging of Neutrophil Migration in Zebrafish. In: Quinn MT, DeLeo FR, editors. Neutrophil Methods and Protocols [Internet]. Totowa, NJ: Humana Press; 2014 [cited 2021 Apr 14]. p. 219–33. (Methods in Molecular Biology). Available from: https://doi.org/10.1007/978-1-62703-845-4_14
20. Petran M, Hadravsky M, Benes J, Boyde A. In Vivo Microscopy Using the Tandem Scanning Microscopea. Ann N Y Acad Sci. 1986;483(1):440–7.
21. Grienberger C, Konnerth A. Imaging Calcium in Neurons. Neuron. 2012 Mar 8;73(5):862–85.
22. Schultz RA, Nielsen T, Zavaleta JR, Ruch R, Wyatt R, Garner HR. Hyperspectral imaging: A novel approach for microscopic analysis. Cytometry. 2001;43(4):239–47.
23. Nagaoka T, Nakamura A, Okutani H, Kiyohara Y, Sota T. A possible melanoma discrimination index based on hyperspectral data: a pilot study. Skin Res Technol. 2012;18(3):301–10.
24. Owen DM, Auksorius E, Manning HB, Talbot CB, Beule PAA de, Dunsby C, et al. Excitation-resolved hyperspectral fluorescence lifetime imaging using a UV-extended supercontinuum source. Opt Lett. 2007 Dec 1;32(23):3408–10.
25. Bertani FR, Ferrari L, Mussi V, Botti E, Costanzo A, Selci S. Living Matter Observations with a Novel Hyperspectral Supercontinuum Confocal Microscope for VIS to Near-IR Reflectance Spectroscopy. Sensors. 2013 Nov;13(11):14523–42.
26. Bini JM, Spain J, Nehal KS, Rajadhyaksha M, Hazelwood V, DiMarzio CA. Confocal mosaicing microscopy of human skin ex vivo: spectral analysis for digital staining to simulate histology-like appearance. J Biomed Opt. 2011 Jul;16(7):076008.
27. Dickinson M e., Bearman G, Tille S, Lansford R, Fraser S e. Multi-Spectral Imaging and Linear Unmixing Add a Whole New Dimension to Laser Scanning Fluorescence Microscopy. BioTechniques. 2001 Dec 1;31(6):1272–8.
28. Lerner JM, Gat N, Wachman E. Approaches to Spectral Imaging Hardware. Curr Protoc Cytom. 2010;53(1):12.20.1-12.20.40.
29. Zucker RM, Rigby P, Clements I, Salmon W, Chua M. Reliability of confocal microscopy spectral imaging systems: Use of multispectral beads. Cytometry A. 2007;71A(3):174–89.
30. Lavis LD, Raines RT. Bright Ideas for Chemical Biology. ACS Chem Biol. 2008 Mar 1;3(3):142–55.
31. Pinaud F, Michalet X, Bentolila LA, Tsay JM, Doose S, Li JJ, et al. Advances in fluorescence imaging with quantum dot bio-probes. Biomaterials. 2006 Mar 1;27(9):1679–87.
32. Rizzo MA, Davidson MW, Piston DW. Fluorescent Protein Tracking and Detection: Fluorescent Protein Structure and Color Variants. Cold Spring Harb Protoc. 2009 Dec 1;2009(12):pdb.top63.
33. Zimmermann T. Spectral Imaging and Linear Unmixing in Light Microscopy. In: Rietdorf J, editor. Microscopy Techniques: -/- [Internet]. Berlin, Heidelberg: Springer; 2005 [cited 2021

Apr 14]. p. 245–65. (Advances in Biochemical Engineering). Available from: https://doi.org/10.1007/b102216
34. Sekar RB, Periasamy A. Fluorescence resonance energy transfer (FRET) microscopy imaging of live cell protein localizations. J Cell Biol. 2003 Mar 3;160(5):629–33.
35. Hockberger PE, Skimina TA, Centonze VE, Lavin C, Chu S, Dadras S, et al. Activation of flavin-containing oxidases underlies light-induced production of H2O2 in mammalian cells. Proc Natl Acad Sci. 1999 May 25;96(11):6255–60.
36. Born M, Wolf E. Principles of Optics: Electromagnetic Theory of Propagation, Interference and Diffraction of Light. Elsevier; 2013. 871 p.
37. Amos WB, White JG. How the Confocal Laser Scanning Microscope entered Biological Research. Biol Cell. 2003;95(6):335–42.
38. Fujita K, Nakamura O, Kaneko T, Oyamada M, Takamatsu T, Kawata S. Confocal multipoint multiphoton excitation microscope with microlens and pinhole arrays. Opt Commun. 2000 Jan 15;174(1):7–12.
39. Buist A, Müller M, Squier J, Brakenhoff G. Real time two-photon absorption microscopy using multi point excitation. J Microsc. 1998 Nov;192(2):217–26.
40. Glazachev YI. Fluorescence Photobleaching Recovery Method with Pulse-Position Modulation of Bleaching/Probing Irradiation. J Fluoresc. 2009 Sep 1;19(5):875–80.
41. Esposito A, Schlachter S, Schierle GSK, Elder AD, Diaspro A, Wouters FS, et al. Quantitative Fluorescence Microscopy Techniques. In: Gavin RH, editor. Cytoskeleton Methods and Protocols [Internet]. Totowa, NJ: Humana Press; 2010 [cited 2021 Apr 14]. p. 117–42. (Methods in Molecular Biology). Available from: https://doi.org/10.1007/978-1-60761-376-3_6
42. Wang Y, Yang B, Feng S, Pessino V, Huang B. Multicolor fluorescent imaging by space-constrained computational spectral imaging. Opt Express. 2019 Feb 18;27(4):5393–402.
43. Hiraoka Y, Shimi T, Haraguchi T. Multispectral Imaging Fluorescence Microscopy for Living Cells. Cell Struct Funct. 2002;27(5):367–74.
44. Strasser F, Offterdinger M, Piestun R, Jesacher A. Spectral image scanning microscopy. Biomed Opt Express. 2019 May 1;10(5):2513–27.
45. Li Z, Suo J, Hu X, Deng C, Fan J, Dai Q. Efficient single-pixel multispectral imaging via non-mechanical spatio-spectral modulation. Sci Rep. 2017 Jan 27;7(1):41435.
46. Elliott AD, Gao L, Ustione A, Bedard N, Kester R, Piston DW, et al. Real-time hyperspectral fluorescence imaging of pancreatic β-cell dynamics with the image mapping spectrometer. J Cell Sci. 2012 Oct 15;125(20):4833–40.
47. Aikio M, Valtion teknillinen tutkimuskeskus. Hyperspectral prism-grating-prism imaging spectrograph. [Espoo [Finland]: Technical Research Centre of Finland; 2001.
48. Herrala E, Okkonen JT, Hyvarinen TS, Aikio M, Lammasniemi J. Imaging spectrometer for process industry applications. In: Optical Measurements and Sensors for the Process Industries [Internet]. International Society for Optics and Photonics; 1994 [cited 2021 Apr 14]. p. 33–40. Available from: https://www.spiedigitallibrary.org/conference-proceedings-of-spie/2248/0000/Imaging-spectrometer-for-process-industry-applications/10.1117/12.194344.short
49. Hanley, Verveer, Arndt-Jovin, Jovin. Three-dimensional spectral imaging by Hadamard transform spectroscopy in a programmable array microscope. J Microsc. 2000 Jan;197(1):5–14.
50. Hagen N, Tkaczyk TS. Compound prism design principles, I. Appl Opt. 2011 Sep 1;50(25):4998–5011.
51. Harris AT. Spectral mapping tools from the earth sciences applied to spectral microscopy data. Cytometry A. 2006;69A(8):872–9.
52. Grußmayer KS, Geissbuehler S, Descloux A, Lukes T, Leutenegger M, Radenovic A, et al.

Spectral cross-cumulants for multicolor super-resolved SOFI imaging. Nat Commun. 2020 Jun 15;11(1):3023.
53. Busch KW, Howell NG, Morrison GH. Elimination of interferences in flame spectrometry using spectral stripping. Anal Chem. 1974 Dec 1;46(14):2074–9.
54. Zimmermann T, Rietdorf J, Pepperkok R. Spectral imaging and its applications in live cell microscopy. FEBS Lett. 2003;546(1):87–92.
55. Neher R, Neher E. Optimizing imaging parameters for the separation of multiple labels in a fluorescence image. J Microsc. 2004;213(1):46–62.
56. Berry MW, Browne M, Langville AN, Pauca VP, Plemmons RJ. Algorithms and applications for approximate nonnegative matrix factorization. Comput Stat Data Anal. 2007 Sep 15;52(1):155–73.
57. Davis LM, Shen G. Extension of multidimensional microscopy to ultrasensitive applications with maximum-likelihood analysis. In: Three-Dimensional and Multidimensional Microscopy: Image Acquisition and Processing XIV [Internet]. International Society for Optics and Photonics; 2007 [cited 2021 Apr 14]. p. 64430N. Available from: https://www.spiedigitallibrary.org/conference-proceedings-of-spie/6443/64430N/Extension-of-multidimensional-microscopy-to-ultrasensitive-applications-with-maximum-likelihood/10.1117/12.702217.short
58. Juan A de, Maeder M, Hancewicz T, Tauler R. Use of local rank-based spatial information for resolution of spectroscopic images. J Chemom. 2008;22(5):291–8.
59. Ducros M, Moreaux L, Bradley J, Tiret P, Griesbeck O, Charpak S. Spectral Unmixing: Analysis of Performance in the Olfactory Bulb In Vivo. PLOS ONE. 2009 Feb 9;4(2):e4418.
60. Bembenek JN, Richie CT, Squirrell JM, Campbell JM, Eliceiri KW, Poteryaev D, et al. Cortical granule exocytosis in C. elegans is regulated by cell cycle components including separase. Development. 2007 Nov 1;134(21):3837–48.
61. Lee TJ, Lee JW, Haynes EM, Eliceiri KW, Halloran MC. The Kinesin Adaptor Calsyntenin-1 Organizes Microtubule Polarity and Regulates Dynamics during Sensory Axon Arbor Development. Front Cell Neurosci [Internet]. 2017 [cited 2021 Apr 14];11. Available from: https://www.frontiersin.org/articles/10.3389/fncel.2017.00107/full
62. Otsu N. A Threshold Selection Method from Gray-Level Histograms. IEEE Trans Syst Man Cybern. 1979 Jan;9(1):62–6.
63. Liu D, Yu J. Otsu Method and K-means. In: 2009 Ninth International Conference on Hybrid Intelligent Systems. 2009. p. 344–9.
64. Thompson MA, Ransom DG, Pratt SJ, MacLennan H, Kieran MW, Detrich HW, et al. The cloche and spadetail Genes Differentially Affect Hematopoiesis and Vasculogenesis. Dev Biol. 1998 May 15;197(2):248–69.
65. Plavicki JS, Baker TracieR, Burns FR, Xiong KM, Gooding AJ, Hofsteen P, et al. Construction and characterization of a sox9b transgenic reporter line. Int J Dev Biol. 2014;58(9):693–9.
66. Kita AM, Swider ZT, Erofeev I, Halloran MC, Goryachev AB, Bement WM. Spindle–F-actin interactions in mitotic spindles in an intact vertebrate epithelium. Mol Biol Cell. 2019 May 15;30(14):1645–54.
67. Flanagan-Steet H, Fox MA, Meyer D, Sanes JR. Neuromuscular synapses can form in vivo by incorporation of initially aneural postsynaptic specializations. Development. 2005 Oct 15;132(20):4471–81.
68. Andersen EF, Asuri NS, Halloran MC. In vivo imaging of cell behaviors and F-actin reveals LIM-HD transcription factor regulation of peripheral versus central sensory axon development. Neural Develop. 2011 May 27;6:27.
69. Blader P, Plessy C, Strähle U. Multiple regulatory elements with spatially and temporally distinct activities control neurogenin1 expression in primary neurons of the zebrafish embryo. Mech Dev. 2003 Feb 1;120(2):211–8.

70. Andersen E, Asuri N, Clay M, Halloran M. Live Imaging of Cell Motility and Actin Cytoskeleton of Individual Neurons and Neural Crest Cells in Zebrafish Embryos. J Vis Exp JoVE [Internet]. 2010 Feb 3 [cited 2021 Apr 14];(36). Available from: https://www.ncbi.nlm.nih.gov/pmc/articles/PMC2818709/

Chapter 3: Sequential Erosion of Tissue Imaging (SETI)

With the inherent problem of imaging optically thick samples, computational microscopy has worked to provide solutions. One of the main approaches for imaging a whole thick sample is by pairing a confocal with a microtome [1–5]. The microtome generates thin slices from the sample which are then imaged sequentially by the confocal microscope. These images are then reconstructed into a 3D data cube that can be analyzed. While this works, it is a very expensive piece of equipment. As such we present a computational microscope that is significantly cheaper and open source. By combining a CNC mill, a fluorescence microscope, and a digital light projector (DLP), we can build a sectioning system using structured illumination for background rejection [6–8].

While the core hardware of the system was developed by prior grad students, the out of plane fluorescence was significantly interfering with the system's signal. Therefore it became apparent that a background rejection approach was needed [6]. Normally structured illumination is done using either a Spatial Light Modulator (SLM) [9–13] which is placed into the optical path or a Digital Light Projector (DLP) [14–17] which is imaged onto the sample. While using a DLP for structured illumination is not novel in itself, this is the first system that combines it with a physical sectioning approach. To support this prototype system, I wrote open-source steering and analysis scripts in Micromanager and MATLAB respectively [18–20]. These scripts can form the basis for future combinations of physical and structured illumination optical sectioning.

To generate the structured illumination a digital light projector (DLP) is used. DLP's are commonly used in projection systems and are not designed for plug'n'play usage in a microscope. As such multiple DLPs were tested to find one that suited this purpose. We tried four DLPs: the PicoProjector from Texas Instruments, the LightCrafter 2000 from Texas Instruments, the IPD1865SL from iView Displays, and finally the DLP Evaluation Board 4500 from Texas Instruments. These four were tried in the system. The PicoProjector had the smallest form factor, but burned out during usage [21]. From this it was upgraded to the LightCrafter 2000. This DLP required some modification to be used in the system but was usable once its front optics had been removed. It also generated more lumens with a max around 100 lumens [22,23]. Unfortunately it was unable to completely fill the back aperture of the objective. This led to the testing of the IPD1865SL DLP which was more than capable of filling out the objectives back aperture and produced a max of 1700 lumens with 1920x1080 resolution [24]. While the light engine and projection optics have a form factor that theoretically fits with the system, once the necessary heat sinks and controller boards were added, it was significantly too big for the system. Finally we tested the DLP 4500 Evaluation Board which is significantly smaller than the IPD1865SL, and has 1280x800 resolution and completely fills the back of the objective aperture [25]. It does require a wedge and custom mounting plate to

compensate for its throw angle, but these can be readily 3D printed. Based on all these considerations, we decided to utilize the DLP 4500 Evaluation Board.

Additionally a significant problem with this approach was found in terms of the embedding media used. While the testing of the DLPs improved our imaging capabilities, we found that our initial embedding methodology using JB4 was causing significant deterioration in the image quality [26]. While there are many papers on optimizing tissue samples for microtomes/vibrotomes, or thin tissue samples for electron microscopy, there is no paper focused on embedding thick tissue samples for milling purposes [27–42]. As such we tried multiple embedding methods as were either recommended or available in the lab for our purposes. Through our testing we found no clear solution amongst the common embedding methods. The approach we ended up using was utilizing EpoFix Embedding on samples cut into the shape of core biopsies then imaging the centers which were not infiltrated by the EpoFix, but would not have significant deformation due to the milling process since they are tightly gripped on their edges by the resin.

Adapted from “Sequential Erosion Tissue Imaging with Structured Illumination for Imaging Thick Fluorescent Fixed Samples” Gahm, Niklas A., Gahl, Zachary, Ma, Yiqun, Cox, Benjamin L., Bredfeldt, Jeremy S., Velten, Andreas, Zeman, Jessica, Petry, George, Swader, Robert, Sagar, Md Abdul Kader, Mackie, Thomas R., Skala, Melissa C., Eliceiri, Kevin W. JBO (will be submitted to JBO within the next week)

Abstract

Significance: We present a computational optical platform that combines physical and optical sectioning for deep imaging into thick fluorescent fixed samples.
Aim: A standard upright fluorescence light path coupled to a digital light projector (DLP) as the light source is used to achieve optical sectioning through structured illumination.
Approach: The optical system is used to image the top surface of fixed embedded biological samples before they are physically sectioned via a mill which erodes away the top surface of the sample. This process is repeated for the whole sample to generate a volumetric data set.
Results: The resulting open-source prototype demonstrates the benefits of speed and low cost in using a mill with structured light illumination. The capacities of this approach are demonstrated on fluorescence beads, GFP expressing tumors, and GFP expressing plant roots.
Conclusions: This system can currently handle certain configurations of embedded thick fluorescent samples as presented, however, more work can be done to remove the constraints

caused by embedding. The open-source nature of the system can provide a basis for further development of mill-based sequential erosion tissue imaging systems.

Keywords:

Optical Sectioning, Physical Sectioning, Fluorescence, Embedding

Introduction

Fluorescence imaging is widely used in research as it can precisely visualize fluorescently tagged proteins and help correlate genetic expression with biological function[43]. It utilizes molecules which can be excited by a photon to a higher energy state before they decay back to their ground energy state releasing a photon of lower energy. These molecules have found widespread usage in research settings since they can be used to tag specific structures and proteins in biological samples[44]. However, these probes run into a depth limitation where, even if the sample is fully labeled, at some depth into the sample the system cannot get enough light down to the layer being imaged nor get light back from the fluorophores. This is particularly problematic in thick samples where valuable information can be deeper than the first few hundred μm from the sample surface than conventional optics can access[45,46].To address this depth need, physical sectioning can be used to remove the surface layer of tissues that have been imaged, revealing the deeper layers for subsequent imaging. This methodology has been popularized with electron microscopy where an electron microscope is coupled with a microtome to generate the physical sections[1,2,5,47]. Fluorescence is widely used in histopathology research samples so effective ways to physically and optically section fixed thick samples is of great interest [48–50]. There have been innovative approaches such as array tomography for neural circuitry studies where the physical sectioning and the imaging are decoupled processes and the sample is sectioned into an array of sequential slices which is then imaged with optical and electron microscopy[3]. Typically, thick sample imaging is not used with standard fluorescence microscopy due to challenges of getting out-of-field noise due to out-of-plane signal. Optical sectioning techniques like confocal and multiphoton laser scanning microscopy resolve this issue by methods of pinhole rejection and selective excitation respectively and have been successfully coupled with physical sectioning[46,51–55]. However, these systems are expensive and not accessible in most lab settings. Block face machine milling presents an accessible alternative to the techniques that require more sample preparation and equipment expertise such as microtome sectioning, vibratome sectioning, or ion ablation via a focused ion beam. Although it is a destructive technique like ion ablation, machine milling provides an advantage by lessening the amount of preparation needed for proper sectioning because it does not require the use of harsh chemicals and a microtome to provide an initial surface[56–58]. This technique is also advantageous from a training and operation perspective as it does not require the same level of tedious expertise as the microtome or vibratome. Furthermore, microtome-based sectioning can have problems with warping and loss of sections and, due to the nature of cutting non-embedded tissues, vibratome sections are limited in thickness ranging from tens to hundreds of microns[59–61]. These issues present a significant problem for generating an accurate volumetric data set. Therefore, machine milling is

much more efficient in terms of sample preparation, training time, and operation time and a more reliable method of sectioning for accurate volumetric data.

There could be improved cost and usability access if a physically sectioning approach could be coupled to the simple widefield fluorescence microscope. The out-of-focus light problem in wide-field fluorescence microscopy can be addressed by coupling the physical sectioning system with structured illumination microscopy to allow for deeper imaging into intact samples[6]. Structured illumination microscopy is a technique that can image below the surface of the sample by changing the plane of focus and rejecting the light from out-of-plane fluorophores, thereby collecting data from inside the sample. However, optical sectioning techniques face intrinsic challenges of light scattering and refractive index changes increasing with imaging depth due to the optical properties of biological samples.

To study this approach a prototype sequential erosion tissue imaging (SETI) system was built that can obtain fluorescence images at much higher depths than traditional fluorescent or multi-photon imaging by combining structured illumination microscopy with physical sectioning all while keeping the advantages of fluorescence microscopy with the speed advantages of a mill. The combination of physical sectioning and precision fluorescence imaging is achieved by integrating a standard CNC mill with the structured illumination imaging system. This combination is a novel approach, since while other groups have used an integrated mill in a fluorescence microscope setup with cryo based milling and sectioning, they are not coupled with optical sectioning[4,62]. The milling approach can offer many advantages of cost, speed and precision. However it also means that the sample has to be hard, not just fixed. So we explore the potential of using embedding mediums, many from the electron microscopy world.
Large samples that need to be physically sectioned are often embedded in paraffin wax or a plastic resin-based material. However, embedding large samples has continued to present challenges to microscopic imaging due to the chemicals changing cellular morphology and target protein structure. Plastic embedding is preferred over paraffin wax due to the shrinkage of the embedded tissue in paraffin[63,64]. Also, each plastic resin is different in its ability to infiltrate large samples and preserve the intensity of markers like fluorescent proteins[65]. Furthermore, resins range from standardized materials like Epofix, JB-4, or SPURR to niche materials with lengthy procedures[66–69]. As a result, a wide range of embedding resins are available for use in both optical and electron microscopy, but there is also a wide range of issues when trying to select an appropriate medium for physical sectioning. Many times sample fluorescence is quenched, tissue morphology is altered, or, most importantly, the medium cannot withstand physical sectioning via a mill because it is too soft or brittle. Therefore, it is difficult to find an effective embedding method that is not specialized for a specific sample type. We present the issues of working with this type of sample preparation and what is achievable with current embedding substrates. Furthermore, the prototype has been developed as a fully automated open-source hardware platform controlled by open source acquisition including on Micro-Manager[18], G-code, Arduino, and MATLAB. By utilizing a conventional CNC mill, standard upright fluorescence optical components, and an off-the-shelf DLP, this prototype provides a starting point for exploring much more affordable, adaptable, and deeper imaging than technologies like multiphoton microscopy. By marrying physical sectioning, computational

optics, and fluorescence imaging, high-quality imaging of very thick tissues can be achieved, while maintaining ease of use and affordability.

Materials and Methods

Sample Preparation

To prevent deformation through the milling process the sample needs to be embedded in a hard resin or epoxy. The exact resin to be used is dependent on the sample being imaged. Due to the nature of using milling as the physical sectioning approach, soft embedding media such as paraffin does not work since the mill will cause deformation of the media and sample. As well it is important to find an embedding medium that is not only hard enough to mill but also does not negatively impact the tissue structure or fluorescence signal To our knowledge this challenge has not been investigated before as most previous tissue embedding studies were for electron microscopy studies and not for fluorescence microscopy.

Fluorescence preservation and image quality in thick fixed samples are at the core of producing useful data with this computational optical milling prototype. As such, finding the best resin, acrylic or epoxy, that could withstand a mill, preserve fluorescence for imaging, and maintain fluorescence signal and optical clarity was crucial. Many off-the-shelf embedding kits are available for embedding tissue. However, through tissue testing trials of many of these resins (Table 3.1), it was found that the fluorescence was not retained at an acceptable level, tissue morphology was affected, or the resin inherently affected the optical quality. Resins included in these trials were JB4, LR White, GMA with True Black, Spurr's, and EMbed-812. Further analysis of resins that were not included for trial can be found in the supplemental material (Table S3.1). In some cases, the resins (LR White and GMA) were changing the morphology of fluorescent polystyrene beads which questions the ability of the resin to preserve soft tissue morphology. Also, the resins would often quench the fluorescence of the sample (GMA, LR White, EMbed-812). Therefore, it was extremely difficult to pick a suitable embedding medium to fully support the capabilities of this system.

Resin Name	Type	Milling Quality	Preserve Fluores-cence	Preserve Morphol-ogy	Special Considerations	Papers
Epofix	Epoxy	Fair: Lots of large chips but clean sample surface.	Yes	Yes	Core biopsy sample.	[35,70, 71]
EMbed-812	Epoxy	Have not milled. Similar properties to SPURR.	No	TBD	None	[41,72]
LR White	Acrylic	Good: small chips and clean surface.	No	No	Needs complete absence of oxygen to	[31,34, 37,73–75]

					polymerize properly.	
JB-4	Acrylic	Good: small chips and clean surface.	Yes	No	None	[76]
SPURR	Epoxy	Good: small chips and clean surface.	N/A	N/A	None	[27]
GMA with True Black	Acrylic	Have not milled. Similar properties to JB-4.	No	N/A	Quenched and deformed beads.	[41]
Paraffin	Wax	Poor: Sample is ripped out of the wax.	N/A	N/A	Cannot withstand milling.	[77,78]

Table 3.1: Off-the-shelf resins were evaluated to determine the best media for the SETI system. Factors taken into consideration were the chemical basis of the resin, quality of the hardened media after milling, fluorescence preservation, and tissue morphology preservation. Through trial some resins presented difficulties or unique circumstances that necessitated special considerations. Each resin has corresponding literature that outlines previous applications and the formulations that were used for testing.

While the sample prep is not the focus of this work, to showcase the capabilities of this type of system, we embedded core biopsy shaped samples with EpoFix, then epoxy the embedded block onto a plastic cap (Electron Microscopy Sciences EBH-2 Block Holder: 70175-60). This fixes the resin and sample onto the plastic cap which is then secured onto the work table of the mill to start the imaging process. EpoFix was selected based on the observation that it strongly grips the edges of the sample to approximately 1 mm depth, but does not fully infiltrate it and thereby cause damage to the underlying cellular structure deeper in the sample. Thereby permitting the usage of a core biopsy style approach to mounting the sample.

Samples

We utilize three samples to show this technique, firstly a bead phantom made from Epofix with a mixture of 45μm and 90μm GFP beads. The imaging surface of this phantom was cut by the mill, then polished by hand to provide a clear scratch free surface to image through. For our main biological pathology sample we used GFP expressing mouse mammary tumors. This sample was cut by a pathologist into 3 mm diameter strips to approximate the shape of a core biopsy. These shaped samples were embedded in EpoFix. Only the center of the sample was imaged to avoid artifacts from the embedding media. Additionally we imaged GFP expressing Arabidopsis seedling roots directly embedded in EpoFix. Both the tumor and roots are compelling imaging problems where deeper fluorescence imaging is needed.

Hardware

The primary components of SETI include a CNC mill that is capable of three-axis movement (MicroMill DSLS 3000 from MicroProto Systems), an optical microscope with a CCD camera (Andor Clara), and a light projector (TI DLP4500 Evaluation Board) (Figure 3.1). The excitation lightpath is from the light projector, through a fixed blue excitation filter, then reflected by a green/blue dichroic, and focused by a Nikon Plan Apo 20x objective. The emission is then collected by the objective, passes through the dichroic then goes through a green emission filter mounted in a Thorlabs manual filter wheel, then focused on the CCD by an ASI C60 tube lens. The mill and the microscope are fixed in space, and the computer steered work table of the mill moves the sample to either the imaging or the machining position. The spindle for the milling cutter is set at 4300 rpm. The mill provides an advantage in the speed of cutting and the ability to handle larger samples that would be difficult to mount in more classical knife based approaches such as microtomes or vibratomes. The light projector shines patterned light perpendicularly into the microscope via a dichroic mirror, which reflects the incoming light onto the sample and passes the fluorescent light from the sample to the microscope. The mill is steered using “high” or “low” TTL signals coordinated via an Arduino Uno microcontroller. The Arduino, camera, and DLP are controlled by a BeanShell script in micro-manager.

Multiple DLPs were tested to find one that suited this system. We tried four DLPs: the PicoProjector from Texas Instruments, the LightCrafter 2000 from Texas Instruments, the IPD1865SL from iView Displays, and finally the DLP Evaluation Board 4500 from Texas Instruments. These four were mounted and tried in the system. The PicoProjector had the smallest form factor, but burned out during usage [21]. From this it was upgraded to the LightCrafter 2000. This DLP required some modification to be used in the system but was usable once it’s front optics had been removed. It also generated more lumens with a max around 100 lumens [22,23]. Unfortunately it was unable to completely fill the back aperture of the objective. This leads to the testing of the IPD1865SL DLP which was more than capable of filling out the objectives back aperture and produced a max of 1700 lumens with 1920x1080 resolution [24]. While the light engine and projection optics have a form factor that theoretically fits with the system, once the necessary heat sinks and controller boards were added, it was significantly too big for the system. Finally we tested the DLP 4500 Evaluation Board which is significantly smaller than the IPD1865SL, and has 1280x800 resolution and completely fills the back of the objective aperture [25]. It does require a wedge and custom mounting plate to compensate for its throw angle, but these can be readily 3D printed. Based on all these considerations, we decided to utilize the DLP 4500 Evaluation Board.

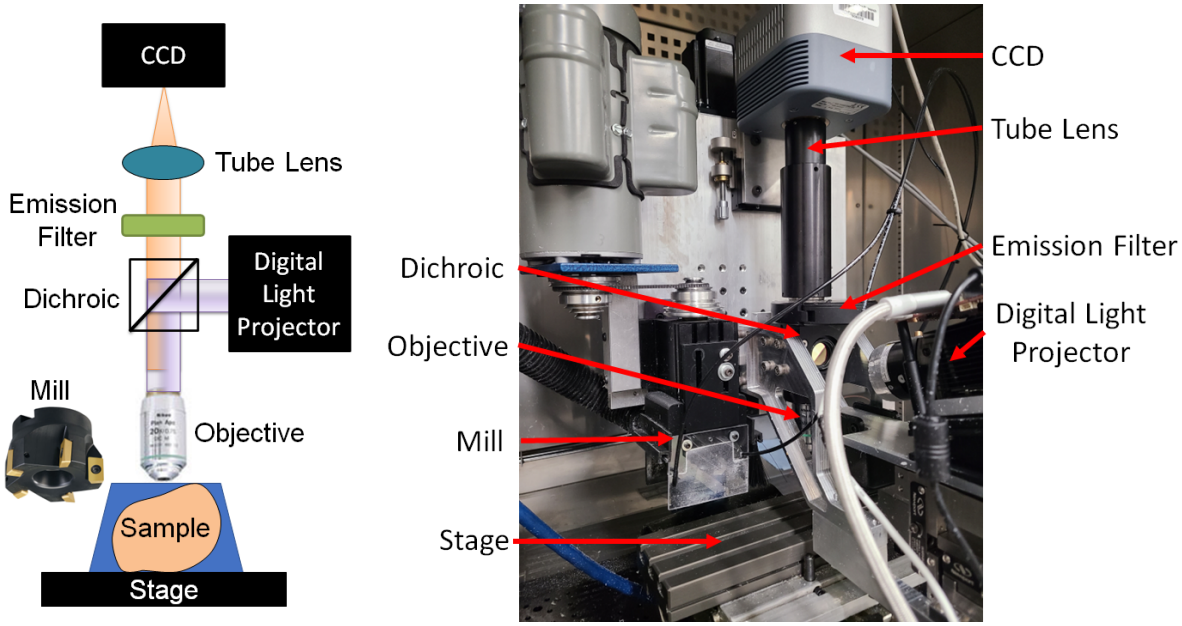

Fig. 3.1: (Left) An embedded sample is fluorescently imaged with patterns projected onto the top surface by a Texas Instruments DLP4500 Evaluation Module . Emitted light from the sample passes through the dichroic and is out of spectrum wavelengths are removed by an emission filter before being captured by an Andor Clara CCD camera. After the top surface is imaged the top layer is milled off with a MicroMill DSLS 3000 CNC and the newly exposed top surface is imaged. This is repeated for the full depth of the sample. (Right) Current layout of the system. The face mill head and the objective are coplanar to make the z-depth changes easier to handle.

Steering Software

The steering software is primarily implemented in the μManager 2.0 framework through a BeanShell script, a Java-based scripting language[18,19]. This works in conjunction with the CNC mill which is controlled by the Mach 3 software from Newfangled Solutions using G-Code, a CNC programming language. A G Code script moves the sample from under the microscope (imaging position) to under the milling cutter (milling position), makes the 10μm cut, and moves the sample back to the imaging position. This process is triggered by TTL signals from the Arduino and takes approximately 45 seconds. This time can be reduced by changing the milling speed, but comes at the cost of imaging surface quality. (Figure 3.2) When the milling is done, the BeanShell script loads a pre-generated sequence of patterns onto the projector to be shined onto the sample. The script switches the patterns and captures an image, then repeats the process for all patterns, all positions, and all cuts. Thereby giving us full system automation.

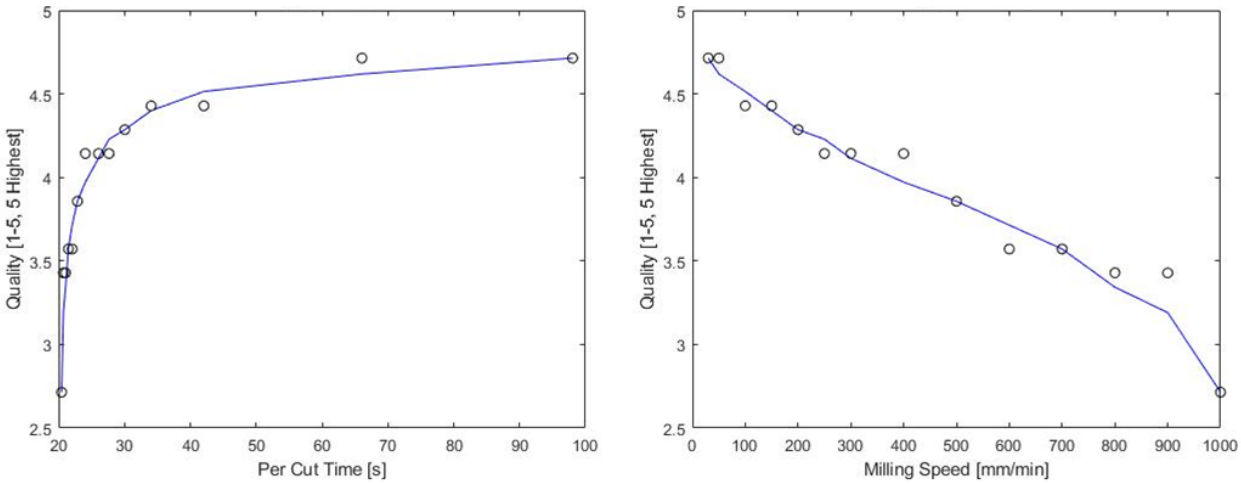

Fig. 3.2: Image quality was assessed by a trained observer of multiple representative sample images at each milling speed/per cut time. (Left) The total milling cut time was captured for multiple milling speeds. From this we can see an optimal balance point between cut time and image quality at about 30s per cut time, which corresponds to a milling speed of 200mm/min. (Right) As expected the milling speed is approximately inversely proportional to the image quality, meaning a faster cut produces a surface with a worse image quality.

Data Collection

Within the automated framework of the system, the operator selects the G Code to be used in Mach3, the projected pattern sequence, depth of imaging, and the name of the sample run in the BeanShell script. The script calculates the number of cycles needed and automatically alternates between the imaging and machining cycles until the input depth is reached. All images taken are automatically saved in a dedicated folder for reconstruction and analysis.

Reconstruction Software

Once the data set is collected in the automated framework, it needs to be run through the reconstruction algorithm (Figure 3.3). The reconstruction algorithm works with any image set that is supported in Bio-Formats[79]. The patterned images are self-normalized to compensate for flashing effects from the digital light projector and combined using the structured illumination axial sectioning algorithm[7,8]. The reconstructed images are combined into a three-dimensional cube using a monomodal optimizer with MATLAB's image registration function to get the translation transform between neighboring tiles. If the data set was acquired for calculating the rejection profile, each layer in the stack is summed and the intensity profile is plotted with a matched theoretical intensity falloff for each pattern used[7,8]. This software package is available in a Github repository.

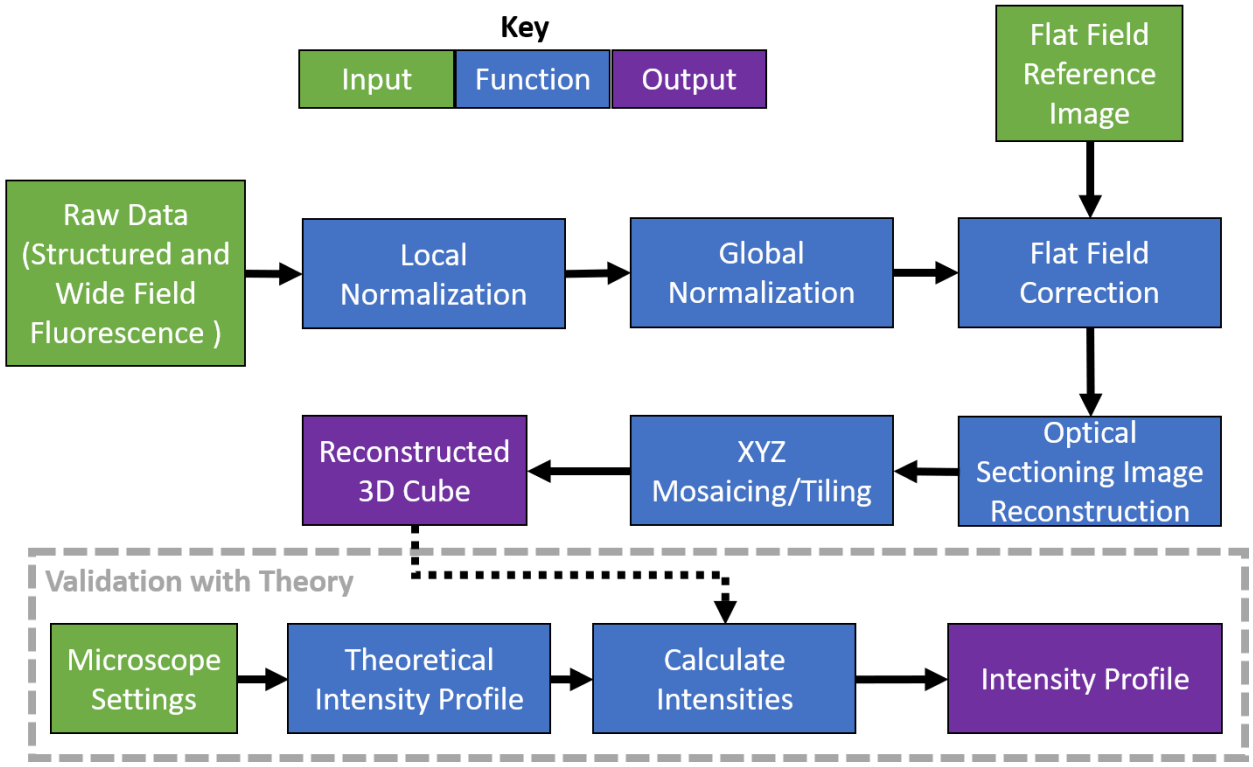

Fig. 3.3: The raw data as generated by the steering code is fed into the processing code which performs various preprocessing steps before using the computational optical axial sectioning algorithm to reconstruct images from the component images. The reconstructed images are then tiled and mosaiced to form the reconstructed 3D image cube. If the data was acquired using the rejection profiling mode, the reconstructed image cubes are used to generate intensity profiles which are matched to theory as calculated based on the microscope hardware configuration settings.

Results and Discussion

System Characterization and Artifact Analysis via Beads

Using a mixture of 45μm and 90μm GFP polystyrene beads embedded in a polished block of EpoFix, the system's characteristics were examined. (Figure 3.4) By comparing the field of view matched wide-field fluorescence images with the reconstructed images we can examine multiple characteristics and improvements of structured illumination systems and the ability to utilize a DLP. Specifically, when examining the point spread functions of the imaged bead a strong reduction in the out-of-focus intensity can be observed. Furthermore, by reducing the out-of-focus intensity, the three dimensional shape of the polystyrene beads is visible. The SETI process does lead to some artifacts. Samples which have whispering gallery effects can cause localized banding artifacts if the sample is on a hi/lo boundary of the pattern.

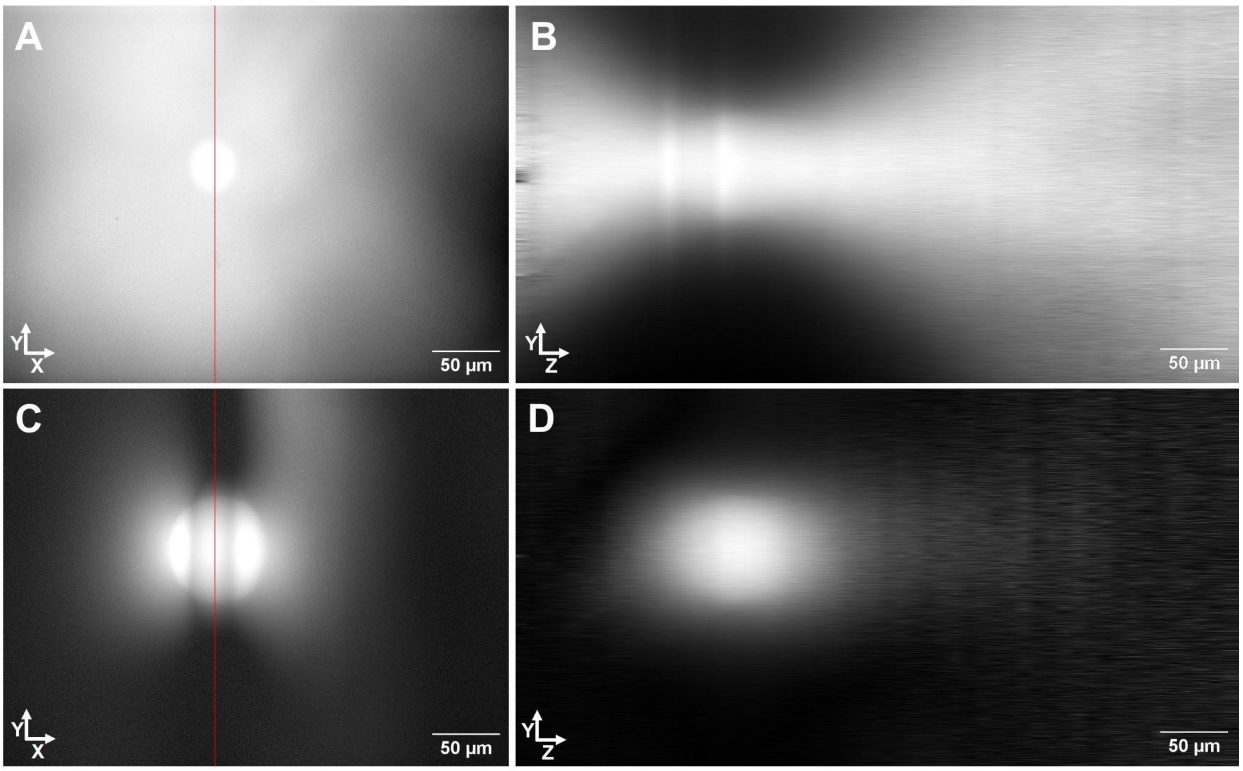

Fig. 3.4: (A) Max Intensity Stack projection of an en-face wide-field fluorescence image of a bead sample stack 530 µm deep. The bead is washed out by out-of-field fluorescence. (B) The sideview through the sample at the red line in A. The comet shaped point spread functions of the in-focus and out-of-focus layers of the bead are visible. (C) Matched view as A but using the optical sectioning algorithm to reject out-of-focus light. There is a banding/ringing artifact visible which occurs when a sample which has a whispering gallery effect is directly on the edge of one of the patterns. Furthermore, the banding is only along one axis due to the nature of the line pattern. (D) Matched view as C in the reconstructed image. The comet shaped point spread function of the bead is significantly reduced.

SETI Comparison to Multiphoton Microscopy with Biological Samples

A GFP expressing xenograft mouse mammary tumor (Figure 3.5) and GFP expressing Arabidopsis seedling roots (Figure 3.6) were imaged with both the SETI system and the most common deep optical microscopy technique of multiphoton microscopy. All images were acquired with a 20x 0.75NA air objective on both systems. One can see that while a basic sequential erosion system has worse lateral resolution than the multiphoton approach, it outperforms the multiphoton in how deep it can image without losing intensity.

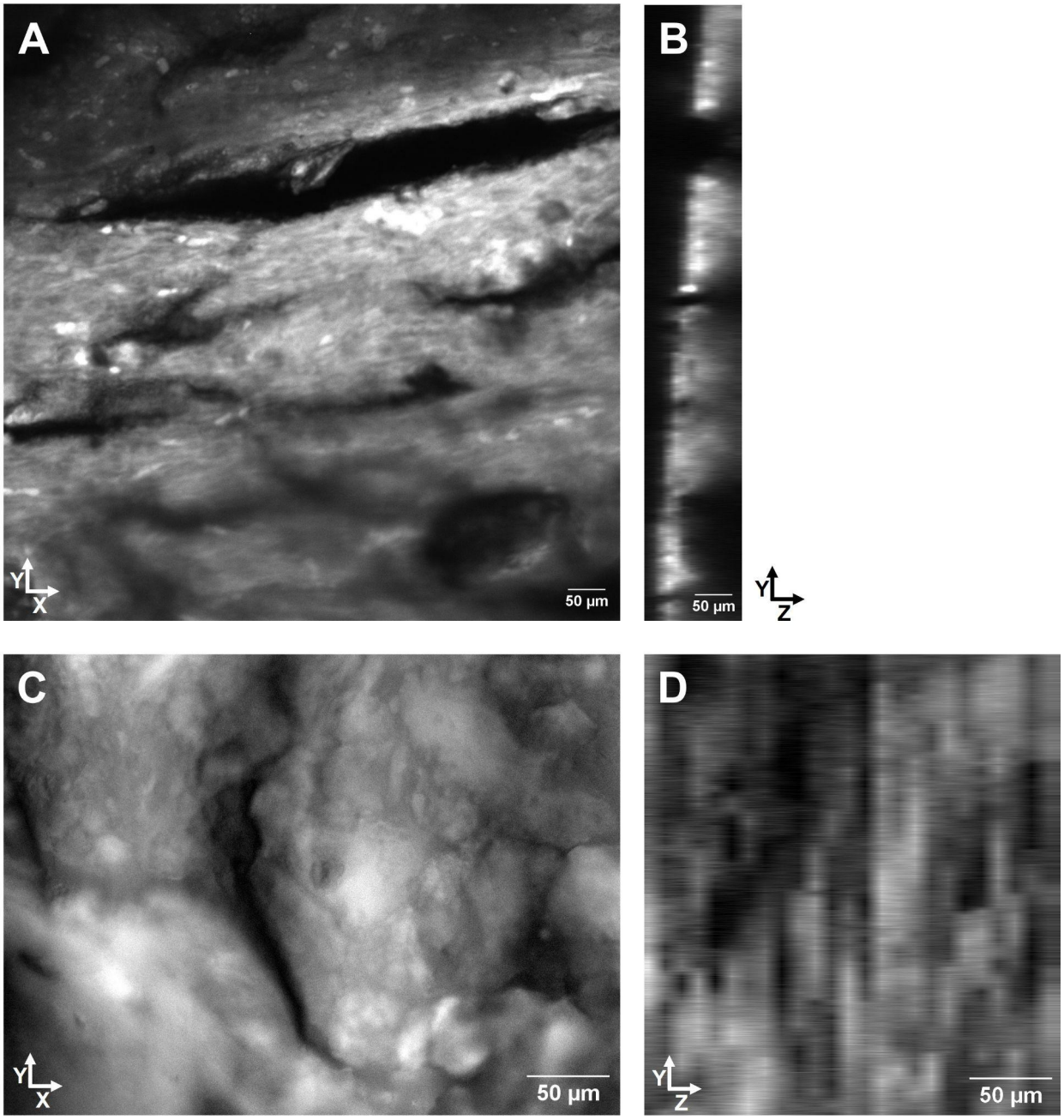

Fig. 3.5: Comparison of a GFP labeled xenograft mouse tumor sample imaged with the SETI system and multiphoton microscopy. (A) Multiphoton enface image (B) Multiphoton cross-section into Z (C) SETI enface image (D) SETI cross-section into Z showing we don't lose fluorescence with depth.

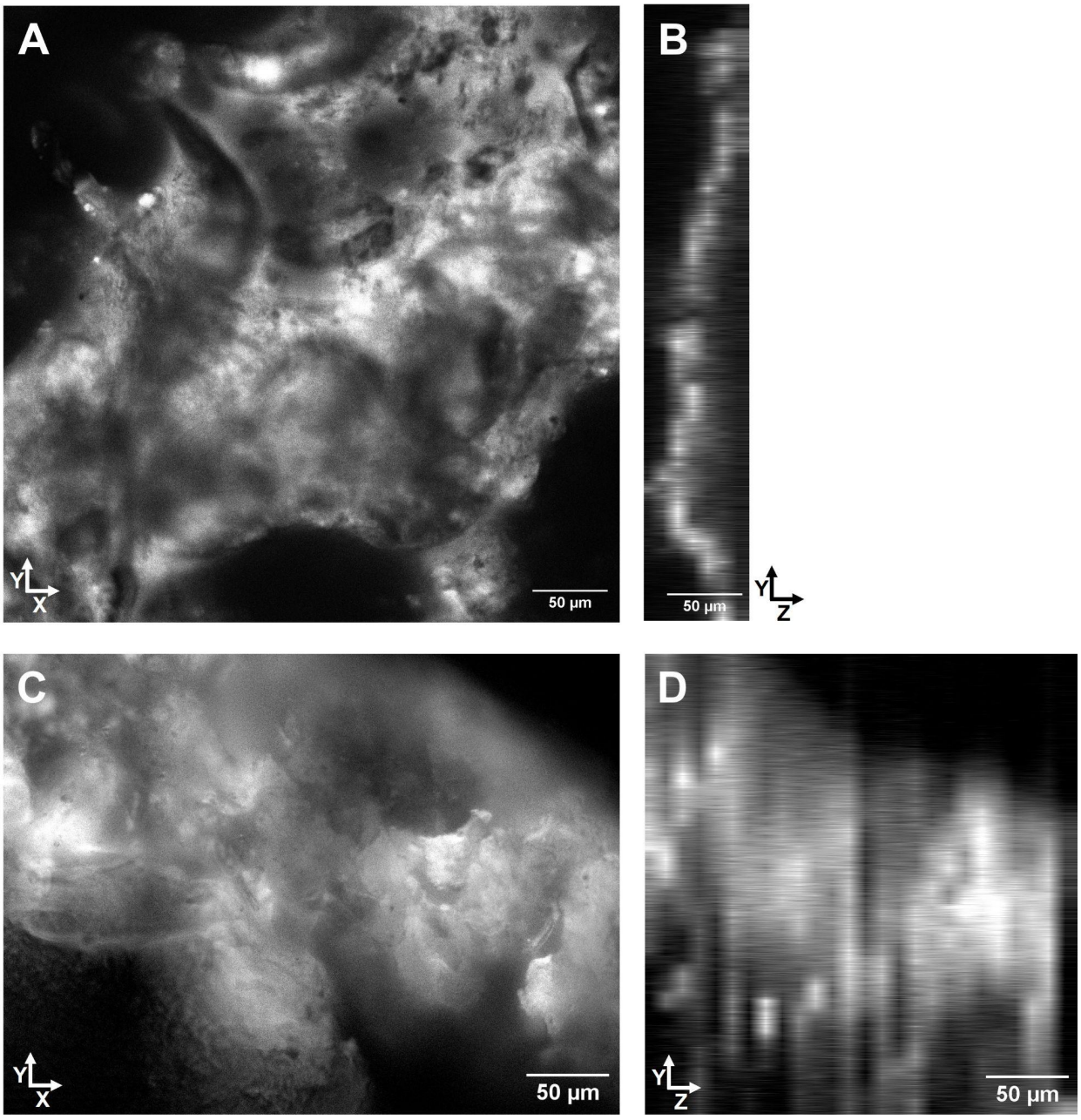

Fig. 3.6: Comparison of a GFP labeled Arabidopsis seedling roots sample imaged with the SETI system and multiphoton microscopy. (A) Multiphoton enface image (B) Multiphoton cross-section into Z (C) SETI enface image (D) SETI cross-section into Z showing we don't lose fluorescence with depth.

Future Directions

This prototype has shown the capabilities of a merged physical and optical sectioning system. Although the current system is cost-effective, there are several small modifications that could be made to increase the functionality and reliability of the system which could even better meet the needs of labs performing deep imaging with thick fluorescent samples. First, the motion on the z-axis could be further stabilized by reducing the movement of the system in z. One screw is currently responsible for moving the optical arm, mill, and DLP. This is an excessive amount of weight acting on a single support, sometimes resulting in chatter and slipping during imaging. A simple solution for improved z-axis motion could be achieved by translation of the sample, rather than the imaging and erosion systems. Additionally, there are a plethora of custom brackets and support pieces on the current model. Standardized and commercially available support structures could be utilized in a next-generation model to increase accessibility. With the milling approach, the embedded sample is destroyed because the milling process chips the material. This major drawback can be leveraged for secondary analysis by placing a collection trap in the vacuum hose used to clean the milled surface. This chipped material is ideal for proteomics which must chip and destroy the sample anyways[80]. Size reduction is another crucial step in making the system more accessible. As this project is developed further, the form factor can be reduced for a more compact setup. The proposed improvements to the system would aid in improving three main areas of user experience. Increasing organization with commercially available parts would create a system that is easier to build and iterate upon. Data collection would be more consistent with the reduction or elimination of mechanical slippage during imaging. More consistent data collection would also help any further computational development to improve the reconstruction algorithm. Even though there are improvements that could be made to the presented system, the achievements demonstrated are an important step towards realizing the ultimate goal of a novel, practical, and affordable technology for deep tissue imaging. Lastly, specimen preparation was a larger issue than initially anticipated because many commercially available resins did not work optimally for this system. Future possibilities include utilizing alternate niche resins which can improve the image quality by way of increased fluorescence preservation, decreasing cellular damage from the chemical processes, and a greater hardness that produces smaller chips with increased sample surface quality. An alternative to existing resins could be to formulate a new resin via a collaboration with an expert in chemistry. Also, if the hardware is retooled to work at -80C, the samples can be flashfrozen and directly mounted and milled, thereby capturing the metabolic state at the time of flash freezing. However, it should be understood that challenges arise with electronics when working at such cold temperatures and that frozen samples have not been machine milled, but have been typically sectioned by a microtome or via a focused ion beam[81–83]. This may be a result of cryosectioned samples not being as physically stable as plastic embedding resins and thus would mean the sample would not be able to withstand the mill[84]. Additionally, there is a strong possibility that the surface of the sample will be heated by the milling process and the sample will subsequently lose structural integrity.

Conclusion

We have presented a novel low-cost prototype which couples physical and optical sectioning for deep imaging into thick fluorescent samples with an open-source algorithm for rejecting background fluorescence in a single photon excitation setting. Using this prototype we have demonstrated its capacities on beads, GFP expressing tumors, and GFP expressing plant roots in direct comparison to multiphoton microscopy. This system can currently handle certain configurations of embedded thick fluorescent samples as presented, but future work could remove the configuration and potentially even the embedding constraint by improving the embedding resin or fully integrating cryo-capabilities. Additionally with the expandable open-source nature of this prototype, we provide a basis to be improved from for the further development of mill based sequential erosion tissue imaging systems.

Through this work, we generated a computational algorithm that can reconstruct background rejected images from two to six patterned sub-images. Therein encompassing the post-processing image reconstruction for most forms of structured illumination for background rejection [7,8]. While the underlying algorithm is in MATLAB, it has been functionalized such that all the methods can be accessed by ImageJ through the MATLAB-ImageJ bridge [20,85–88]. We further provide insight into the problems associated with combining physical and optical sectioning with a particular focus on the problems associated with milling and finding an appropriate embedding resin. This provides a basis for future work to incorporate the underlying open-source algorithms/scripts into fully open source frameworks and better physical setups with optimized embedding resins.

Chapter 3 References

1. Ragan T, Sylvan JD, Kim KH, Huang H, Bahlmann K, Lee RT, et al. High-resolution whole organ imaging using two-photon tissue cytometry. J Biomed Opt. 2007 Jan;12(1):014015.
2. Hildebrand DGC, Cicconet M, Torres RM, Choi W, Quan TM, Moon J, et al. Whole-brain serial-section electron microscopy in larval zebrafish. Nature. 2017 May;545(7654):345–9.
3. Micheva KD, Smith SJ. Array Tomography: A New Tool for Imaging the Molecular Architecture and Ultrastructure of Neural Circuits. Neuron. 2007 Jul 5;55(1):25–36.
4. Luo Y, Wang A, Liu M, Lei T, Zhang X, Gao Z, et al. Label-free brainwide visualization of senile plaque using cryo-micro-optical sectioning tomography. Opt Lett. 2017 Nov 1;42(21):4247–50.
5. Denk W, Horstmann H. Serial Block-Face Scanning Electron Microscopy to Reconstruct Three-Dimensional Tissue Nanostructure. PLOS Biol. 2004 Oct 19;2(11):e329.
6. Mertz J. Optical sectioning microscopy with planar or structured illumination. Nat Methods. 2011 Oct;8(10):811–9.
7. Karadaglić D, Wilson T. Image formation in structured illumination wide-field fluorescence microscopy. Micron. 2008 Oct 1;39(7):808–18.
8. Neil M a. A, Juškaitis R, Wilson T. Method of obtaining optical sectioning by using

structured light in a conventional microscope. Opt Lett. 1997 Dec 15;22(24):1905–7.
9. Maurer C, Jesacher A, Bernet S, Ritsch-Marte M. What spatial light modulators can do for optical microscopy. Laser Photonics Rev. 2011;5(1):81–101.
10. Savage N. Digital spatial light modulators. Nat Photonics. 2009 Mar;3(3):170–2.
11. Chang BJ, Chou LJ, Chang YC, Chiang SY. Isotropic image in structured illumination microscopy patterned with a spatial light modulator. Opt Express. 2009 Aug 17;17(17):14710–21.
12. Förster R, Lu-Walther HW, Jost A, Kielhorn M, Wicker K, Heintzmann R. Simple structured illumination microscope setup with high acquisition speed by using a spatial light modulator. Opt Express. 2014 Aug 25;22(17):20663–77.
13. Li R, Zhou X, Wu D, Peng T, Yang Y, Lei M, et al. Selective plane illumination microscopy with structured illumination based on spatial light modulators. In: Three-Dimensional and Multidimensional Microscopy: Image Acquisition and Processing XXI [Internet]. SPIE; 2014 [cited 2022 Oct 19]. p. 285–9. Available from: https://www.spiedigitallibrary.org/conference-proceedings-of-spie/8949/89491S/Selective-plane-illumination-microscopy-with-structured-illumination-based-on-spatial/10.1117/12.2040319.full
14. Mazhar A, Cuccia DJ, Gioux S, Durkin AJ, M.d JVF, Tromberg BJ. Structured illumination enhances resolution and contrast in thick tissue fluorescence imaging. J Biomed Opt. 2010 Jan;15(1):010506.
15. Saxena M, Eluru G, Gorthi SS. Structured illumination microscopy. Adv Opt Photonics. 2015 Jun 30;7(2):241–75.
16. Zhu J, Zhou P, Su X, You Z. Accurate and fast 3D surface measurement with temporal-spatial binary encoding structured illumination. Opt Express. 2016 Dec 12;24(25):28549–60.
17. Geng J. Structured-light 3D surface imaging: a tutorial. Adv Opt Photonics. 2011 Jun 30;3(2):128–60.
18. Edelstein AD, Tsuchida MA, Amodaj N, Pinkard H, Vale RD, Stuurman N. Advanced methods of microscope control using μManager software. J Biol Methods. 2014;1(2):e10.
19. Edelstein A, Amodaj N, Hoover K, Vale R, Stuurman N. Computer Control of Microscopes Using μManager. Curr Protoc Mol Biol. 2010;92(1):14.20.1-14.20.17.
20. MATLAB [Internet]. The Mathworks, Inc.; 2021. Available from: https://www.mathworks.com/products/matlab.html
21. DLP160AP data sheet, product information and support | TI.com [Internet]. [cited 2022 Nov 12]. Available from: https://www.ti.com/product/DLP160AP
22. DLPDLCR2000EVM Evaluation board | TI.com [Internet]. [cited 2022 Nov 12]. Available from: https://www.ti.com/tool/DLPDLCR2000EVM
23. DLP2000 data sheet, product information and support | TI.com [Internet]. [cited 2022 Nov 12]. Available from: https://www.ti.com/product/DLP2000
24. IPD1965SL [Internet]. [cited 2022 Nov 12]. Available from: https://www.iviewdisplays.com/pro_view-28.html
25. DLPLCR4500EVM Evaluation board | TI.com [Internet]. [cited 2022 Nov 12]. Available from: https://www.ti.com/tool/DLPLCR4500EVM
26. Sullivan-Brown J, Bisher ME, Burdine RD. Embedding, serial sectioning and staining of zebrafish embryos using JB-4 resin. Nat Protoc. 2011 Jan;6(1):46–55.
27. An YH, Moreira PL, Kang QK, Gruber HE. Principles of Embedding and Common Protocols. In: An YH, Martin KL, editors. Handbook of Histology Methods for Bone and Cartilage [Internet]. Totowa, NJ: Humana Press; 2003 [cited 2022 May 12]. p. 185–97. Available from: https://doi.org/10.1007/978-1-59259-417-7_11
28. Blaauw EH, Oosterbaan JA, Schakenraad JM. Improved Epon embedding for biomaterials. Biomaterials. 1989 Jul 1;10(5):356–8.

29. Burns WA, Bretschneider AM, Morrison AB. Embedding in large plastic blocks. Diagnostic light and potential electron microscopy on the same block. Arch Pathol Lab Med. 1979 Apr;103(4):177–9.
30. Carlemalm E, Garavito RM, Villiger W. Resin development for electron microscopy and an analysis of embedding at low temperature*. J Microsc. 1982;126(2):123–43.
31. de Mesy Jensen KL, di Sant'Agnese PA. Large block embedding and "pop-off" technique for immunoelectron microscopy. Ultrastruct Pathol. 1992 Apr;16(1–2):51–9.
32. Fischer AH, Jacobson KA, Rose J, Zeller R. Paraffin Embedding Tissue Samples for Sectioning. Cold Spring Harb Protoc. 2008 May 1;2008(5):pdb.prot4989.
33. Fischer AH, Jacobson KA, Rose J, Zeller R. Cutting Sections of Paraffin-Embedded Tissues. Cold Spring Harb Protoc. 2008 May 1;2008(5):pdb.prot4987.
34. Gros O, Maurin LC. Easy flat embedding of oriented samples in hydrophilic resin (LR White) under controlled atmosphere: Application allowing both nucleic acid hybridizations (CARD-FISH) and ultrastructural observations. Acta Histochem. 2008 Sep 8;110(5):427–31.
35. Li C, Risnes S. A comparison of resins for embedding teeth, with special emphasis on adaptation to enamel surface as evaluated by scanning electron microscopy. Arch Oral Biol. 2004 Jan 1;49(1):77–83.
36. Luft JH. IMPROVEMENTS IN EPOXY RESIN EMBEDDING METHODS. J Biophys Biochem Cytol. 1961 Feb 1;9(2):409–14.
37. Luo T, Deng L, Li A, Zhou C, Shao S, Sun Q, et al. Scalable Resin Embedding Method for Large-Volume Brain Tissues with High Fluorescence Preservation Capacity. iScience [Internet]. 2020 Nov 20 [cited 2022 May 12];23(11). Available from: https://www.cell.com/iscience/abstract/S2589-0042(20)30914-7
38. Mandry P, Murray AB, Rieke L, Becke H, Höfler H. Postembedding Ultrastructural in Situ Hybridization on Ultrathin Cryosections and LR White Resin Sections. Ultrastruct Pathol. 1993 Jan 1;17(2):185–94.
39. McDonald KL. Rapid Embedding Methods into Epoxy and LR White Resins for Morphological and Immunological Analysis of Cryofixed Biological Specimens. Microsc Microanal. 2014 Feb;20(1):152–63.
40. Ren M, Tian J, Sun Q, Chen S, Luo T, Jia X, et al. Plastic embedding for precise imaging of large-scale biological tissues labeled with multiple fluorescent dyes and proteins. Biomed Opt Express. 2021 Oct 6;12(11):6730–45.
41. Ren M, Tian J, Sun Q, Chen S, Luo T, Jia X, et al. Plastic embedding for precise imaging of large-scale biological tissues labeled with multiple fluorescent dyes and proteins. Biomed Opt Express. 2021 Oct 6;12(11):6730–45.
42. Wallis MA, Griffin RL. A routine method for embedding animal tissues in Spurr resin for electron microscopy. J Clin Pathol. 1973 Jan 1;26(1):77–8.
43. Miyawaki A, Niino Y. Molecular Spies for Bioimaging—Fluorescent Protein-Based Probes. Mol Cell. 2015 May 21;58(4):632–43.
44. Zhang J, Campbell RE, Ting AY, Tsien RY. Creating new fluorescent probes for cell biology. Nat Rev Mol Cell Biol. 2002 Dec;3(12):906–18.
45. Helmchen F, Denk W. Deep tissue two-photon microscopy. Nat Methods. 2005 Dec;2(12):932–40.
46. Denk W, Strickler JH, Webb WW. Two-Photon Laser Scanning Fluorescence Microscopy. Science [Internet]. 1990 Apr 6 [cited 2021 Sep 3]; Available from: https://www.science.org/doi/abs/10.1126/science.2321027
47. Briggman KL, Denk W. Towards neural circuit reconstruction with volume electron microscopy techniques. Curr Opin Neurobiol. 2006 Oct 1;16(5):562–70.
48. Conklin MW, Provenzano PP, Eliceiri KW, Sullivan R, Keely PJ. Fluorescence Lifetime Imaging of Endogenous Fluorophores in Histopathology Sections Reveals Differences

Between Normal and Tumor Epithelium in Carcinoma In Situ of the Breast. Cell Biochem Biophys. 2009 Apr 1;53(3):145–57.
49. Barocas DA, Mathew S, DelPizzo JJ, Vaughan Jr ED, Sosa RE, Fine RG, et al. Renal cell carcinoma sub-typing by histopathology and fluorescence in situ hybridization on a needle-biopsy specimen. BJU Int. 2007;99(2):290–5.
50. Layfield LJ, Meloni-Ehrig A, Liu K, Shepard R, Harrelson JM. Malignant Giant Cell Tumor of Synovium (Malignant Pigmented Villonodular Synovitis): A Histopathologic and Fluorescence In Situ Hybridization Analysis of 2 Cases With Review of the Literature. Arch Pathol Lab Med. 2000 Nov 1;124(11):1636–41.
51. Kleinfeld D, Bharioke A, Blinder P, Bock DD, Briggman KL, Chklovskii DB, et al. Large-Scale Automated Histology in the Pursuit of Connectomes. J Neurosci. 2011 Nov 9;31(45):16125–38.
52. Conchello JA, Lichtman JW. Optical sectioning microscopy. Nat Methods. 2005 Dec;2(12):920–31.
53. Amos WB, White JG. How the Confocal Laser Scanning Microscope entered Biological Research. Biol Cell. 2003;95(6):335–42.
54. Amos WB, White JG, Fordham M. Use of confocal imaging in the study of biological structures. Appl Opt. 1987 Aug 15;26(16):3239–43.
55. Wright SJ, Centonze VE, Stricker SA, DeVries PJ, Paddock SW, Schatten G. Chapter 1 Introduction to Confocal Microscopy and Three-Dimensional Reconstruction. In: Matsumoto B, editor. Methods in Cell Biology [Internet]. Academic Press; 1993 [cited 2022 Nov 6]. p. 1–45. (Cell Biologcal Applications of Confocal Microscopy; vol. 38). Available from: https://www.sciencedirect.com/science/article/pii/S0091679X0860998X
56. Bushby AJ, P'ng KMY, Young RD, Pinali C, Knupp C, Quantock AJ. Imaging three-dimensional tissue architectures by focused ion beam scanning electron microscopy. Nat Protoc. 2011 Jun;6(6):845–58.
57. Heymann JAW, Shi D, Kim S, Bliss D, Milne JLS, Subramaniam S. 3D Imaging of mammalian cells with ion-abrasion scanning electron microscopy. J Struct Biol. 2009 Apr;166(1):1–7.
58. Knott G, Marchman H, Wall D, Lich B. Serial Section Scanning Electron Microscopy of Adult Brain Tissue Using Focused Ion Beam Milling. J Neurosci. 2008 Mar 19;28(12):2959–64.
59. WANNER AA, KIRSCHMANN MA, GENOUD C. Challenges of microtome‐based serial block‐face scanning electron microscopy in neuroscience. J Microsc. 2015 Aug;259(2):137–42.
60. Saitta B, Jalili MF, Zohoorkari H, Rao R, Hallows KR, Baty CJ, et al. Chapter 10 - Ex vivo kidney slice preparations as a model system to study signaling cascades in kidney epithelial cells. In: Weimbs T, editor. Methods in Cell Biology [Internet]. Academic Press; 2019 [cited 2022 Jun 1]. p. 185–203. (Methods in Kidney Cell Biology - Part A; vol. 153). Available from: https://www.sciencedirect.com/science/article/pii/S0091679X19300688
61. Sousa AL, Rodrigues Lóios J, Faísca P, Tranfield EM. Chapter 2 - The Histo-CLEM Workflow for tissues of model organisms. In: Müller-Reichert T, Verkade P, editors. Methods in Cell Biology [Internet]. Academic Press; 2021 [cited 2022 Jun 1]. p. 13–37. (Correlative Light and Electron Microscopy IV; vol. 162). Available from: https://www.sciencedirect.com/science/article/pii/S0091679X20302077
62. Chen X, Chen X, Zhang X, Zhang X, Zhong Q, Zhong Q, et al. Dual-mode Micro-Optical Sectioning Tomography for simultaneously acquiring Golgi-stained neuronal morphology with co-located cytoarchitecture in the same brain. In: International Conference on Photonics and Imaging in Biology and Medicine (2017), paper W3A32 [Internet]. Optical Society of America; 2017 [cited 2021 Sep 3]. p. W3A.32. Available from: https://www.osapublishing.org/abstract.cfm?uri=PIBM-2017-W3A.32

63. Stowell RE. Effect on Tissue Volume of Various Methods of Fixation, Dehydration, and Embedding. Stain Technol. 1941 Jan;16(2):67–83.
64. Nielsen KK*, Andersen CB, Kromann-Andersen B. A Comparison Between the Effects of Paraffin and Plastic Embedding of the Normal and Obstructed Minipig Detrusor Muscle Using the Optical Dissector. J Urol. 1995 Dec 1;154(6):2170–3.
65. Yang Z, Hu B, Zhang Y, Luo Q, Gong H. Development of a Plastic Embedding Method for Large-Volume and Fluorescent-Protein-Expressing Tissues. PLOS ONE. 2013 Apr 5;8(4):e60877.
66. Sullivan-Brown J, Bisher ME, Burdine RD. Embedding, Serial Sectioning and Staining of Zebrafish Embryos Using JB-4™ Resin. Nat Protoc. 2011 Jan;6(1):46–55.
67. Russell SD, Daghlian CP. Scanning electron microscopic observations on deembedded biological tissue sections: Comparison of different fixatives and embedding materials. J Electron Microsc Tech. 1985;2(5):489–95.
68. Zhou H, Gang Y, Chen S, Wang Y, Xiong Y, Li L, et al. Development of a neutral embedding resin for optical imaging of fluorescently labeled biological tissue. J Biomed Opt. 2017 Oct;22(10):106015.
69. Zhou H, Liu X, Gang Y, Lv X, Zeng S. A novel reactive resin for embedding biological tissue. In: Neural Imaging and Sensing [Internet]. SPIE; 2017 [cited 2022 Jan 24]. p. 36–8. Available from: https://www.spiedigitallibrary.org/conference-proceedings-of-spie/10051/100510H/A-novel-reactive-resin-for-embedding-biological-tissue/10.1117/12.2251267.full
70. Nielsen JK, Maiboe J. EPOFIX AND VACUUM: AN EASY METHOD TO MAKE CASTS OF HARD SUBSTRATES. Palaeontol Assoc. 2000;3(1):10.
71. Carter JG, Ambrose WW. Techniques for studying molluscan shell microstructure. Paleontol Soc Spec Publ. 1989 ed;4:101–19.
72. Sousa AL, Rodrigues Lóios J, Faísca P, Tranfield EM. Chapter 2 - The Histo-CLEM Workflow for tissues of model organisms. In: Müller-Reichert T, Verkade P, editors. Methods in Cell Biology [Internet]. Academic Press; 2021 [cited 2022 Oct 12]. p. 13–37. (Correlative Light and Electron Microscopy IV; vol. 162). Available from: https://www.sciencedirect.com/science/article/pii/S0091679X20302077
73. Skepper JN, Powell JM. Immunogold Staining of London Resin (LR) White Sections for Transmission Electron Microscopy (TEM). Cold Spring Harb Protoc. 2008 Jun 1;2008(6):pdb.prot5016.
74. Yang Z, Hu B, Zhang Y, Luo Q, Gong H. Development of a Plastic Embedding Method for Large-Volume and Fluorescent-Protein-Expressing Tissues. PLOS ONE. 2013 Apr 5;8(4):e60877.
75. Zhou H, Gang Y, Chen S, Wang Y, Xiong Y, Li L, et al. Development of a neutral embedding resin for optical imaging of fluorescently labeled biological tissue. J Biomed Opt. 2017 Oct;22(10):106015.
76. Sullivan-Brown J, Bisher ME, Burdine RD. Embedding, Serial Sectioning and Staining of Zebrafish Embryos Using JB-4™ Resin. Nat Protoc. 2011 Jan;6(1):46–55.
77. Nielsen KK*, Andersen CB, Kromann-Andersen B. A Comparison Between the Effects of Paraffin and Plastic Embedding of the Normal and Obstructed Minipig Detrusor Muscle Using the Optical Dissector. J Urol. 1995 Dec 1;154(6):2170–3.
78. Stowell RE. Effect on Tissue Volume of Various Methods of Fixation, Dehydration, and Embedding. Stain Technol. 1941 Jan 1;16(2):67–83.
79. Linkert M, Rueden CT, Allan C, Burel JM, Moore W, Patterson A, et al. Metadata matters: access to image data in the real world. J Cell Biol. 2010 May 31;189(5):777–82.
80. Görg A, Weiss W, Dunn MJ. Current two-dimensional electrophoresis technology for proteomics. PROTEOMICS. 2004;4(12):3665–85.
81. Roy D, Steyer GJ, Gargesha M, Stone ME, Wilson DL. 3D Cryo-Imaging: A Very

High-Resolution View of the Whole Mouse. Anat Rec Hoboken NJ 2007. 2009 Mar;292(3):342–51.
82. Lam V, Villa E. Practical approaches for cryo-FIB milling and applications for cellular cryo-electron tomography. Methods Mol Biol Clifton NJ. 2021;2215:49–82.
83. Zachs T, Schertel A, Medeiros J, Weiss GL, Hugener J, Matos J, et al. Fully automated, sequential focused ion beam milling for cryo-electron tomography. Carter AP, Kuriyan J, editors. eLife. 2020 Mar 9;9:e52286.
84. Fischer AH, Jacobson KA, Rose J, Zeller R. Cryosectioning Tissues. Cold Spring Harb Protoc. 2008 Aug 1;2008(8):pdb.prot4991.
85. Schroeder AB, Dobson ETA, Rueden CT, Tomancak P, Jug F, Eliceiri KW. The ImageJ ecosystem: Open-source software for image visualization, processing, and analysis. Protein Sci. 2021;30(1):234–49.
86. Schindelin J, Rueden CT, Hiner MC, Eliceiri KW. The ImageJ ecosystem: An open platform for biomedical image analysis. Mol Reprod Dev. 2015;82(7–8):518–29.
87. Rueden CT, Schindelin J, Hiner MC, DeZonia BE, Walter AE, Arena ET, et al. ImageJ2: ImageJ for the next generation of scientific image data. BMC Bioinformatics. 2017 Nov 29;18(1):529.
88. Hiner MC, Rueden CT, Eliceiri KW. ImageJ-MATLAB: a bidirectional framework for scientific image analysis interoperability. Bioinformatics. 2017 Feb 15;33(4):629–30.

Chapter 4: Real-Time Fluorescence Lifetime Imaging Microscopy Estimation (RT-FLIM)

So far the primary focus of this thesis has been on developing new post-acquisition processing tools, but computational microscopy can also provide benefits at run-time [1,2]. Ths run-time analysis often called smart microscopy means analysis can occur while the sample is still on the microscope with the results of the analysis being used to guide the acquisition [3–5]. One application of run-time analysis is to improve the process of capturing FLIM data [6]. With FLIM being a common research tool, it does bear a significant drawback in terms of the ability to verify that collected data is usable as one collects it [7,8]. In the current FILM acquisition which is time and resource consuming, one does not usually know if the FLIM data is robustly and accurately collected until after the experiment is over. As such, fast computational methods for FILM estimation of quality and accuracy implemented in an open source platform for FLIM can enable getting an estimate of the data quality at run-time.

FLIM is still largely a separate experiment in fluorescence imaging and traditionally viewed as a separate dataset to be analyzed independent of the intensity-based fluorescence data [9]. This is in part due to the different methods and hardware available on the market [7,10]. However, for many modern imaging systems such as laser scanning systems both commercial and home-built, the FLIM element has been integrated into the acquisition so it can be collected with one common software package and interface. Despite this improved integration, the FLIM data is treated very differently from the fluorescence intensity data. Fluorescence intensity data is viewed in real-time while it is collected and is analyzed carefully for not only its quantitative metrics but also for key morphology features. FLIM due to its analysis needs is typically collected blindly and not analyzed until post-acquisition [7]. Meaning the user has no idea whether their collection captured useful and accurate differences in lifetimes until hours later. Additionally, FLIM data is typically not treated like an image and FLIM measurements are typically not combined with important image metrics as biological morphology. We propose a computational platform that can directly address both these needs.

This platform will effectively act as a FLIM quality viewfinder. Wherein, a view finder is ideally a real time image available to users which gives an estimation of the region and metrics that will be captured in an image in the current imaging configuration. Since most time domain based FLIM methods are focused on single photon counting (SPC), the critical parameters to optimize for in a FLIM viewfinder are fast processing and informative rough lifetime estimation from very low photon counts [7]. As such, to find an appropriate real time methodology which can act as a lifetime viewfinder, I compared four algorithms as shown in Table 4.1. Noise Corrected - Primary Component Analysis (NC-PCA), is of interest since it corrects for the Poisson distribution of noise in the image and Primary Component Analysis is a computationally fast analysis that can quickly provide an estimated relative lifetime score (i.e. not the actual lifetime, but an estimate of the pixel lifetime variance from mean for the image) [11]. Additionally, Phasor Analysis is of

interest since it comes from frequency domain FLIM and acts globally on all pixels in an image to estimate the phase and modulation of a single from time-domain data and can separate lifetime distributions by projecting them into a two dimensional space. This two dimensional projection can then be further used to give a lifetime score to each pixel for fast grouping of clusters and with slower computation be used to calculate the actual lifetimes present in individual pixels [12]. Laguerre deconvolution based approaches function similarly to a phasor approach, but rather than projecting into the frequency domain, they project into Laguerre space. From which a scoring of the lifetimes of pixels in the image can be generated for fast estimation [13]. Furthermore, Rapid Lifetime Determination (RLD) provides a general description of the lifetime decay process and can come in multi-component variants [14]. It provides a significantly faster calculation methodology than a least squares fitting approach and has been shown to provide a fairly accurate calculation of lifetime under most conditions [14]. Unfortunately, currently utilizing these algorithms requires a significant coding background to implement on any system. Therefore I selected one algorithm based on comparative benchmarking on representative FLIM data sets to determine an optimal viewfinder algorithm for implementation in OpenScan [15].

Levenberg-Marquardt Fitting [7,16]	Gold standard analysis method
Noise Corrected Primary Component Analysis [11]	Robust determination of an unknown number of fluorescent lifetime species at low photon counts.
Phasor Analysis [12,17]	Additional information through the phasor plot
Laguerre Deconvolution [9,13,18]	Potential to be very fast
Rapid Lifetime Determination [14,19,20]	Computational simplicity for speed

Table 4.1 Methodology Overview. Tested algorithms (left) were each selected for their specializations. (right)

Levenberg-Marquardt Fitting (LM)

Levenberg-Marquardt fitting is the gold-standard analysis method for time and frequency domain based FLIM [21–24]. LM is a non-linear least squares fitting routine that combines gradient descent and Gauss-Newton fitting algorithms [25]. This fitting method iteratively improves the fit parameters of a given function till it either converges or reaches its maximum allowed number of iterations. In FLIM it is used to fit an exponential decay or multiple exponential decays to the counts collected at each pixel with the fluorescence lifetime as a parameter [8,26]. While this process does generate what is considered to be the best fit of FLIM data possible, it does have the significant drawback that it takes a long time and in most applications requires the whole data set to have been collected before analysis [6,7,27]. All

estimates from the other methods were compared to the respective fully Levenberg-Marquardt fitted data set to generate an accuracy metric in relation to accepted ground-truth.

Noise Corrected Primary Component Analysis (NC-PCA)

Noise Corrected Primary Component Analysis is designed to operate on a sample with an unknown number of fluorescent lifetime species at low photon counts. This makes it very good at separating out distinct micro-environments in an image [11]. Paired with the low photon counts needed for it, makes it of significant interest to our application since it can potentially give an estimate and even detect possible problems with the data. At its core NC-PCA is just Poisson noise-correction paired with standard primary component analysis. The noise correction is done by dividing the image by the square-root of the measured average intensity at each time bin. Then this corrected data goes through single value decomposition of the image's covariance matrix. The eigenvectors of the resultant primary components are used to score each pixel. This score can be directly used as a relative estimate that shows distinct microenvironments. This method is relatively robust for determining the number of microenvironments present in a field of view and is capable of handling and highlighting abnormalities in the data set; single value decomposition can be quite slow. Additionally this method only provides a relative estimate through the scored primary component images, it has no direct ability to produce a quantitative lifetime value.

Phasor Analysis

Phasor Analysis of FLIM data was developed on frequency domain systems and generates additional information which can be used to separate species and can display underlying problems with the data [17]. While phasor analysis may be based in the frequency domain, it can also be used in time domain single-photon counting systems. To do so one has to take the fourier transform of the signal. The real and imaginary components from the transform are then used as a coordinate system and plotted for each pixel to generate a phasor plot [12]. To recover the actual lifetimes from a phasor plot requires fitting [28]. That said the components can directly be used to generate a relative estimate score, thereby forgoing the fitting [29]. Overall the additional information gained from the phasor plot can be very beneficial and is robust to having an unknown number of fluorescent lifetime species in the sample which can be determined through the phasor plot [30]. But to avoid fitting which tends to be slow, we have to settle for a relative estimated scored image with no direct quantitative lifetime value.

Laguerre Deconvolution

Similar to Phasor Analysis, Laguerre Deconvolution is focused on projecting the pixel lifetimes into a secondary space. Instead of using the Fourier transform to project each pixel sequentially into phasor space, it uses a Laguerre expansion method to project all the pixels simultaneously into Laguerre space. Due to this simultaneous projection, Laguerre deconvolution has the potential to be very fast [13,31]. The Laguerre bases that are calculated through this expansion can be used to generate a relative estimated scored image [18]. While this has the potential to be very fast due to its nature, it has been shown to provide low accuracy of information [9,32].

Rapid Lifetime Determination (RLD)

Rapid Lifetime Determination is the computationally simplest method of the tested set. Which inherently implies that it is the fastest method. RLD is a method to quickly estimate the lifetime of single or bi-exponential decay curves from any source [14,19]. For FLIM it is run on every individual pixel, and first calculates the width of the fluorescence response. Then it estimates the lifetime and amplitude by splitting the response window in half and summing all the counts in each half. While this method is incredibly fast and does directly produce a lifetime for each pixel, it does require a priori knowledge of how many distinct fluorescent lifetime species are in the sample. Additionally it can be susceptible to artifacts arising from the imaging process [20].

To determine which algorithm is optimal for integration into OpenScan to give a look at the live data stream from FLIM, we must select an algorithm that is faster than the data acquisition rate. Particularly since the scan rate is typically one frame per second, but each frame only captures one excitation pulse, so multiple frames (30-60) need to be acquired to have enough data to generate a single image [7]. Meaning that even if in a low resolution imaging sequence the acquisition rate is one fully collected frame per twenty seconds. Which is a refresh rate of 0.05 Hz. Since hardware is constantly improving, eventually the data acquisition rate will be faster than video rate, so for the sake of longevity and usefulness of the tool, the live video rate of 60Hz will be used as our optimal speed threshold. Meaning whichever algorithm is selected needs to operate on average under 16.7ms (optimally) or 20s (at worst) from taking data from the data stream, generating an estimate on the cumulative image, and then updating the display with the new estimate [33]. Then selection between any algorithms that fall below this threshold, is determined by whichever, on average, has the highest accuracy.

Based on our testing RLD was the fastest and was capable of producing accurate results most of the time. Similarly phasor analysis was fast enough and was able to visually quantify information about lifetime clusters while producing accurate results. NC-PCA and Laguerre deconvolution were both too slow to be considered further. As such with the extra information it added we decided to primarily implement the phasor analysis approach for the RT-FLIM estimation in OpenScan. Additionally since the RLD is very straightforward from a coding standpoint, it was added as an optional additional view in OpenScan. This allows users to use whichever method they are most comfortable with between the two and makes this tool more well-rounded and appealing to more research groups.

We have presented the new capabilities of OpenScan and how it can assist researchers who use FLIM. Specifically by adding an early warning system/data quality check through real-time FLIM estimation of not only phasor analysis but also RLD. Of particular interest is that this has added methods to OpenScan to access the direct datastream coming from a FLIM system. While we only use it as an early warning system so far, this has significant potential for future methods that can utilize this datastream. We additionally showed the computational power comparisons of the methods that were considered. As more and better estimation methods get developed for FLIM other methods that can either access more information about the image in real time or can provide even better estimations, can be added as optional additional views in OpenScan.

With this tool readily available in OpenScan, we have added quality control measures earlier into the imaging pipeline for FLIM [15]. This further shows the reasoning behind which algorithms were selected for implementation and provides a head-to-head comparison of the estimation methods tested. As accessible run-time computational power increases and estimation algorithms are refined, more and better FLIM estimation methods will reach the necessary criterion to operate at run-time approaching live-view FLIM, not just as a data quality control, but as a fully operational imaging mode.

Adapted from “Real-Time Open-Source FLIM Analysis” Tan, Kevin K. D., Gahm, Niklas A., Tsuchida, Mark A., Chacko, Jenu V., Eliceiri, Kevin W. Frontiers (will be submitted to Frontiers within the next week)

Abstract

Fluorescence lifetime imaging microscopy (FLIM) provides quantitative information on the chemical microenvironment of the fluorophore. Analysis of data from the widely used time-correlated single photon counting (TCSPC) implementation of FLIM is usually a post-acquisition operation due to lengthy computation times and the lack of real-time analysis toolkits that are open source and accessible. Typically, the quality of FLIM data is uncertain until after collection, and it is frequently accounted for by extending the duration of the imaging session. However, such lengthy FLIM collection sessions can not only cause important biological events to be missed but also result in unwanted photobleaching and photodamage to the samples. FLIM data collection would therefore benefit from tools to assess during imaging when and if sufficient data has been collected to accurately identify the underlying FLIM signature of a molecule and make relevant conclusions. We present the first open-source program that enables FLIM analysis while the specimen is still being scanned by combining acquisition with real-time computational and visualization capabilities. Our open-source real-time FLIM viewer is a Napari plugin that displays phasor analysis and rapid lifetime determination (RLD) results computed from data sent on the fly from acquisition software, such as the open-source Micro-Manager based OpenScan package. By providing preliminary analysis during acquisition, our method allows early identification of FLIM signatures and assessment of data quality, speeding the imaging process for sensitive live biological samples.

Keywords

Fluorescence Lifetime, FLIM, Real-time FLIM Analysis, Open Source, Phasor, Napari, Live FLIM

Introduction

Fluorescence Lifetime Imaging Microscopy (FLIM) maps the spatial distribution of excited state lifetimes over a field of view, generating contrast that is in addition to the fluorophore (intensity) distribution. Fluorescence lifetime measures the inverse of the rate of decay of fluorescence after excitation [9,16]. The measurement of fluorescence lifetime can provide a unique sensitivity to measurements of variations in the microenvironment of fluorophores and the physical structure of the molecule [9,31,34]. For example, FLIM is used to monitor the free and enzyme-bound fluorescence lifetime of reduced nicotinamide adenine dinucleotide in live cells and correlate the ratio to the metabolic state of the cells [9,35,36]. FLIM measurements can be performed in the time domain or frequency domain. A principal method of time-domain FLIM employs time-correlated single photon counting (TCSPC) to measure per-pixel photon histograms binned by time delay relative to pulsed excitation.

From such photon histograms, fitting to an exponential or multi-exponential decay function is a common method for determining fluorescence lifetime. More specifically, nonlinear least-squares fitting via the Levenberg–Marquardt algorithm (LMA) is the standard in TCSPC-FLIM [7]. However, LMA computation is usually slower than acquisition speed, so a real-time per-pixel computation of fluorescence lifetime during imaging (~100 kHz pixel rate) is not feasible. Therefore, unlike fluorescence intensity, which is displayed and analyzed in real-time, fluorescence lifetime is typically computed and analyzed after acquisition in an offline analysis procedure [37]. As a result, it is very common for users to find out only at a later time whether their data collection accurately recorded meaningful changes in fluorescence lifetimes. The lack of real-time visualization of FLIM undermines live cell imaging applications when the microscopist would benefit from visual feedback for determining the length of the experiment or controlling other experimental parameters. Real-time FLIM (RT-FLIM) results would enable users to correct issues, observe dynamic systems, or locate regions of interest (ROIs) for more detailed imaging. Furthermore, real time analysis opens the door to more complex experiment design that might require real-time feedback.

Currently, there are a few closed-source options for RT-FLIM, most that are part of commercial systems. One recently added and popular option for RT-FLIM for laser-scanning microscopy is the commercially available closed-source Leica FALCON system [38]. Other FLIM hardware vendors such as Becker-Hickl, Picoquant, and ISS have their own applications that support a version of real-time FLIM [7,30,39]. Unfortunately, there are currently no open-source options for RT-FLIM, severely limiting access and also preventing code iteration by other FLIM labs.

Here we present an open source RT-FLIM viewer that leverages existing open source components such as the FLIM analysis library FLIMLib and the visualization package Napari [40,41]. Our viewer, named napari-live-flim, is a Napari plugin which, in principle, can be made to interface with any producer of TCSPC-FLIM histogram images. We demonstrate its use with the open-source laser scanning acquisition software OpenScan (https://eliceirilab.org/openscan), which in turn operates as a module for the general microscope image acquisition software Micro-Manager [42,43].

Materials and Methods

We developed our live, interactive FLIM viewer (napari-flim-viewer) in Python as a plugin for the Napari multi-dimensional image viewer [40]. The viewer provides a user interface that is updated as new results are available from incoming image frames. We employed standard Python multithreading techniques to perform the FLIM analysis in the background; results are cached where possible to increase responsiveness.

To transfer FLIM histogram data from acquisition software to napari-live-flim, we used a temporary file for each frame, together with simple UDP messages to notify the viewer of the availability of a new frame. By memory mapping the temporary file on both the sender and receiver side, large amounts of data could be transferred efficiently.

We used FLIMLib for lifetime analysis using LMA, RLD, and phasors. Because FLIMLib is a C library (with Java bindings), we first developed Python bindings for FLIMLib so that the necessary functions could be called [44]. This included adding multi-pixel fitting functions to FLIMLib to facilitate fast analysis by avoiding looping over image pixels in Python code. Python bindings were created using the ctypes standard library module with hand-written wrapper code to check inputs and facilitate usage with NumPy arrays as input and output. These bindings are general and can be used for FLIM analysis outside of napari-live-flim; we released them as a separate Python package (flimlib) with documentation and unit tests. Further validation of the FLIMLib Python Bindings was conducted by performing typical post-acquisition FLIM analysis in a Python Jupyter Notebook. The notebook is available online at *https://github.com/uw-loci/flimlib_python_examples*.

Results

Choice of analysis methods for real-time FLIM

RT-FLIM is primarily focused on time domain based FLIM methods. Most of these methods are focused on single photon counting (SPC), ergo the critical parameters to optimize for in a FLIM viewfinder are fast processing and informative rough lifetime estimation from very low photon counts [7]. As such, to find an appropriate real time methodology which can act as a lifetime viewfinder, we compared four common fast-FLIM techniques including Rapid Lifetime Determination (RLD), Phasor Analysis, Laguerre deconvolution, and Noise Corrected - Primary Component Analysis (NC-PCA). Noise Corrected - Primary Component Analysis (NC-PCA), is of interest since it corrects for the Poisson distribution of noise in the image and Primary Component Analysis is a computationally fast analysis that can quickly provide an estimated relative lifetime score (i.e. not the actual lifetime, but an estimate of the pixel lifetime variance from mean for the image) [11]. Additionally, Phasor Analysis is of interest since it comes from frequency domain FLIM and acts globally on all pixels in an image to estimate the phase and modulation of a single from time-domain data and can separate lifetime distributions by projecting them into a two dimensional space. This two dimensional projection can then be further used to give a lifetime score to each pixel for fast grouping of clusters and with slower computation be used to calculate the actual lifetimes present in individual pixels [12]. Laguerre deconvolution based approaches function similarly to a phasor approach, but rather than

projecting into the frequency domain, they project into Laguerre space. From which a scoring of the lifetimes of pixels in the image can be generated for fast estimation [13]. Furthermore, Rapid Lifetime Determination (RLD) provides a general description of the lifetime decay process and can come in multi-component variants [14]. It provides a significantly faster calculation methodology than a least squares fitting approach and has been shown to provide a fairly accurate calculation of lifetime under most conditions [14]. All methods were compared to each other and to the gold standard LMA [6,11–14,17–20,25,29,30,32,45]. The comparisons were performed on simulated and experimental data. The comparison code and results are available at https://github.com/uw-loci/RT-FLIM. Additionally we benchmarked the relative speed and performance cost of the algorithms. Based on this benchmarking, we found that RLD was the fastest among the tested methods that provide accurate single exponential lifetime estimates. We also determined that phasor analysis is similarly fast and uniquely able to provide multicomponent analysis for multiexponential models in a graphical plot known as phasor-plots [29]. Therefore, we decided to implement both RLD and phasor approaches in the RT-FLIM as analysis options.

Phasor plots and 2D-phasor analysis are powerful tools for visually separating species with separable fluorescence lifetime distributions in an image [9]. We chose phasor analysis aided with RLD as a comprehensive solution for RT-FLIM analysis.

Napari-live-flim architecture

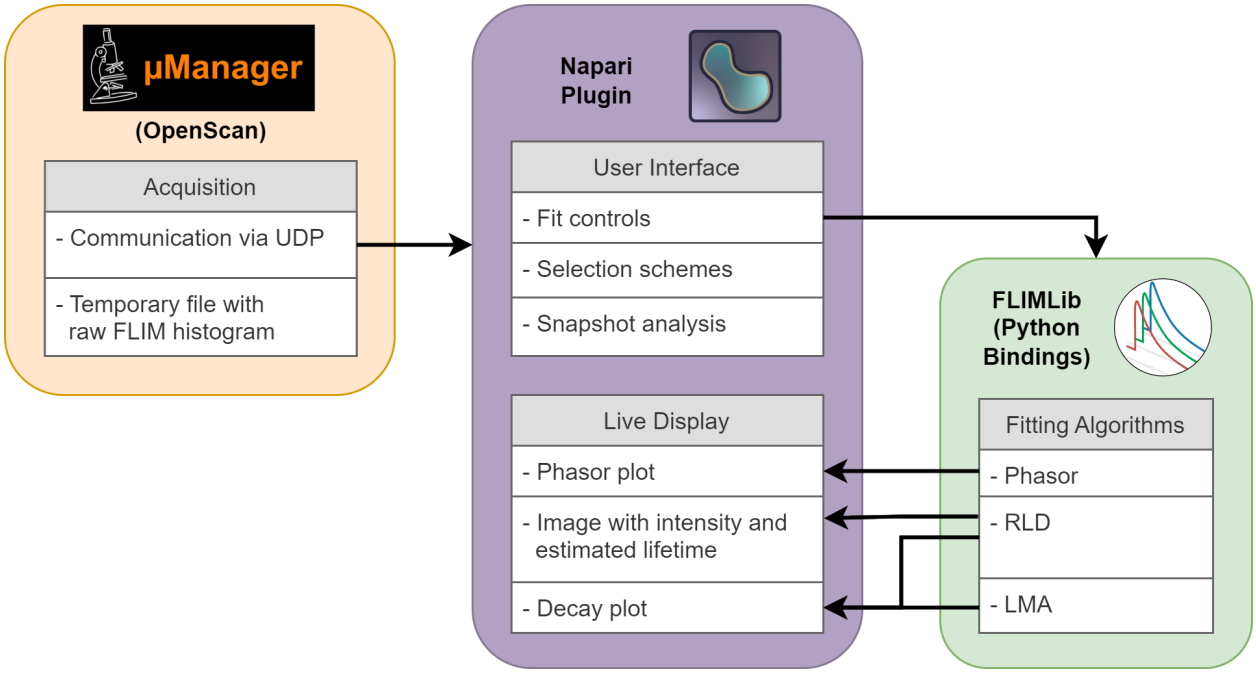

Figure 4.1. Software schematic of napari-live-flim. Raw FLIM histogram data is sent from OpenScan to napari-live-flim via temporary files and signaled by UDP messages. napari-live-flim provides user interaction and visualization of FLIM results which are calculated in real time via the FLIMLib Python Bindings.

Figure 4.1 shows the basic architecture of napari-live-flim, our real-time FLIM viewer. We chose to develop napari-live-flim to run as a separate program from the acquisition software (Micro-Manager and OpenScan), so that it can potentially be attached to different acquisition software. In addition to being a workaround for the lack of support for FLIM datasets in Micro-Manager, this scheme also permitted us to take advantage of NumPy and Napari, which facilitated rapid development of the analysis, display, and user interface.

In order to conduct FLIM analysis in real-time, the computation steps must be short and fast, while maintaining a high-level user interface with a minimal learning curve. We chose to handle all computation of FLIM results within the high performance C programming language and extend the user experience in Python. A strong motivation for choosing C was to utilize FLIMLib, an existing open-source C library for FLIM data analysis co-developed by our group [44]. FLIMLib has an implementation of LMA and many other popular FLIM analysis methods.

Napari-live-flim user interface

Napari-live-flim is a Napari plugin downloadable from the Napari Hub. It offers a variety of controls to let users set FLIM analysis parameters, view fluorescence decay data and fits for selected regions, and take “snapshots” of the live data stream for comparison with subsequent frames.

The fit controls include the range of bins in the FLIM histogram to use in analysis, time resolution, and other fitting parameters. Additionally, users are able to threshold pixels in the Lifetime Image based on fluorescence lifetime and the chi-square (χ^2, metric for goodness of the fit/model) statistic of the RLD estimate. These parameters can be saved to a JSON file to be loaded later for a post-acquisition analysis. The controls are shown in Figure 4.2.

Selections allow users to select certain ROIs or phasor clusters within the Napari windows for more specific and interactive analysis. Selections are made possible through the use of a Napari shapes layer. Shapes layers allow users to create various selection areas such as ellipses, rectangles, and polygons and manipulate their size and position on the display. The screenshot presented in Figure 4.2A shows a view of the plugin. Separate, color coordinated selections can be created, reorganized, hidden, and deleted using the UI (Figure 4.2B). Pixels selected in the Lifetime Image are highlighted within the Phasor Plot, and conversely, phasors selected in the Phasor Plot are highlighted in the Lifetime Image (Figure 4.2B). This correlation feature allows users to select ROIs and determine where they lie on the phasor plot and, in reverse, visualize where certain phasors occur on their sample. By linking these two views, it may be possible to make unique, more confident observations of the data. Lastly, with these selected regions, additional analysis can be performed. By averaging the FLIM histogram data within the selections, analysis can be reduced to a single fit. Therefore, it is possible to run the slow gold standard LMA fitting algorithm on this averaged data. This LMA implementation may be useful to confirm observations made by RLD and Phasor against what can be considered ground truth. Using this averaged histogram data, the LMA and RLD fitted decay curves are displayed on 2D intensity-time axes. Refer to the demonstration of real time FLIM in Video 4.2. The data itself is also plotted as a scatter plot, and two vertical lines delineate the user defined fit range. In the upper right of these decay plots, the numerical results of the LMA and RLD fits are displayed. A major use for the decay plot is to observe the trends in the FLIM histograms in order to assess the quality of the data and set reasonable fitting parameters.

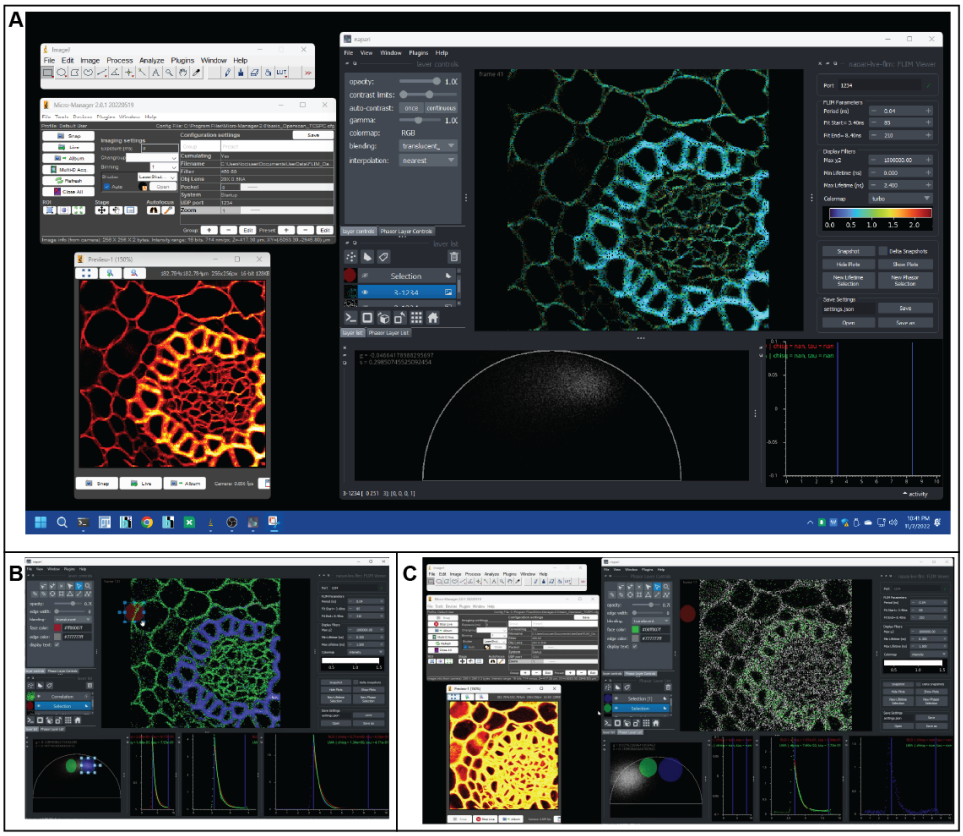

Figure 4.2: Selections The screenshots show how to use phasor based selection to identify FLIM artifacts during a real-time acquisition. A) The screenshot of OpenScan/MicroManager and Napari-FLIM-Viewer operating in real time. The Micromanager window shows the essential Openscan controls and a Preview window that shows intensity image (red hot color). The Napari window shows the fitted lifetime image (turbo colormap) and the phasor distribution. The colors show two regions of interest(ROI) with different lifetime values(green and cyan). B) The two ROI are separated using the phasor cursor selection as blue and green cursors (cursors are shown in the phasor tab and corresponding colored pixels in the image). C) A pile-up artifact generates a clear intensity image (seen in the Micromanager Preview window), but the FLIM data is skewed, seen by the mislocated phasor distribution and lack of expected pixel colors in the selected phasor cursors.

Another useful feature that we added to the napari-live-flim application was the ability to store temporal snapshots of the FLIM data as it arrived. Being able to compare time points in the acquisition is necessary in order to monitor the quality of data as it accumulates and to analyze a specimen that is changing in real time. Another Napari Widget was designed and added with a single button that creates a new snapshot of the current histogrammed FLIM data (Figure 4.3). These snapshots can be revisited by sliding the scrollbar underneath the Lifetime Image(shown by green arrow in Figure 4.3). Snapshots are ordered from oldest to newest; the last snapshot being the one that is reserved for live data. All snapshots can be analyzed in the same manner, allowing for easy comparison. The Video 4.2 shows general working using NLF and a demonstration of the use of delta snapshots during a real time acquisition (at time 3:29). Figure 3 compares two snapshots created on live neuronal culture, separating the FLIM by a temporal breakpoint (associated with a different z-selection in the culture) without stopping or pausing

the multiphoton laser scanning for slicing the collection. This is critical for monitoring the FLIM response to drugs or sample treatments on the fly.

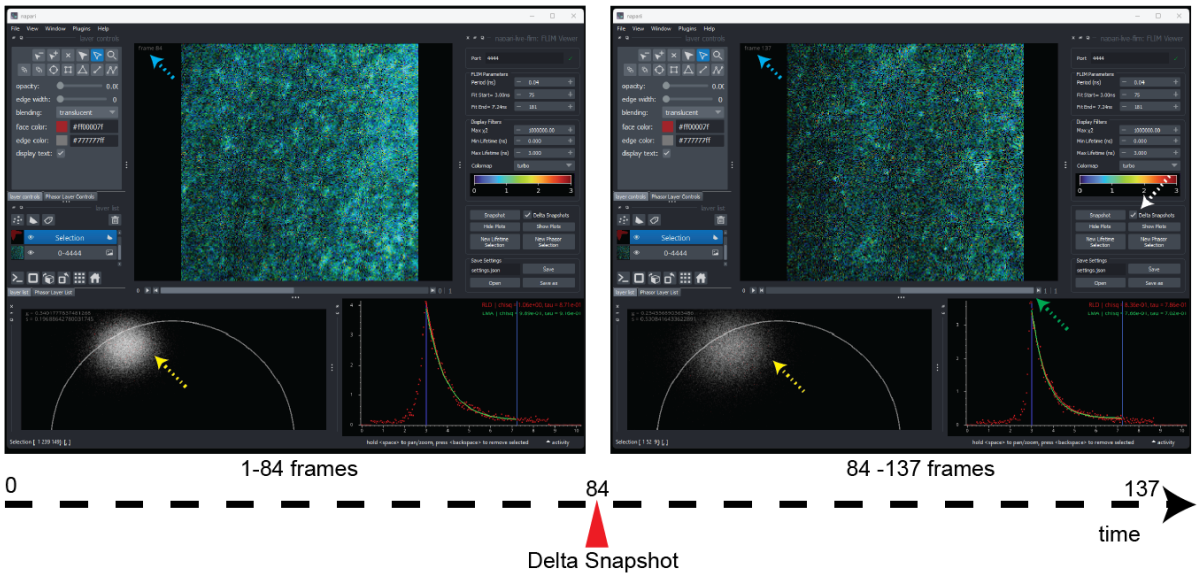

Figure 4.3: Snapshots The screenshot comparison here shows the two snaps from a single FLIM live acquisition. The delta-snapshot (shown by the green dashed arrow) features temporal slicing of incoming FLIM data into different FLIM sub-datasets that can be compared realtime to gain an understanding of signal strength, phasor plot density(yellow dashed arrows) and improvement in fitting accuracy and any changes in the sample that correspond to that section of FLIM data stream. The blue dashed arrows show the current frame number and the green arrow shows the scrollbar which facilitate visualization of the two temporal slices. Note that the screen shots were made post collection.

Usage and Performance

All the described software is open source and available at https://github.com/uw-loci/napari-live-flim. For ease of review and testing, we have provided a sample dataset and simulation of replay option to readers to test our plugin. The sample data is available at Example Dataset (for replay test) and a live demonstration on how to use the sample data is shown in Video 4.3.

A detailed guide on how to set up napari-live-flim with Openscan is provided in the Supplementary Materials. We also provide a video demonstration on how to set up OpenScan and napari-live-flim for real time visualization (Video 4.1) and a video of how the acquisition goes. We also demonstrate live chlorophyll fluorescence from Arabidopsis Thaliana samples.

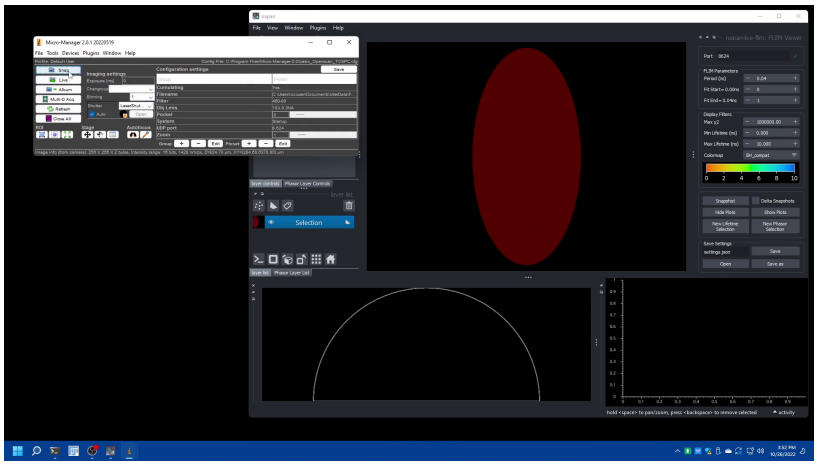

Video 4.1: Initializing the collection OpenScan and NapariLiveFlimViewer
Demonstration of Initializing napari-live-flim

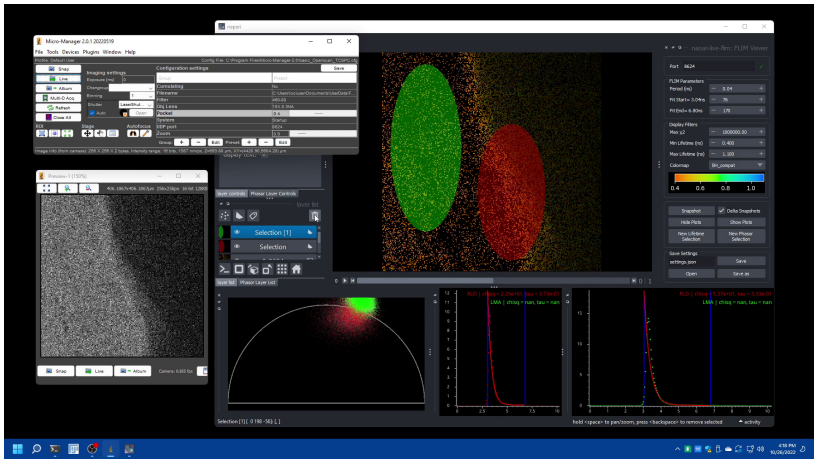

Video 4.2:
Demonstration of Real time Acquisition

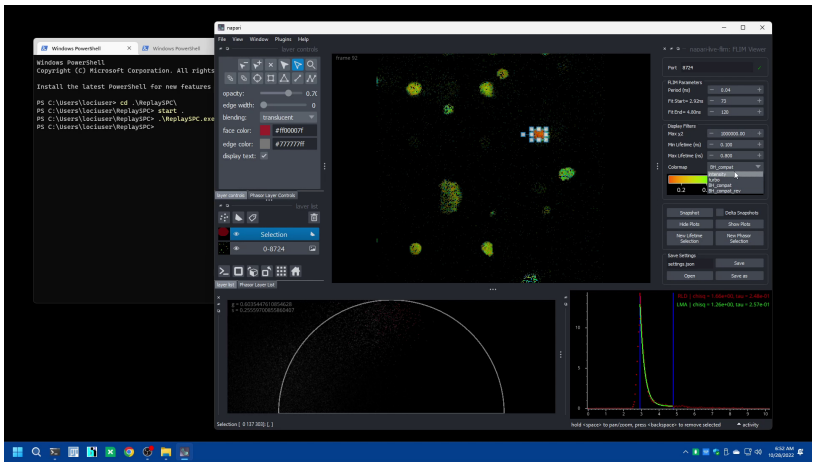

Video 4.3:
Demonstration of Replay of SPC file and visualization in napari-live-flim

Performance: We tested the overall speed of napari-live-flim to make sure that it is capable of keeping up with imaging. We ran benchmarks by sending a test FLIM dataset with 50 frames, each with 256x256 pixels and 256 time bins at a rate of 2 frames per second (Table 4.2). These benchmarks were performed on a 64-bit Windows PC with an Intel Core i5-7300HQ 2.5GHz CPU and 8GB of 2133 MHz RAM. A total of 49 frames were processed by napari-live-flim which computed a lifetime image and phasor plot on separate threads. The median time it took between the arrival of data and display of results was 124 ms. The median time that was taken to create the lifetime image and phasor plot was 116 and 34.5 ms respectively. Since a typical scan rate for TCSPC FLIM with this image size is about 300 ms per frame, we conclude that our analysis can keep up with most acquisitions [7]. Due to the way we queue incoming data, we ensure that we remain synced with acquisition by only processing the most recent accumulated frame. This occasionally results in a frame not being processed which explains why only 49 out of the 50 frames were processed in our test. It should be noted that utilization of our selection feature creates some overhead, especially with large selection areas and many selections. However, since these tasks run on separate threads, we found that for reasonable selections, the added computational load is manageable.

Table 4.2. Benchmark Table for live-FLIM imaging

Computation step after arrival of new data	Median Time (ms)
Lifetime image (RLD)	116
Phasor plot	34.5
Overall processing time of new frame	124

Discussion

Phasor based contrast in FLIM has been attributed to frequency domain techniques for the past couple of decades, and it mostly belongs to a single commercial vendor [29,30]. Many instances of academic solutions were proposed in the period that could generate phasor plots but were limited in scope due to closed source codes that severely limited sharing and extensibility [46–48]. Napari-Live-FLIM is the first open source solution to handle live phasor plots and provide nDimensional filtering on a real-time FLIM acquisition. This easily installed and customizable plugin allows microscopes to be set up for real-time FLIM analysis. Predetermined values for FLIM collection from the hardware can make the operations easier and make napari-live-flim suitable for microscopy cores that allow FLIM imaging facilities to users. RLD-based analysis, however, has a lot of open-sourced solutions and provides straightforward computation, but is limited to a smaller group of users who use the FLIM technique in on-board implementations of FLIM analysis for mutipixel-FPGA and CMOS/FLIM cameras [49,50]. Napari-live-flim proposes a unique RLD-based live estimation of pixel-wise lifetimes that offers a preview of the FLIM image, aided with simultaneous phasor plots that can address the distribution of lifetimes and quality of the FLIM data.

Napari-live-flim offers ROI-based fitting that enables users to fit a group of pixels of interest, brought together either by phasor or spatial features. The fitting is performed in LMA and

generates a confidence map that could allow the user to determine the collection time for their experiment. Integrating the method with Napari makes it possible to integrate other image-analysis routines into FLIM analysis and deploy them in a real-time manner for feedback. For example, use of 3D filters and segmentation can separate regions of interest and allow users to focus collection on their interests. This is important, as many GPU-based image optimization algorithms are readily available in Napari (https://github.com/haesleinhuepf/napari-cupy-image-processing) and through community-driven napari-hub. Moreover, an image analysis pipeline can easily be integrated into the napari-console for exporting FLIM outputs for analysis outside Python.

The different parts of our open source software: FLIMLib, OpenScan, and napari-live-flim are modular and could be improved, upgraded, and updated without affecting each other. Current tests we demonstrate are using the OpenScan framework that supports laser scanning microscopy under the Micromanager program. However, this bridge is completely modular, allowing users to adapt the viewer to other FLIM control systems.

The key feature of our library is the open-sourced architecture, which is built upon all open-sourced components. Program solutions such as FlimLib and FLIMJ offered an open source FLIM analysis solution that could do fitting and exponential-library analyses, but was limited by the inherent limitations of the programming language they were written in. Extending FlimLib to Python for exponential curve analysis encourages the larger Python based scientific community to read and contribute to the project and the progress of FLIM-based analysis tools. Exponential fitting methods used in the project are not limited to FLIM and can be extended to non-FLIM applications that could use fast real-time analysis of exponential curves or arrays of exponential curves.

Conclusions

We present an open-source tool for real-time analysis of FLIM data during acquisition called napari-live-flim. Currently, it is integrated into OpenScan and available as a Napari plugin. This tool enables efficient and informative data collection of FLIM. Moving forward, this tool can be improved through further code optimization, caching for loading, threading for parallelization, and the use of specific hardware to handle different data acquisition setups. Upgrades of the application can enable higher throughput FLIM systems. Currently, napari-live-flim provides phasor based analysis of the data, but due to its open source nature and the potential of the methodology, it is set up to be readily expandable with alternate analysis methods such as NC-PCA, Laguerre, and more.

Chapter 4 References

1. Tian L, Liu Z, Yeh LH, Chen M, Zhong J, Waller L. Computational illumination for high-speed in vitro Fourier ptychographic microscopy. Optica. 2015 Oct 20;2(10):904–11.
2. Kam Z, Hanser B, Gustafsson MGL, Agard DA, Sedat JW. Computational adaptive optics for live three-dimensional biological imaging. Proc Natl Acad Sci. 2001 Mar 27;98(7):3790–5.
3. Albert O, Sherman L, Mourou G, Norris TB, Vdovin G. Smart microscope: an adaptive optics learning system for aberration correction in multiphoton confocal microscopy. Opt Lett. 2000 Jan 1;25(1):52–4.
4. Eisenstein M. Smart solutions for automated imaging. Nat Methods. 2020 Nov;17(11):1075–9.
5. Scherf N, Huisken J. The smart and gentle microscope. Nat Biotechnol. 2015 Aug;33(8):815–8.
6. Zhu X, Zhang D. Efficient Parallel Levenberg-Marquardt Model Fitting towards Real-Time Automated Parametric Imaging Microscopy. PLOS ONE. 2013 Oct 10;8(10):e76665.
7. Becker W. The bh TCSPC Handbook 8th ed. [Internet]. 8th ed. 2019 [cited 2021 Aug 2]. Available from: https://www.becker-hickl.com/literature/documents/flim/the-bh-tcspc-handbook/
8. Liu X, Lin D, Becker W, Niu J, Yu B, Liu L, et al. Fast fluorescence lifetime imaging techniques: A review on challenge and development. J Innov Opt Health Sci. 2019 Sep 1;12(05):1930003.
9. Datta R, Heaster TM, Sharick JT, Gillette AA, Skala MC. Fluorescence lifetime imaging microscopy: fundamentals and advances in instrumentation, analysis, and applications. J Biomed Opt. 2020 May;25(7):071203.
10. Wahl M, Röhlicke T, Kulisch S, Rohilla S, Krämer B, Hocke AC. Photon arrival time tagging with many channels, sub-nanosecond deadtime, very high throughput, and fiber optic remote synchronization. Rev Sci Instrum. 2020 Jan 1;91(1):013108.
11. Marois AL, Labouesse S, Suhling K, Heintzmann R. Noise-Corrected Principal Component Analysis of fluorescence lifetime imaging data. J Biophotonics. 2017;10(9):1124–33.
12. Lakner PH, Monaghan MG, Möller Y, Olayioye MA, Schenke-Layland K. Applying phasor approach analysis of multiphoton FLIM measurements to probe the metabolic activity of three-dimensional in vitro cell culture models. Sci Rep. 2017 Feb 13;7(1):42730.
13. Pande P, Jo JA. Automated Analysis of Fluorescence Lifetime Imaging Microscopy (FLIM) Data Based on the Laguerre Deconvolution Method. IEEE Trans Biomed Eng. 2011 Jan;58(1):172–81.
14. Ballew RM, Demas JN. An error analysis of the rapid lifetime determination method for the evaluation of single exponential decays. Anal Chem. 1989 Jan 1;61(1):30–3.
15. OpenScan – Laboratory for Optical and Computational Instrumentation [Internet]. [cited 2021 Aug 2]. Available from: https://eliceirilab.org/openscan/
16. van Munster EB, Gadella TWJ. Fluorescence Lifetime Imaging Microscopy (FLIM). In: Rietdorf J, editor. Microscopy Techniques: -/- [Internet]. Berlin, Heidelberg: Springer; 2005 [cited 2021 Aug 2]. p. 143–75. (Advances in Biochemical Engineering). Available from: https://doi.org/10.1007/b102213
17. Digman MA, Caiolfa VR, Zamai M, Gratton E. The Phasor Approach to Fluorescence Lifetime Imaging Analysis. Biophys J. 2008 Jan 15;94(2):L14–6.
18. Jo JA, Fang Q, Marcu L. Ultrafast method for the analysis of fluorescence lifetime imaging microscopy data based on the Laguerre expansion technique. IEEE J Sel Top Quantum Electron. 2005 Jul;11(4):835–45.
19. Sharman KK, Periasamy A, Ashworth H, Demas JN. Error Analysis of the Rapid Lifetime Determination Method for Double-Exponential Decays and New Windowing Schemes.

Anal Chem. 1999 Mar 1;71(5):947–52.
20. Silva SF, Domingues JP, Morgado AM. Can we use rapid lifetime determination for fast, fluorescence lifetime based, metabolic imaging? Precision and accuracy of double-exponential decay measurements with low total counts. PLOS ONE. 2019 May 14;14(5):e0216894.
21. Sagar MAK, Cheng KP, Ouellette JN, Williams JC, Watters JJ, Eliceiri KW. Machine Learning Methods for Fluorescence Lifetime Imaging (FLIM) Based Label-Free Detection of Microglia. Front Neurosci. 2020 Sep 3;14:931.
22. Hwang W, Kim D, Lee S, Won YJ, Moon S, Kim DY. Analysis of biexponential decay signals in the analog mean-delay fluorescence lifetime measurement method. Opt Commun. 2019 Jul 15;443:136–43.
23. Schönle A, Glatz M, Hell SW. Four-dimensional multiphoton microscopy with time-correlated single-photon counting. Appl Opt. 2000 Dec 1;39(34):6306–11.
24. Brismar H, UIfhake B. Fluorescence lifetime measurements in confocal microscopy of neurons labeled with multiple fluorophores. Nat Biotechnol. 1997 Apr;15(4):373–7.
25. Gavin HP. The Levenberg-Marquardt algorithm for nonlinear least squares curve-fitting problems. 2020;19.
26. Gorbunova IA, Sasin ME, Golyshev DP, Semenov AA, Smolin AG, Beltukov YM, et al. Two-Photon Excited Fluorescence Dynamics in Enzyme-Bound NADH: the Heterogeneity of Fluorescence Decay Times and Anisotropic Relaxation. J Phys Chem B. 2021 Sep 2;125(34):9692–707.
27. Moré JJ. The Levenberg-Marquardt algorithm: Implementation and theory. In: Watson GA, editor. Numerical Analysis. Berlin, Heidelberg: Springer; 1978. p. 105–16. (Lecture Notes in Mathematics).
28. Digman MA, Gratton E. The phasor approach to fluorescence lifetime imaging: Exploiting phasor linear properties. :14.
29. Ranjit S, Malacrida L, Jameson DM, Gratton E. Fit-free analysis of fluorescence lifetime imaging data using the phasor approach. Nat Protoc. 2018 Sep;13(9):1979–2004.
30. Liao SC, Sun Y, Coskun U. FLIM Analysis using the Phasor Plots. :13.
31. Chen LC, Lloyd WR, Chang CW, Sud D, Mycek MA. Chapter 20 - Fluorescence Lifetime Imaging Microscopy for Quantitative Biological Imaging. In: Sluder G, Wolf DE, editors. Methods in Cell Biology [Internet]. Academic Press; 2013 [cited 2021 Nov 24]. p. 457–88. (Digital Microscopy; vol. 114). Available from: https://www.sciencedirect.com/science/article/pii/B9780124077614000208
32. Fereidouni F, Gorpas D, Ma D, Fatakdawala H, Marcu L. Rapid fluorescence lifetime estimation with modified phasor approach and Laguerre deconvolution: a comparative study. Methods Appl Fluoresc. 2017 Sep;5(3):035003.
33. Ma Z, Wu J, Zhong S hua, Jiang J, Heinen SJ. Human Eye Movements Reveal Video Frame Importance. Computer. 2019 May;52(5):48–57.
34. Bastiaens PIH, Squire A. Fluorescence lifetime imaging microscopy: spatial resolution of biochemical processes in the cell. Trends Cell Biol. 1999 Feb 1;9(2):48–52.
35. Bird DK, Yan L, Vrotsos KM, Eliceiri KW, Vaughan EM, Keely PJ, et al. Metabolic Mapping of MCF10A Human Breast Cells via Multiphoton Fluorescence Lifetime Imaging of the Coenzyme NADH. Cancer Res. 2005 Oct 3;65(19):8766–73.
36. Chacko JV, Eliceiri KW. Autofluorescence lifetime imaging of cellular metabolism: Sensitivity toward cell density, pH, intracellular, and intercellular heterogeneity. Cytometry A. 2019;95(1):56–69.
37. Becker W. Advanced Time-Correlated Single Photon Counting Techniques. Springer Science & Business Media; 2005. 414 p.
38. Application Note: SP8 FALCON: a novel concept in fluorescence lifetime imaging enabling video-rate confocal FLIM. [cited 2022 Nov 15]; Available from:

https://www.nature.com/articles/d42473-019-00261-x
39. Orthaus-Mueller S, Kraemer B, Dowler R, Devaux A, Tannert A, Roehlicke T, et al. rapidFLIM: The New and Innovative Method for Ultra fast FLIM Imaging. :8.
40. Sofroniew N, Lambert T, Evans K, Nunez-Iglesias J, Bokota G, Winston P, et al. napari: a multi-dimensional image viewer for Python [Internet]. 2022 [cited 2022 Apr 29]. Available from: https://github.com/napari/napari
41. Gao D, Barber PR, Chacko JV, Sagar MAK, Rueden CT, Grislis AR, et al. FLIMJ: An open-source ImageJ toolkit for fluorescence lifetime image data analysis. PLOS ONE. 2020 Dec 30;15(12):e0238327.
42. Edelstein AD, Tsuchida MA, Amodaj N, Pinkard H, Vale RD, Stuurman N. Advanced methods of microscope control using μManager software. J Biol Methods. 2014;1(2):e10.
43. Edelstein A, Amodaj N, Hoover K, Vale R, Stuurman N. Computer Control of Microscopes Using μManager. Curr Protoc Mol Biol. 2010;92(1):14.20.1-14.20.17.
44. FLIMLib [Internet]. [cited 2021 Nov 22]. Available from: https://flimlib.github.io/
45. Levenberg K. A method for the solution of certain non-linear problems in least squares. Q Appl Math. 1944 Jul 1;2(2):164–8.
46. Schrimpf W, Barth A, Hendrix J, Lamb DC. PAM: A Framework for Integrated Analysis of Imaging, Single-Molecule, and Ensemble Fluorescence Data. Biophys J. 2018 Apr 10;114(7):1518–28.
47. Sorrells JE, Sorrells JE, Iyer RR, Iyer RR, Yang L, Yang L, et al. Real-time pixelwise phasor analysis for video-rate two-photon fluorescence lifetime imaging microscopy. Biomed Opt Express. 2021 Jul 1;12(7):4003–19.
48. Yaseen MA, Sutin J, Wu W, Fu B, Uhlirova H, Devor A, et al. Fluorescence lifetime microscopy of NADH distinguishes alterations in cerebral metabolism in vivo. Biomed Opt Express. 2017 May 1;8(5):2368–85.
49. Zang Z, Xiao D, Wang Q, Jiao Z, Yu C, Li DDU. Compact and Robust Deep Learning Architecture for Fluorescence Lifetime Imaging and FPGA Implementation [Internet]. arXiv; 2022 [cited 2022 Nov 15]. Available from: http://arxiv.org/abs/2209.03272
50. Henderson RK, Rae BR, Li DU. 11 - Complementary metal-oxide-semiconductor (CMOS) sensors for fluorescence lifetime imaging (FLIM). In: Durini D, editor. High Performance Silicon Imaging [Internet]. Woodhead Publishing; 2014 [cited 2022 Nov 15]. p. 312–47. Available from: https://www.sciencedirect.com/science/article/pii/B9780857095985500117

Chapter 5: Image Processing Tools in ImageJ Scripting

While much of my previous work has been focused on providing easily usable tools for computational imaging utilizing MATLAB, unfortunately MATLAB is not a true open source code base since it is not an open source framework [1]. So while it provides a fantastic programming environment for manipulation of images and prototyping, there's a need to provide ready access to other open source environments. ImageJ is one such environment that was designed for images [2–5]. It provides a powerful scripting interface that enables developing algorithmic routines for processing of images and has a large network of users that further develop its capabilities through plugins [6–10]. That said, it is difficult to get accustomed to, particularly if one is coming from a primarily MATLAB background. Therefore this paper was written to provide some easy introductions to the ImageJ/FIJI environment and display different ways in which a user can interact with it. To further improve the accessibility and understanding of common ImageJ methods, we wrote use cases that show off primary features such as PyImageJ, ImageJ Ops, and Headless ImageJ through common imaging problems and tasks [2,4–6]. To understand these methods and cases deeper we further provide insight into how each input will affect the methods, how common errors are caused, and what the results mean. These scripts can be used as a basis to expand upon and develop more customized routines for users' individual applications.

Adapted from "New Extensibility and Scripting Tools in the ImageJ EcoSystem" Gahm, Niklas A., Rueden, Curtis T., Evans III, Edward L., Selzer, Gabriel, Hiner, Mark C., Chacko, Jenu V., Gao, Dasong, Sherer, Nathan M., Eliceiri, Kevin W., Current Protocols

Summary

ImageJ provides a framework for image processing across scientific domains whilst being fully open source. Over the years ImageJ has been substantially extended to support novel applications in scientific imaging as they emerge, particularly in the area of biological microscopy, with functionality made more accessible via the Fiji distribution of ImageJ. Within this software ecosystem, work has been done to extend the accessibility of ImageJ to utilize scripting, macros, and plugins in a variety of programming scenarios such as from Groovy and Python and in Jupyter notebooks and cloud computing. We provide five protocols that demonstrate the extensibility of ImageJ for various workflows in image processing. We focus first on Fluorescence Lifetime Imaging Microscopy (FLIM) data since it requires significant processing to provide quantitative insights into the microenvironments of cells. Secondly, we

show how ImageJ can now be utilized for common image processing techniques, specifically image deconvolution and inversion while highlighting the new built in features of ImageJ. Particularly its capacity to run completely headless and the Ops matching feature that selects the optimal algorithm for a given function and data input thereby enabling processing speedups. Collectively these protocols can be used as a basis for automating biological image processing workflows.

Basic Protocol 1: Using PyImageJ for FLIM Data Processing
Alternate Protocol 1: Groovy FLIMJ in Jupyter Notebooks

Basic Protocol 2: Using ImageJ Ops for Image Deconvolution
Support Protocol 1: Using ImageJ Ops Matching Feature for Image Inversion
Support Protocol 2: Headless ImageJ Deconvolution

Keywords: ImageJ, Fiji, image analysis, scripting, Python, Jython, Ops, SciJava, Lifetime analysis, Deconvolution

Introduction

ImageJ is an open-source software tool for multidimensional image analysis, routinely used in the scientific imaging community [3]. It is usable in multiple forms, including as an end-user application, as a suite of software libraries, and as an extensible framework for writing your own image analysis plugins and scripts [2]. The ImageJ user and developer community has produced thousands of such plugins and scripts which can be reused and customized in diverse ways [4,5].

In the pursuit of extensibility and workflow optimization, ImageJ evolved from a standalone program developed at the National Institutes of Health into the Fiji and ImageJ2 projects co-developed across several organizations and targeting a broader range of technical requirements [2,11,5]. Over the years, these architectural improvements to ImageJ have fostered the growth of a collaborative ecosystem of cross-compatible frameworks and software, enabling ImageJ to be combined more effectively with other tools useful in the field of scientific imaging, including KNIME Analytics Platform, CellProfiler, MATLAB, and others [7,12,8,13]. This reengineering work unified ImageJ's algorithmic infrastructure under the ImageJ Ops framework, which enables programmers to create multiple versions of an algorithm targeting different specialized inputs in a way transparent to users calling the algorithms from scripts. It also extended ImageJ scripting support, useful for workflow automation, to more languages, as demonstrated in the variety of protocols we present in this manuscript. The scripts presented here illustrate the ability to invoke ImageJ's algorithmic functionality in contexts other than just the graphical user interface, including: headless mode as part of an interprocess workflow involving multiple analysis tools; via the PyImageJ library enabling the use of ImageJ from a Python environment; and from Jupyter Notebook, a scientific notebook tool useful for

encapsulating the steps of data analysis protocols and workflows in a visual, interactive, and reproducible way [14,15].

The development of ImageJ's new features has been driven by the major revolution optical microscopy has experienced in the last 25 years with the advent of significantly advanced optical imaging technology from classical brightfield microscopes to highly advanced approaches like super resolution microscopy [16]. As these methods are developed there is a collective need for corresponding image processing and analysis methods to be developed. Particularly in a research setting, building on the work of others is critical therefore an open-source framework such as ImageJ is invaluable for research within this field as it develops. Particularly, fluorescence imaging has been significantly expanded and developed since it is capable of correlating phenotypic function and genetics [17,18]. This has led to the usage of fluorescence microscopy in a wide number of biological research areas including cancer biology, cell trafficking, and pathogenetic studies [17,19–22]. The core of fluorescence microscopy has been even further expanded via the development of fluorescence lifetime imaging microscopy (FLIM) which has seen increased adoption by biologists in recent years for its quantitative sensing of the state of cellular micro-environments spatially and temporally [23,24]. While fluorescence lifetime has previously been used by chemists to detect the pH of a micro-environment, the binding state of a molecule, and more, FLIM provides imaging based information of the spatial distribution of these metrics within a sample [24,25]. Given the importance of this method and its inherent computational challenges, we present, as Basic Protocol 1, an open-source protocol for FLIM image processing independent of the underlying acquisition software. This protocol leverages FLIMJ through PyImgJ's headless ImageJ extensible scripting mode.

In the following two protocols, we showcase how to use ImageJ for image data processing, how readily it can be automated for routine system data processing, and the ease of extending ImageJ for workflows. We focus on FLIM data processing in *Basic Protocol 1: Using PyImageJ for FLIM Data Processing*, by leveraging the FLIMJ library through PyImageJ for lifetime component fitting in Jupyter Notebooks without interacting with the ImageJ user interface[9]. In *Alternate Protocol 1: Groovy FLIMJ in Jupyter Notebooks*, we show that the same lifetime fitting can be done through the Groovy programming language. Whilst these first two protocols are focused on processing raw data collected via a specific imaging modality, FLIM, the remaining protocols are all centered on using ImageJ for general image processing methods. In *Basic Protocol 2: Using ImageJ Ops for Image Deconvolution* we provide an example on how to perform image deconvolution with ImageJ in Jython, demonstrating the poly-glottal nature of ImageJ.

To deepen the readers understanding of one of the main features of the newest version of ImageJ we show the built-in Ops matching in *Support Protocol 1: Using ImageJ Ops Matching Feature for Image Inversion*. This protocol is centered around demonstrating Ops' matching feature that will intelligently determine the best algorithm available within its scope for a given function and input type on a simplistic example of image inversion. This further illustrates the increased polyglot nature of ImageJ by being executed with a Groovy script as well as Jython in

the underlying *Basic Protocol 2*. Finally, to display how readily the power of ImageJ for image processing can be integrated into larger computing environments (*e.g.* computing clusters), we show how to use ImageJ without a graphical user interface in *Support Protocol 2: Headless ImageJ Deconvolution*, which presents a deconvolution script that can be run from the command line.

Basic Protocol 1

Using PyImageJ for FLIM Processing

Introductory Paragraph

This protocol uses PyImageJ to run FLIMJ and process Fluorescence Lifetime Imaging Microscopy (FLIM) datasets and extract individual pixel fluorescence lifetimes within a Jupyter Notebook. Using this protocol, it is possible to estimate fluorescence lifetimes using curve-fitting routines without the need to use a third party proprietary software.

Materials:

This protocol has been tested with the following configuration:

- ❏ Windows 10 operating system
- ❏ Version 2.1.0/1.53c of Fiji (https://imagej.net/Fiji.html#Downloads)
- ❏ Version 1.0.0 of FLIMJ (Installation process described in the Protocol Steps)
- ❏ Version 1.10.0 of Anaconda Navigator (https://www.anaconda.com/products/individual)
- ❏ Version 1.0.0 of PyImageJ (Installation process described in the Protocol Steps)
- ❏ Version 6.2.0 of Jupyter Notebook (Installation process described in the Protocol Steps)
- ❏ Version 1.30 of BeakerX (Installation process described in the Protocol Steps)
- ❏ The following files are all freely available:
    - ❏ BP1_PyImageJ.ipynb (https://github.com/uw-loci/ScriptingExampleForFLIMJandOps/blob/main/FLIM_DataProcessing/BP1_PyImageJ_FLIM_Notebook/BP1_PyImageJ.ipynb)
    - ❏ read_wiscscan_sdt.py (https://github.com/uw-loci/ScriptingExampleForFLIMJandOps/blob/main/FLIM_DataProcessing/BP1_PyImageJ_FLIM_Notebook/read_wiscscan_sdt.py)
    - ❏ Example dataset: epithelial_human_FLIM.sdt (https://zenodo.org/record/4642146/files/epithelial_human_FLIM.sdt)

Protocol Steps:

Setup:

1. Install FLIMJ Plugin for FIJI
    a. Open the local install of FIJI

   b. Open the ImageJ Updater by selecting “Help → Update...”
   c. Open the Update Site List by selecting “Manage update sites” in the bottom left corner of the window
   d. In the list of Update sites scroll down and check “FLIMJ”
   e. Close the “Manage update sites” window
   f. Select “Apply Changes” in the “ImageJ Updater” Window
   g. Restart FIJI
2. Start Anaconda Navigator
3. Install PyImageJ Environment
   a. Launch the command terminal from Anaconda Navigator
   b. Type in Commands:
      i. conda create -n pyimagej -c conda-forge pyimagej openjdk=8
      ii. conda activate pyimagej
4. Switch to the PyImageJ Environment in Anaconda Navigator by selecting it from the dropdown menu next to “Applications on”
5. Install BeakerX and PyWidgets
   a. Launch the command terminal from Anaconda Navigator
   b. Type in Commands:
      i. conda install -c conda-forge ipywidgets beakerx
6. Install sdtfile module
   a. Launch the command terminal from Anaconda Navigator
   b. Type in Commands:
      i. conda install -c conda-forge sdtfile
7. On the Jupyter Notebooks Panel select install
8. Once installed select launch
9. On the Jupyter Notebooks screen navigate to the directory where BP1_PyImageJ.ipynb and epithelial_human_FLIM.sdt were downloaded
10. Open BP1_PyImgJ.ipynb
11. In the User Input code block, change “filename” to the path for the sample data set.
12. In the User Input code block, change “ij_local_installation” to the full path to your local FIJI installation.
13. Then run the User Input code block
14. On the screen select the code block under “Dependencies” and run it.

    This will install all the libraries and dependencies necessary to read in sdt data and perform lifetime fitting in the notebook.

15. Scroll down to the block of “File Read In” and then sequentially run the two blocks.

    This first loads in a 3-dimensional image file to be processed from the associated testing data. Then analyzes the 3-dimensional image file to determine the dimensions and displays the summation of all collected photons.

16. Scroll down to the code block for “Lifetime Fitting” and then sequentially run the two blocks.

    This performs lifetime fitting on the data and displays how long the fitting process took.

17. Finally scroll down to the code block for “Plot Fitted Results” and then sequentially run the two blocks.

    This plots the Offset, Amplitude, and Lifetimes of the fitted data.

Sample Data:

This protocol was designed to operate on fluorescence lifetime data sets and is shown in this protocol running on epithelial_human_FLIM.sdt. The underlying sample is unstained epithelial cells from human mammary gland tissue with fibrocystic disease. NAD(P)H auto-fluorescence signal was collected with 740nm multiphoton excitation and 460/80 spectral emission range. The hardware used was a Nikon Apo 40x water immersion objective with a 1.25 NA and a SPC-150 Becker & Hickl Time correlated Single Photon Counting electronics.

Alternate Protocol 1

Groovy FLIMJ in Jupyter Notebooks

Introductory Paragraph

This protocol extends the basic protocol for Groovy and FLIMJ to be run through Jupyter Notebooks. This methodology enables Groovy to run FLIMJ to process FLIM datasets and extract individual pixel fluorescence lifetimes in an annotable graphic interface thereby improving repeatability and consistency across data processing.

Materials:

This protocol has been tested with the following configuration:

- ❏ Windows 10 operating system
- ❏ Version 1.10.0 of Anaconda Navigator (https://www.anaconda.com/products/individual)
- ❏ Version 6.2.0 of Jupyter Notebook (Installation process described in the Protocol Steps)
- ❏ Version 1.30 of BeakerX (Installation process described in the Protocol Steps)
- ❏ The following files are all freely available:
    - ❏ AP1_FLIM_Notebook.ipynb (https://github.com/uw-loci/ScriptingExampleForFLIMJandOps/blob/main/FLIM_DataProcessing/AP1_Groovy_FLIM_Notebook/AP1_FLIM_Notebook.ipynb)

- ❏ Example dataset: epithelial_human_FLIM.sdt (https://zenodo.org/record/4642146/files/epithelial_human_FLIM.sdt)

Protocol Steps:

Setup:

1. Start Anaconda Navigator
2. Install BeakerX and PyWidgets
    a. Launch the command terminal from Anaconda Navigator
    b. Type in Commands:
        i. conda install -c conda-forge ipywidgets beakerx
3. On the Jupyter Notebooks Panel select install
4. Once installed select launch
5. On the Jupyter Notebooks screen navigate to the directory where AP1_FLIM_Notebook.ipynb and epithelial_human_FLIM.sdt were downloaded
6. Open AP1_FLIM_Notebook.ipynb
7. Change the kernel to Groovy by selecting Groovy in “Kernel → Change kernel”
8. On the screen select the code block under “Dependencies” and run it.

    This will install all the libraries and dependencies necessary to run FLIMJ in the notebook. It is possible this step can cause errors. If so, see Troubleshooting.

9. Scroll down to the block of “Utility Code” and run it.

    This sets up the displays for the data.

10. Scroll down to the code block for “Loading Dataset” and then sequentially run the two blocks.

    This first loads in a 3-dimensional image file to be processed from the associated testing data. Then analyzes the 3-dimensional image file to determine the dimensions and displays the raw photon counts of time bin 45.

11. Scroll down to the code block for “Hyperparameter Setup” and run it.

    This calculates the parameters to be used for lifetime fitting.

12. Finally scroll down to the code block for “Performing Image Fitting” and then sequentially run the blocks to step through the process.

    This is where image fitting actually occurs and presents two forms of Levenberg-Marquardt Algorithm fitting, Global Fitting, and Multi-Component Fitting (1, 2, and 3 components). It further displays two common data processing elements: Region of Interest, and Binning both for improved processing speeds in scenarios with large data sets.

Sample Data:

The AP1_FLIM_Notebook.ipynb script was designed to operate on spectral fluorescence lifetime data sets and is shown in this protocol running on epithelial_human_FLIM.sdt. The underlying sample is unstained epithelial cells from human mammary gland tissue with fibrocystic disease. NAD(P)H auto-fluorescence signal was collected with 740nm excitation and 460/80nm bandpass emission. The images were collected with a lab built multiphoton system and a Nikon Apo 40x 1.25 NA water immersion objective and a Becker & Hickl Time Correlated Single Photon Counting system.

Basic Protocol 2

Using ImageJ Ops for Image Deconvolution

Introductory Paragraph

The ImageJ Ops framework enables easy access to a large library of image processing functions. Image deconvolution is a common operation in image processing for microscopy, as it can notably increase the contrast and resolution of a captured data set. This is done by calculating the point spread function (PSF) at each z-level, then using a reconstruction technique to remove the effects of the PSF, specifically aberrations, from the captured image and reduce the light blurring present in the image. In this example we use a script written in Jython, a Python implementation on the Java platform. Jython is able to import and use any Java class, enabling easy access to ImageJ's Java libraries with a familiar Python language syntax.

Materials:

This protocol has been tested with the following configuration:

- ❏ Windows 10 and Ubuntu 20.04 LTS operating systems
- ❏ Version 2.1.0/1.53c of Fiji (https://imagej.net/Fiji.html#Downloads)
- ❏ The following files are all freely available:
  - ❏ Decon_richardsonLucyTV.py (https://github.com/uw-loci/ScriptingExampleForFLIMJandOps/tree/main/RL_Deconvolution/BP2_ImageJ_Ops_Deconvolution)
  - ❏ Example dataset: HeLa_microtubules.tif (https://zenodo.org/record/4642146/files/HeLa_microtubules.tif)

Protocol Steps:

1. Start Fiji

2. Load the input image into Fiji using “File → Open” or by drag & drop. The example data set “HeLa_microtubules.tif”.
3. Load Decon_richardsonLucyTV.py using “File → Open” or by drag & drop. The script opens within the script editor.
4. Run the Decon_richardsonLucyTV.py script from the open script editor.
5. A pop-up with variables will appear, the variables are explained further in the Critical Parameters Section. Select “Okay”.

   Automatically the script will open two windows one that displays the deconvolved image stack and one that displays the point spread function across the image stack.

Sample Data:

The Decon_richardsonLucyTV.py script was designed to operate on any z-stack but is shown in this protocol operating on HeLa_microtubules.tif. The test data set, HeLa_microtubules.tif, is a 41 slice z-stack of microtubules stained with a monoclonal anti-α-Tubulin primary antibody and Alexa Fluor 568 secondary antibody to visualize the mitotic spindle assembly of a HeLa cell in metaphase. Imaged with a Plan Apo 60x oil 1.4 NA objective and epi-fluorescence microscopy.

Support Protocol 1

Using ImageJ Ops Matching Feature for Image Inversion

Introductory Paragraph

Image inversion is a common procedure in segmentation workflows but is often computationally expensive. Inversion algorithms often produce pixel outputs by subtracting the input from the maximum value of the pixel type. Such an implementation struggles with signed pixel values, however, as this subtraction operation often causes overflow to occur. For this reason, ImageJ Ops contains two different image inversion Ops. One inversion algorithm optimizes over the set of pixel data types whose entire range can be represented within double precision math. A second algorithm is designed for data types that cannot be accurately represented with double precision math, gaining accuracy at the cost of performance. Given an image whose pixel type is not known beforehand, the ImageJ Ops matcher can intelligently determine the Op most suitable for the given arguments. This allows scripts to easily adapt to different input sets and increases reusability.

Materials:

This protocol has been tested with the following configuration:

- ❏ Windows 10 Operating System
- ❏ Version 2.1.0/1.53c of Fiji (https://imagej.net/Fiji.html#Downloads)

- ❏ Version 0.38.0 of ImageJ Ops (Included in Fiji)
- ❏ The following files are all freely available:
    - ❏ protocol_subprocedure_1.groovy (https://github.com/uw-loci/ScriptingExampleForFLIMJandOps/blob/main/RL_Deconvolution/SP1_Ops_Matching/protocol_subprocedure_1.groovy)
    - ❏ Example dataset: SUM_sp2_gag_still_KIP.tif (https://zenodo.org/record/4642146/files/SUM_sp2_gag_still_KIP.tif)

Protocol Steps:

1. Start Fiji
2. Load the input image into Fiji using “File → Open” or by drag & drop. The example data set SUM_sp2_gag_still_KIP.tif.
3. Load protocol_subprocedure_1.groovy using “File → Open” or by drag & drop. The script opens within the script editor.
4. Run the protocol_subprocedure_1.groovy script from the open script editor.

    Automatically the script will open two windows one that inverts the original unsigned long type image with an Ops function tailored for large data types and one where the image has been converted into a smaller bit data type which is inverted with a different Ops function that is tailored for smaller data types. Both of which are generated using the same call to Ops, and Ops intelligently decides which function to use on the input. Additionally we can inspect which Ops function was called in the Script Editor’s log.

Sample Data:

The sample script was designed to operate on any image but is shown in this protocol running on SUM_sp2_gag_still_KIP.tif which is a summation of three imaging channels. Here the data we used consists of time lapse fluorescence microscopy of HeLa cells being infected by a modified replication deficient HIV-1, NL4-3 strain, fluorescent reporter virus [26]. Upon infection, the reporter virus will integrate its viral genome into the host cell’s genome, transcribe viral mRNA and translate viral proteins. The modified HIV-1_{NL4-3} reporter virus encodes two fluorescent proteins, mCherry and mVenus. The HIV-1 *nef* gene was deleted and replaced with the mCherry fluorescent protein, tracking early viral gene expression. The mVenus fluorescent protein was fused to the *gag* open reading frame, enabling us to observe nascent HIV-1 assembly and budding at the cell periphery and tracking late gene expression. These cells were imaged with a Plan Apo 20x .75 NA air objective and epi fluorescence microscopy.

Support Protocol 2

Headless ImageJ Deconvolution

Introductory Paragraph

So far all the protocols presented require user interaction with the Fiji GUI (via the built-in scripting window running Jython and Groovy scripts) or the Jupyter Notebooks GUI. Herein we show how to call ImageJ completely headless directly from a command line, such that its image processing power can be leveraged by other large computing environments such as high performance computing clusters, where access to a GUI is either undesired or otherwise unavailable.

Materials:

This protocol has been tested with the following configuration:

- ❏ Windows 10, Ubuntu 20.04 LTS (amd64, Desktop), and Ubuntu 18.04 LTS (amd64, Server) operating systems
- ❏ Version 2.1.0/1.53c of Fiji (https://imagej.net/Fiji.html#Downloads)
- ❏ The following files are all freely available:
  - ❏ Decon_richardsonLucyTV_headless.py (https://github.com/uw-loci/ScriptingExampleForFLIMJandOps/blob/main/RL_Deconvolution/SP2_Headless_ImageJ_Deconvolution/Decon_richardsonLucyTV_headless.py)
  - ❏ Example dataset: HeLa_microtubules.tif (https://zenodo.org/record/4642146/files/HeLa_microtubules.tif)

Protocol Steps:

1. Open the Decon_richardsonLucyTV_headless.py file in a text editor
2. Change the path on line 11 to the path for the input file “HeLa_microtubules.tif”
3. Change the path on line 47 to the path for the output file
4. Open a terminal/cmd prompt and navigate to the Fiji install.
5. Run the script by using the appropriate following command and changing the path input to the path for Decon_richardsonLucyTV_headless.py
   a. Windows:
      i. ImageJ-win64.exe --ij2 --headless --console --run "C:/path/to/script.py"
   b. Linux:
      i. ./ImageJ-linux64 --ij2 --headless --run "/path/to/script.py"
   c. MacOS:
      i. Contents/MacOS/ImageJ-macosx --ij2 --headless --run "/path/to/script.py"

   The script will automatically read in the file specified in the input file path, perform deconvolution on it, then save the deconvolved image to the specified output path.

Sample Data:

The Decon_richardsonLucyTV_headless.py script was designed to operate on any z-stack but is shown in this protocol operating on HeLa_microtubules.tif. The test data set, HeLa_microtubules.tif, dataset is a 41 slice z-stack of microtubules stained with a monoclonal anti-α-Tubulin primary antibody and Alexa Fluor 568 secondary antibody to visualize the mitotic spindle assembly of a HeLa cell in metaphase. Imaged with a Plan Apo 60x 1.4 NA oil objective and epi fluorescence microscopy.

Commentary

Background Information

ImageJ offers to customize image analysis workflows through multiple approaches, notably via its scripting framework, which enables users to code processing steps in whichever programming language is most comfortable for them; options include Python, Jython, JavaScript, Ruby, Clojure, Groovy, R, and ImageJ's own macro language, among others [11,2]. Scripting enables scientists to tailor their analysis to the parameters of their experiments, while providing reusable building blocks accessible by the community via ImageJ's update site mechanism [4,5]. All protocols demonstrated in this paper make use of ImageJ scripts and/or plugins in some form.

ImageJ's structured design for plugins, together with its strict separation of graphical elements from algorithmic functionality, enables ImageJ commands and scripts to be used in a variety of contexts besides only the ImageJ user interface [2,4,5]. They can be invoked from other SciJava-compatible applications including KNIME Analytics Platform, CellProfiler, OMERO, and others, as well as from user scripts, including executing in headless mode from the command line, without any graphical user interface [7,12,27,13,28]. This is useful in several scenarios, including: for batch analysis across large quantities of data; when combining ImageJ functionality with other systems via standard interprocess interoperability approaches (files and/or pipes); for use within modules of container-based workflow systems; and for distributed execution of analysis pipelines on server clusters [10,29,30]. See Support Protocol 2 for an example of invoking ImageJ headless from the command line.

To further expand ImageJ's capabilities, it has been extended with ImageJ Ops which is an extensible framework for implementing algorithm plugins, paired with a collection of built-in plugins for common image analysis tasks [2]. The Ops framework enables programmers to create multiple versions of an op targeting different specialized inputs, e.g. convolution ops optimized for different kernel sizes. These ops are typically invoked from user scripts specifying the desired algorithm at a conceptual level (e.g. "convolve"), leaving selection of the most appropriate plugin to the framework, which determines the best match situationally based on the given inputs. This approach transparently realizes the extensible use of specialized code,

without the need for explicit conditional case logic in either user scripts or within the op implementations themselves. In this way, software developers can improve performance of routines by writing more specialized plugin implementations as appropriate and extend the reach of ops to cover new scenarios such as large images, various image storage mechanisms, or new paradigms such as image data accessed from remote databases (*i.e.* cloud computing). To assist the community in tapping into the power of ImageJ Ops, this manuscript highlights its use as part of Support Protocol 1.

ImageJ is grounded in the Java programming language and ecosystem [3]. However, in many cases, scientists benefit from combining ImageJ-based tools with other software ecosystems [4,5]. One very powerful ecosystem used in cross-domain scientific inquiry is the PyData software stack, written in the Python programming language, including NumPy, SciPy, scikit-image, and scikit-learn, among other libraries [31–34]. Another mature ecosystem for working with scientific images accessible from Python is the C++-based Insight Toolkit (ITK) popular in the medical imaging community [35]. To realize a more seamless blending of ImageJ across these and other technology suites, we have created PyImageJ, a software layer implemented in Python that facilitates the use of ImageJ from a Python environment. It contains logic for translating between Python and ImageJ data structures, enabling interchangeable use of NumPy arrays and ImageJ datasets, and image processing routines written for either environment to be combined across language boundaries. To display the power and flexibility of PyImageJ, we highlight it in Basic Protocol 1.

This cross programming language and ecosystem even enables using scientific notebooks which are a popular paradigm for encapsulating the steps of data analysis protocols and workflows. One notebook software in common use in the data sciences community is Jupyter Notebook [14], which makes it easy to showcase workflows in a visual, interactive, and reproducible way, by writing snippets of Groovy or other code in so-called notebook cells, which when executed produce numerical and/or visual output. Notebooks allow for both experimentation and data mining—by executing and revising cells out of order to explore one's data—as well as communication of completed workflows with others, by embedding the computation results into the final notebook, which can be made readily accessible online from a web browser [15]. In Basic Protocol 1 and Alternate Protocol 1, we show how to use ImageJ as part of a Jupyter notebook.

The need for improved, accessible, extensible, and open-source image processing has been primarily driven by the explosion of optical microscopy methods in the last 25 years. One such method, which is powerful but requires substantial processing to analyze the collected data, is Fluorescence Lifetime Imaging Microscopy (FLIM)[36–38]. Unfortunately, most current FLIM analysis frameworks are highly dependent on the underlying collection hardware and the associated third party proprietary algorithm from the same manufacturer for data processing [39]. Due to the proprietary nature of the algorithm used in such commercial software, it is opaque and non-extendable meaning that users cannot build further analysis into the software nor experiment with the processing pipeline for artifact correction etc. There is a strong need for FLIM microscopy methods to have not only a processing framework that functions across

multiple hardware acquisition platforms but is also extensible and open-source. Given the importance of this method, we present, as Basic Protocol 1, an open-source protocol for FLIM image processing independent of the underlying acquisition software that is extensible with the suite of image processing tools available in ImageJ.

Critical Parameters

Protocol 1

This protocol is centered around FLIM data and has been designed to calculate all basic critical parameters from the data. Specifically of note is the time resolution since a mismatch between what is used and the underlying data leads to incorrect lifetime fitting.

Alternate Protocol 1

There is only one critical parameter that is user tweakable in the main fitting methods. Specifically which range of time bins to analyze. This alters the underlying data that the fitting method uses. Furthermore it permits removal of data captured before a fluorescence event and after it is complete, thereby reducing the amount of data processed which improves the speed and reduces the amount of noise going into the processing. For further data reduction, there are two more parameters that are alterable. Specifically for the region of interest (ROI), the bounds of the ROI mask to be analyzed are defined in image pixels by the coordinates within the image. For binning, the kernel used for binning is alterable to provide differences in weighting and size.

Protocol 2

Within this protocol, there are multiple experiment/microscope derived inputs which are data set collection dependent. These parameters are critical for the correct operation of image deconvolution. Going through them, there is NumericalAperture which is the NA of the objective used to image the data set. There is Wavelength which is the excitation wavelength used in nm. There is RiImmersion which is the refractive index of the immersion medium generally this is oil (~1.5), water (~1.3), or air (~1.0). Similarly, RiSample is the estimate of the refractive index of the sample. For biological purposes this is estimated as the average between the cover slip (normally crown glass at ~1.5) and the sample (since most biology is primarily water, ~1.3). Then within a single field of view the xySpacing is the XY pixel spacing in nm and assumes equal pixel spacing in X and Y dimensions. Then there is zSpacing which is the distance in nm between each Z-pane in the data set. . Finally there is one parameter that affects the algorithm and is independent of the data collection; the NumIterations which is the number of iterations of RichardsonLucyTV deconvolution to run, the number of iterations specified determines the bulk of how long the protocol takes the run.

Support Protocol 1

Users should take note of the data types of the arguments provided during a matching call. To maximize efficiency, these types should be compared to those of each Op that is a potential match.

Support Protocol 2

This protocol is an extension of Protocol 2, so all the critical parameters from Protocol 2 are applicable here as well. Additionally, this protocol requires two file paths “/path/to/image.tif” and "/path/to/output_image.tif". Naming within the file path has to be done carefully since the Python interpreter does not recognize spaces nor overarching drive directory such as “D:/”.

Troubleshooting

Protocol 1

The primary issues that arise from this protocol operating on the example data stem from incorrectly setting up the environment. Secondarily errors will be thrown if the ImageJ initialization code block is re-run multiple times since an instance of ImageJ is already running in the environment.

Additionally, if this protocol is run on a different data set than the example data, some modification of data read in may be necessary to account for differences in how the file formats store the collected data.

Alternate Protocol 1

Due to the nature of the extension, most issues arise from setting up the environment. Particularly importing the FLIMJ Ops in the notebook can have problems with the classpath for dependencies. If this causes errors, there is a code block immediately below the Dependencies block that can be uncommented and run to fix this issue.

Additionally, if this protocol is run on a different data set than the example data, some modification of data read in and splitting may be necessary to account for differences in how the file formats store the collected data.

Protocol 2

The main issues that can arise in this protocol are all centered around mismatches between the critical parameters for this and the data on which it is run. As such, if you are running this protocol on data other than the example data set, make sure that the critical parameters are updated to match the data.

Support Protocol 1

Due to the strong typing of the Java language, most Ops matching errors are due to a mismatch between the argument types and the parameter types of the Op(s) of interest. Ensure that all arguments provided in the Op call are assignable to the parameter types of the Op.

Another set of issues can arise when attempting to reuse an Op on a different set of arguments than those used in the matching request. The matching framework uses the arguments it is given to return the optimal Op for *those arguments*; other sets of arguments may not be accepted by the returned Op. To operate on arguments of different types, it is advised to either create a matching request on the greatest common supertype or to create two separate matching requests.

Support Protocol 2

The primary issues that arise within this protocol are file path naming issues. In particular the command line/terminal will throw errors on spaces in the path names. Additionally the overarching directory i.e. “C:\” cannot be used within the scripts input and output image file paths since the parser errors on the character “:”. Additionally, if run on data other than the example data set, the script is subject to the same data to critical parameter mismatch as described in Protocol 2 Troubleshooting.

Understanding Results

General

Overall, all protocols presented are designed to be clear examples of how readily the image processing power of ImageJ can be integrated into repeatable workflows and data processing for biological applications.

Protocol 1

This protocol exports lifetime fitted FLIM images. As such the core element to note is the ability to visualize the lifetime components via the three component images, offset, amplitude, and lifetime estimate (See Figure 5.1). These images can provide insights into cellular micro-environments with quantitative sensing abilities.

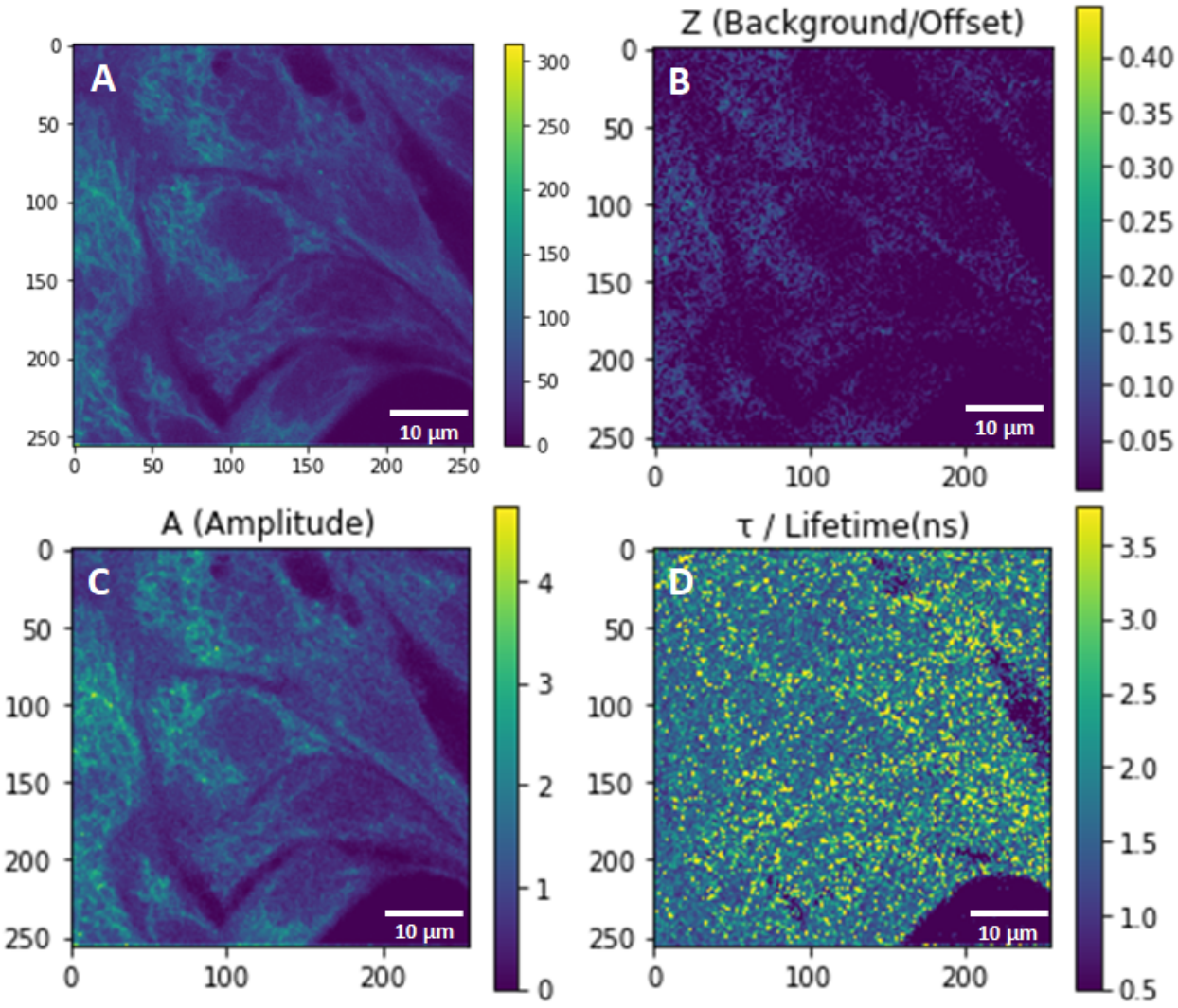

Figure 5.1

In Basic Protocol 1: Using PyImageJ for FLIM Data Processing, (A) the summation of all collected photons before processing, Levenberg-Marquardt Fitted Data of NADH lifetimes of unstained epithelial cells from human mammary gland tissue with fibrocystic disease (B) offset, (C) amplitude, and (D) estimated lifetime. NAD(P) auto-fluorescence signals were collected with 740nm excitation and 460/80 emission. The hardware used was a Nikon Apo 40x water immersion objective with a 1.25 NA and a Becker & Hickl Single Photon Counting system.

Alternate Protocol 1

There are five lifetime fitting methods and two common data reduction methods presented in this protocol. At their core, all lifetime fitting methods are attempting to take advantage of the fluorescence photons time of flight to estimate the underlying physiological parameters and use

those to generate contrast for images (See Figure 5.2). The two common data reduction methods are used to allow for processing of larger data sets.

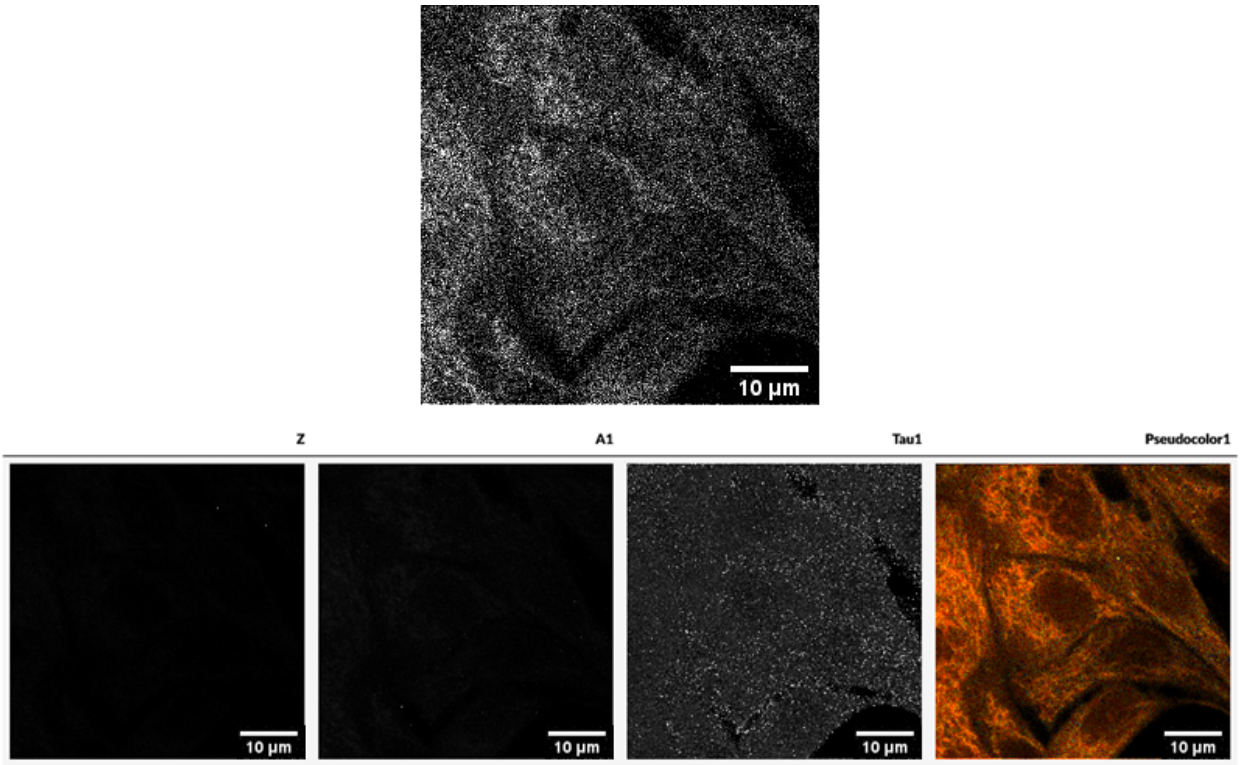

Figure 5.2

In Alternate Protocol 1: Groovy FLIMJ in Jupyter Notebooks, the (Top) a time bin from the raw FLIM intensity data and the (Bottom) Levenberg-Marquardt Fitted pseudo colored NADH lifetimes of unstained epithelial cells from human mammary gland tissue with fibrocystic disease. NAD(P) auto-fluorescence signals were collected with 740 nm excitation and 460/80 emission. The hardware used was a Nikon Apo 40x water immersion objective with a 1.25 NA and a Becker & Hickl Single Photon Counting system.

Protocol 2

The resultant image should be clearer than the input image (See Figure 5.3) since the image deconvolution process is designed to remove blur caused by the inherent point spread function (PSF) of the imaging system as characterized by the experimental components that primarily determine the PSF. This provides image quality improvement at minimal cost to users time and experimental overhead.

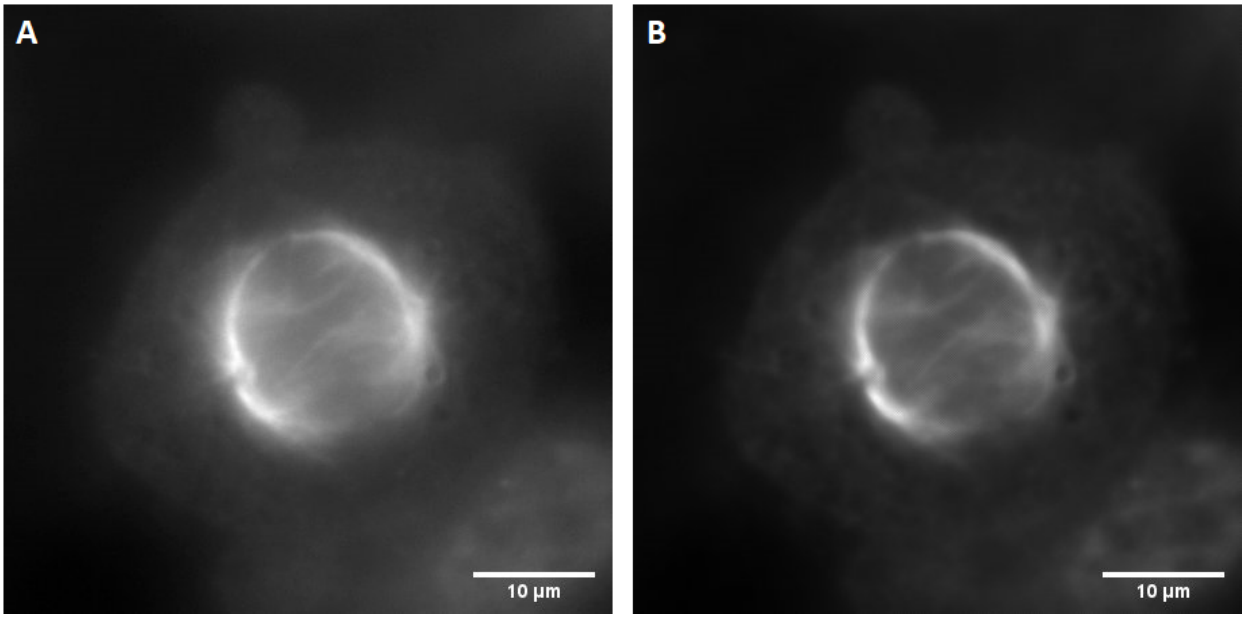

Figure 5.3

In Basic Protocol 2: Using ImageJ Ops for Deconvolution and Support Protocol 1: Headless ImageJ Deconvolution, the difference in clarity between (A) raw data and (B) deconvolved data of a z-stack of microtubules stained with a monoclonal anti-α-Tubulin primary antibody and Alexa Fluor 568 secondary antibody to visualize the mitotic spindle assembly of a HeLa cell in metaphase, imaged with a Plan Apo 60x oil objective and epi fluorescence.

Support Protocol 1

The Ops returned by each inversion Op request are of particular importance, namely due to the fact that different Ops are returned for each request (See Figure 5.4). In light of the different argument types, the juxtaposition of these two returns highlights the ease of optimization made possible through the matching framework. This feature is present throughout the Ops library where useful rather than restricted to the inversion function.

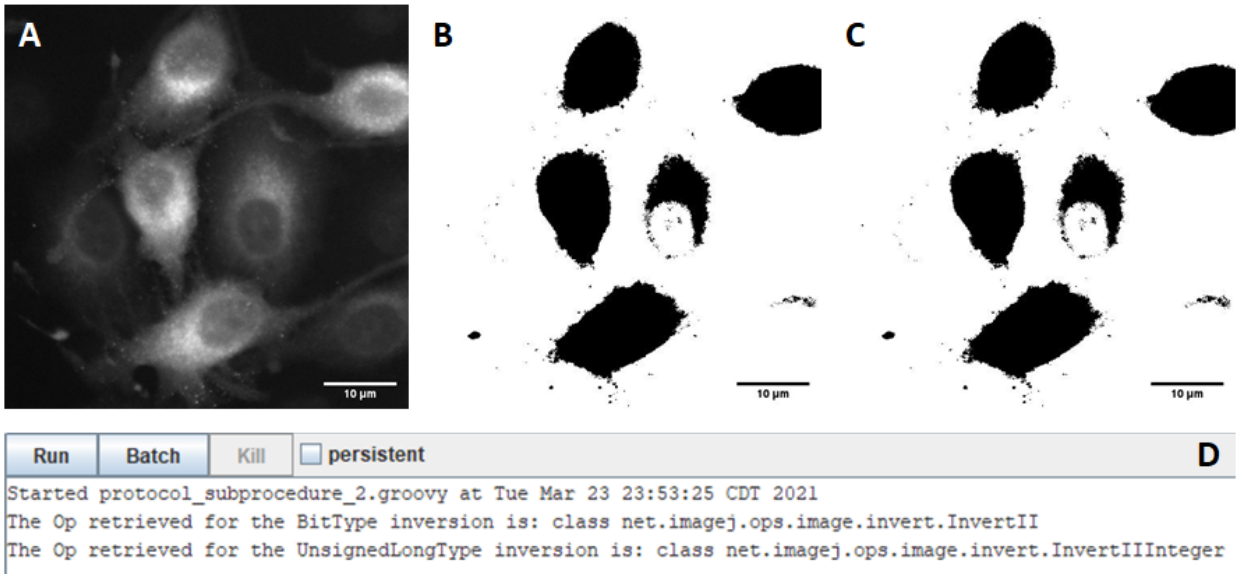

Figure 5.4

In Support Protocol 1: Using ImageJ Ops Matching Feature for Image Inversion, (A) the original image, (B) inverted unsigned long type image, and (C) inverted bit type image, with (D) the different Ops used enumerated. The sample imaged is a HeLa cell being infected by a vesicular stomatitis virus G (VSV-G)-pseudotyped single-round fluorescent HIV-1_{NL4-3} virus. Upon infection, the virus produces mVenus-tagged HIV Gag proteins and free mCherry. These cells were imaged with a Plan Apo 20x air objective and epi fluorescence.

Support Protocol 2

The same as in Protocol 2, the resultant image should be clearer than the input image (See Figure 5.3), the core element of note is that it was run in a completely headless manner. Meaning no interaction with the Fiji GUI was necessary.

Time Considerations

Protocol 1

Setting up the environment to run this protocol takes about fifteen minutes, but once set up doesn't need to be done again. Stepping through this protocol is straightforward and takes around five minutes. The amount of time needed is dependent on the size of the dataset used.

Alternate Protocol 1

If the environment hasn't already been set up for Protocol 1, then setting up the environment *de novo* to run this protocol takes about fifteen minutes. Processing the example dataset takes

about ten minutes to step through each component in the Jupyter Notebook interface. When running this protocol on other datasets the time required will scale with the size of the underlying data set.

Protocol 2

Processing of the example dataset takes up to five minutes depending on the computational power of the hardware and the number of iterations used in the protocol. When running this protocol on other datasets the time required will scale with the size of the image and the number of iterations of deconvolution used.

Support Protocol 1

Processing of the example dataset takes only a few seconds (image conversion and then two inversions) in Fiji. When running this protocol on other datasets the time required will scale with the size of the image, which only makes it more effective as an example displaying the speed-ups that can be gained from using Ops matching feature.

Support Protocol 2

Processing of the example dataset with this protocol takes just as long in headless mode as it does with the Fiji interface and the time will scale with the size of the data set and the number of iterations of deconvolution used. But headless ImageJ allows for cloud computing meaning that a user can farm out processing of large data sets to more powerful computers and servers than their local machine, thereby decreasing the time it takes to process the data set.

Future Directions

With the readily extensible framework that ImageJ provides, new and improved image processing methods and protocols are constantly being added by users, and shared via ImageJ's update site mechanism, as well as in public repositories in source code and notebook forms. Furthermore, ImageJ has already been extended to be accessible from many scripting languages and environments and will continue to expand and support more languages used by scientists such as R and MATLAB. We are particularly excited to continue improving the PyImageJ library, such that users may seamlessly utilize Python-based routines from ImageJ scripts running within the ImageJ user interface, as well as further developing ImageJ's web-oriented capabilities, enabling ImageJ functionality to be combined with JavaScript-based tools such as ImJoy [28] expanding its utility to more platforms such as mobile devices. We also look forward to ImageJ continuing to grow in its support for larger and more complex scientific image datasets, driven by the underlying ImgLib2 [40] and BigDataViewer [41] libraries.

This displays some of the main functionalities and benefits of using ImageJ/FIJI for image processing and provides some simple scripts for new users to build off of[5]. Thereby enabling new users to utilize this open source platform for their own purposes, rather than being reliant on MATLAB or collaborators for their image processing [1,8]. Additionally enabling them to access a plethora of useful processing methods they may not even have been aware of.

Chapter 5 References

1. MATLAB [Internet]. The Mathworks, Inc.; 2021. Available from: https://www.mathworks.com/products/matlab.html
2. Rueden CT, Schindelin J, Hiner MC, DeZonia BE, Walter AE, Arena ET, et al. ImageJ2: ImageJ for the next generation of scientific image data. BMC Bioinformatics. 2017 Nov 29;18(1):529.
3. Schneider CA, Rasband WS, Eliceiri KW. NIH Image to ImageJ: 25 years of image analysis. Nat Methods. 2012 Jul;9(7):671–5.
4. Schroeder AB, Dobson ETA, Rueden CT, Tomancak P, Jug F, Eliceiri KW. The ImageJ ecosystem: Open-source software for image visualization, processing, and analysis. Protein Sci. 2021;30(1):234–49.
5. Schindelin J, Rueden CT, Hiner MC, Eliceiri KW. The ImageJ ecosystem: An open platform for biomedical image analysis. Mol Reprod Dev. 2015;82(7–8):518–29.
6. PyImageJ: Python wrapper for ImageJ [Internet]. ImageJ; 2021 [cited 2021 Nov 22]. Available from: https://github.com/imagej/pyimagej
7. Dietz C, Rueden CT, Helfrich S, Dobson ETA, Horn M, Eglinger J, et al. Integration of the ImageJ Ecosystem in KNIME Analytics Platform. Front Comput Sci [Internet]. 2020 [cited 2021 Apr 1];2. Available from: https://www.frontiersin.org/articles/10.3389/fcomp.2020.00008/full?report=reader
8. Hiner MC, Rueden CT, Eliceiri KW. ImageJ-MATLAB: a bidirectional framework for scientific image analysis interoperability. Bioinformatics. 2017 Feb 15;33(4):629–30.
9. Gao D, Barber PR, Chacko JV, Sagar MAK, Rueden CT, Grislis AR, et al. FLIMJ: An open-source ImageJ toolkit for fluorescence lifetime image data analysis. PLOS ONE. 2020 Dec 30;15(12):e0238327.
10. Krumnikl M, Bainar P, Klímová J, Kožusznik J, Moravec P, Svatoň V, et al. SciJava Interface for Parallel Execution in the ImageJ Ecosystem. In: Saeed K, Homenda W, editors. Computer Information Systems and Industrial Management. Cham: Springer International Publishing; 2018. p. 288–99. (Lecture Notes in Computer Science).
11. Schindelin J, Arganda-Carreras I, Frise E, Kaynig V, Longair M, Pietzsch T, et al. Fiji: an open-source platform for biological-image analysis. Nat Methods. 2012 Jul;9(7):676–82.
12. Kamentsky L, Jones TR, Fraser A, Bray MA, Logan DJ, Madden KL, et al. Improved structure, function and compatibility for CellProfiler: modular high-throughput image analysis software. Bioinformatics. 2011 Apr 15;27(8):1179–80.
13. Möller B, Glaß M, Misiak D, Posch S. MiToBo - A Toolbox for Image Processing and Analysis. J Open Res Softw. 2016 Apr 28;4(1):e17.
14. Kluyver T, Ragan-Kelley B, Pérez F, Granger BE, Bussonnier M, Frederic J, et al. Jupyter Notebooks-a publishing format for reproducible computational workflows. Vol. 2016. 2016.
15. Perkel JM. Why Jupyter is data scientists' computational notebook of choice. Nature. 2018 Nov 1;563(7732):145–7.
16. Schermelleh L, Ferrand A, Huser T, Eggeling C, Sauer M, Biehlmaier O, et al.

Super-resolution microscopy demystified. Nat Cell Biol. 2019 Jan;21(1):72–84.
17. Giepmans BNG, Adams SR, Ellisman MH, Tsien RY. The Fluorescent Toolbox for Assessing Protein Location and Function. Science. 2006 Apr 14;312(5771):217–24.
18. Blake DJ, Weir A, Newey SE, Davies KE. Function and Genetics of Dystrophin and Dystrophin-Related Proteins in Muscle. Physiol Rev. 2002 Apr 1;82(2):291–329.
19. Chinen AB, Guan CM, Ferrer JR, Barnaby SN, Merkel TJ, Mirkin CA. Nanoparticle Probes for the Detection of Cancer Biomarkers, Cells, and Tissues by Fluorescence. Chem Rev. 2015 Oct 14;115(19):10530–74.
20. Lamm MH, Ke PC. Cell Trafficking of Carbon Nanotubes Based on Fluorescence Detection. In: Balasubramanian K, Burghard M, editors. Carbon Nanotubes: Methods and Protocols [Internet]. Totowa, NJ: Humana Press; 2010 [cited 2021 Jul 14]. p. 135–51. (Methods in Molecular Biology). Available from: https://doi.org/10.1007/978-1-60761-579-8_12
21. Lagendijk EL, Validov S, Lamers GEM, De Weert S, Bloemberg GV. Genetic tools for tagging Gram-negative bacteria with mCherry for visualization in vitro and in natural habitats, biofilm and pathogenicity studies. FEMS Microbiol Lett. 2010 Apr 1;305(1):81–90.
22. Gahm Th, Reinhardt ER, Witte S. Analysis of the wall permeability of blood vessels in the rat mesentery. Res Exp Med (Berl). 1984 Mar 1;184(1):1–15.
23. Kalinina S, Breymayer J, Schäfer P, Calzia E, Shcheslavskiy V, Becker W, et al. Correlative NAD(P)H-FLIM and oxygen sensing-PLIM for metabolic mapping. J Biophotonics. 2016;9(8):800–11.
24. Ryder AG, Power S, Glynn TJ, Morrison JJ. Time-domain measurement of fluorescence lifetime variation with pH. In: Biomarkers and Biological Spectral Imaging [Internet]. International Society for Optics and Photonics; 2001 [cited 2021 Jul 14]. p. 102–9. Available from: https://www.spiedigitallibrary.org/conference-proceedings-of-spie/4259/0000/Time-domain-measurement-of-fluorescence-lifetime-variation-with-pH/10.1117/12.432487.short
25. Lebakken CS, Kang HC, Vogel KW. A Fluorescence Lifetime–Based Binding Assay to Characterize Kinase Inhibitors. J Biomol Screen. 2007 Sep 1;12(6):828–41.
26. Evans EL, Becker JT, Fricke SL, Patel K, Sherer NM. HIV-1 Vif's Capacity To Manipulate the Cell Cycle Is Species Specific. J Virol. 2018 Apr 1;92(7):e02102-17.
27. Allan C, Burel JM, Moore J, Blackburn C, Linkert M, Loynton S, et al. OMERO: flexible, model-driven data management for experimental biology. Nat Methods. 2012 Mar;9(3):245–53.
28. Ouyang W, Mueller F, Hjelmare M, Lundberg E, Zimmer C. ImJoy: an open-source computational platform for the deep learning era. Nat Methods. 2019 Dec;16(12):1199–200.
29. apeer [Internet]. apeer. [cited 2021 Mar 27]. Available from: https://www.apeer.com/home
30. Rubens U, Mormont R, Paavolainen L, Bäcker V, Pavie B, Scholz LA, et al. BIAFLOWS: A Collaborative Framework to Reproducibly Deploy and Benchmark Bioimage Analysis Workflows. Patterns [Internet]. 2020 Jun 12 [cited 2021 Mar 27];1(3). Available from: https://www.cell.com/patterns/abstract/S2666-3899(20)30045-3
31. Harris CR, Millman KJ, van der Walt SJ, Gommers R, Virtanen P, Cournapeau D, et al. Array programming with NumPy. Nature. 2020 Sep;585(7825):357–62.
32. Pedregosa F, Varoquaux G, Gramfort A, Michel V, Thirion B, Grisel O, et al. Scikit-learn: Machine Learning in Python. J Mach Learn Res [Internet]. 2011 Oct 12 [cited 2021 Mar 31]; Available from: https://hal.inria.fr/hal-00650905
33. van der Walt S, Schönberger JL, Nunez-Iglesias J, Boulogne F, Warner JD, Yager N, et al. scikit-image: image processing in Python. PeerJ. 2014 Jun 19;2:e453.
34. Virtanen P, Gommers R, Oliphant TE, Haberland M, Reddy T, Cournapeau D, et al. SciPy 1.0: fundamental algorithms for scientific computing in Python. Nat Methods. 2020

Mar;17(3):261–72.
35. Yoo TS, Ackerman MJ, Lorensen WE, Schroeder W, Chalana V, Aylward S, et al. Engineering and Algorithm Design for an Image Processing API: A Technical Report on ITK - the Insight Toolkit. Med Meets Virtual Real 0210. 2002;586–92.
36. Lakner PH, Monaghan MG, Möller Y, Olayioye MA, Schenke-Layland K. Applying phasor approach analysis of multiphoton FLIM measurements to probe the metabolic activity of three-dimensional in vitro cell culture models. Sci Rep. 2017 Feb 13;7(1):42730.
37. O'Connor D. Time-correlated single photon counting. Academic Press; 2012. 299 p.
38. Verveer PJ, Hanley QS. Chapter 2 Frequency domain FLIM theory, instrumentation, and data analysis. In: Laboratory Techniques in Biochemistry and Molecular Biology [Internet]. Elsevier; 2009 [cited 2021 Mar 27]. p. 59–94. (Fret and Flim Techniques; vol. 33). Available from: https://www.sciencedirect.com/science/article/pii/S0075753508000028
39. Becker W. Advanced Time-Correlated Single Photon Counting Techniques. Springer Science & Business Media; 2005. 414 p.
40. Pietzsch T, Preibisch S, Tomančák P, Saalfeld S. ImgLib2—generic image processing in Java. Bioinformatics. 2012 Nov 15;28(22):3009–11.
41. Pietzsch T, Saalfeld S, Preibisch S, Tomancak P. BigDataViewer: visualization and processing for large image data sets. Nat Methods. 2015 Jun;12(6):481–3.

Chapter 6: Future Direction

My thesis work focused on the development and streamlining of tools for computational microscopy and making those tools more accessible to future users. Both the SSFC and SETI tools are currently very much stand-alone applications written in a non-open source programming framework, but the underlying algorithms and scripts which are open-source for these two projects are readily generalizable to other microscopes that operate on similar premises. As such this presents an opportunity for them to be translated into μManager or OpenScan so they can be more readily used in other applications [1–3]. This also opens up the possibility of run-time processing for these methods. With the diversity of computational microscopy methods available, integrating more fundamental methods into standardized open-source software packages with a multitude of supportive users can provide others with a starting point to build off of and develop even more innovative computational methodologies [4,5]. Furthermore as controllable optical elements get more and more integrated into systems, we can utilize these steering code frameworks to programmatically capture multiple images of the same field of view with different methodologies either for the sake of co-localization experiments or direct comparison to each other. Specifically optical elements such as a digital light projector can be utilized for most variants of structured illumination, ranging from the projection of Hildebrand matrices for super resolution to simple bar patterns for background rejection. This capacity will continually increase as more elements become computer controllable.

The SSFC approach uses the intrinsically unused space of the detection camera in multipoint confocal setups [6]. This increase in information density could be further leveraged than just the color separation I present, polarization could potentially be split in a similar fashion for co-localization and co-temporal experiments. A similar approach can be implemented on other hardware than what is presented. With more development and commercialization a simple retrofit module could add these options to many currently existent multipoint confocal microscopes. To fully utilize these capabilities a functional image processing algorithm is needed for image reconstruction, such as the one I present [7,8]. While this algorithm is open-source and forms a good baseline for this reconstruction problem, there are more improvements and automation that can be added to it. The algorithm I present is entirely centered around a priori knowledge of the distribution of information across the detection camera, and operates on a pixel splitting basis. Alternative approaches have the potential to perform even better. An approach commonly utilized in spectroscopy for small numbers of unknown spectra is a cytofluorogram which operates on non-negative matrix factorization spectral unmixing [9–12]. This approach would theoretically be better at separating fluorophores that have partially overlapping emission spectra, which the pixel splitting approach is not designed to handle. While these are algorithmic approaches to reconstructing the image, there is also potential for machine learning unmixing, since the sequential sub-images captured, can be viewed as being a 3D image cube, with parts of the whole image striped across it with a diagonal slant into the z-axis. Machine learning has the potential to better capture the partially

filled pixels on the edges of the diagonal stripe [13–15]. Additionally there are deep learning approaches for nonlinear unmixing in hyperspectral imaging which have shown the potential to be even better than the linear unmixing dependent on the underlying experiment [16,17]. All of these methods can be used to significantly improve parts of the pixel splitting algorithm I present, but require further development and tuning towards the unique underlying approach to maximize the information density available from the detection camera. Additionally if these algorithms get translated into being distributable plugins for ImageJ or OpenScan, their implementation for this specific project and many more can be streamlined into the acquisition software, thereby potentially even enabling a real-time view of the sample, and decreasing the time between data acquisition and analysis while using a processing intensive imaging method [1,4,18].

The SETI project can also benefit from this form of integration with a framework such as Micro-Manager/OpenScan [1]. While this work generated a computational algorithm that can reconstruct background rejected images from two to six patterned sub-images, there are many more regular corrections and speedups that can be included in the system such as an automated flat field correction [19,20]. The framework presented is capable of handling the post-processing image reconstruction for most forms of structured illumination for background rejection [21,22]. It would benefit from being translated from open-source MATLAB code into more readily accessible languages such as Python or Java [23]. Currently it is functionalized such that all the methods can be accessed by ImageJ through the MATLAB-ImageJ bridge [4,5,24–26]. On the sample side of the system, a significant amount of work needs to be done to develop a hard resin or epoxy sample preservation method that does not alter the underlying morphological features [27–31]. A resin with these properties would be able to withstand the milling process and make this system incredibly powerful, since it has the capability to scan large tissues without losing signal due to getting too deep into the sample [32,33]. Additionally the milling provides a unique opportunity for chip capture and secondary analysis with approaches such as atomic mass spectrometry which requires the sample to be ground very fine before it can be used [34,35]. Additionally, more work can be done to redesign the layout of the system to reduce vibration, improve positional accuracy, and make it more portable than its current version.

The RT-FLIM project inherently shows the benefits that modality integration can provide. Through algorithm analysis and testing, RLD and phasor approaches were selected for initial integration into OpenScan. They met the criteria for being viable real time analysis methods, since they were both fast, accurate, and in the case of phasor able to visually quantify information about lifetime clusters [36–41]. By integrating both methods into OpenScan users can use whichever method they are most comfortable with and makes this tool more well-rounded and appealing to more research groups [1]. Furthermore this provides access to the direct datastream coming from a system which currently assists researchers by acting as an early warning system/data quality check, but has significant potential for future development to enable “smart” microscopes which are able through on the fly image analysis tell whether the sample has moved and correct for that, or provide real-time segmentation to researchers monitoring the experiment as assistance for data quality control [42–44]. Which comes back to

the benefits of modality and method integration, since as more estimation approaches are developed, they can be added and can build off of the functions and methods already integrated, therein not only saving time in the development of them, but also being built on tested and debugged methods which increases stability [45]. As the tool stands, it is readily available in OpenScan which adds quality control measures earlier into the imaging pipeline for FLIM [1,46].

To ensure better and more accessible data being collected, imaging modalities require matched image processing. And many tools exist for this purpose, notably ImageJ/FIJI, R, and MATLAB [4,24,25]. Through the macro writing system in ImageJ/FIJI, it is fairly easy to generate repeatable image analysis routines without the need of a scripting knowledge base [18,47,48]. Unfortunately, without a scripting knowledge base it is difficult to utilize the full power behind all of these tools. Therefore, to make access to scripting easier, the image processing paper was written. This highlights the readily extensible framework that ImageJ provides, and showcases a breadth of general use cases that can be built off of. Furthermore, these cases show how ImageJ has already been extended to be accessible from many scripting languages and environments such as R and MATLAB. Python is increasingly becoming a common scientific scripting language, as such the PyImageJ library was written and is being expanded such that users may seamlessly utilize Python-based routines from ImageJ scripts. This enables ImageJ functionality to be combined with JavaScript-based tools such as ImJoy expanding its utility to more platforms such as mobile devices [49]. Through the integration of ImgLib2 and BigDataViewer libraries ImageJ is able to support larger and more complex scientific image datasets [50,51].

The further development and increased accessibility of core methodologies presents space for interactions between machine learning and image reconstruction algorithms, since the reconstruction processing algorithms produce a lot of information on each reconstructed image that is not visible in the final image. Machine learning could use this information to refine the reconstructed image, perform quality control/assurance, and potentially even use it for classification [49,52–60]. Similarly, run-time processing of computational microscopy also enables machine learning to be combined with the system’s steering code. The main use cases so far are to classify if any part of the sample is in the field of view before taking an image or to dynamically correct for aberrations in the imaging system [61–63]. This saves data storage space, speeds up imaging, reduces the likelihood of photo-bleaching the sample, and produces higher quality images. But the possible scope of what can be accomplished with machine learning integrated in steering processes is significantly larger, with its capacity for classification and identification, it could be utilized to do highly selective scans which would be useful in fields such as in pathology, only capturing images from regions bearing cancer markers, potentially even generating grade classifications that do not suffer from human interpretability at the time of imaging. Thereby removing the wait period between when a sample is imaged and the pathologist gets around to analyzing it. Finally, as more and more computational power keeps becoming increasingly easier to access, computational microscopy will only become more powerful by being able to run larger algorithms at run-time and handle larger data sets.

Appendix: Collaborations

Before coming to grad school, I was an undergrad doing research in Dr. Izatt's lab at Duke University. Most of my work was on integrating and streamlining the post-processing pipeline for the Swept Source Optical Coherence Tomography (SSOCT) project[64]. Once that was complete it evolved into working on a Heads Up Display to stream SSOCT data in real time to a Google Glass device. I was simultaneously working on designing custom opto-mechanical parts and Solid Works modeling for a long working distance OCT system targeted for usage in pediatric applications [65,66]. This work gave me my first experiences with computational microscopy which I further explored in graduate school.

I started graduate school at Vanderbilt University in Dr. Skala's lab, where my work was focused on the development of computational microscopy methods. Wherein I started with a project building a Fourier ptychography microscope using interfering light-sheets in the ultraviolet (UV) spectrum to image T-Cells. Fourier ptychography is incredibly powerful, due to its capabilities to capture large fields of view at high resolution [67–70]. Upon further refinement this project was changed to a structured illumination microscope with UV illumination.

Simultaneously I was working on a cell classifier I called Atlas Classification with Dr. Skala and Dr. Landman. This classifier was centered around utilizing Bayesian statistics with confusion matrices to iteratively update the priors [71–74]. It operated on comparing cells in an unclassified image to two or more collections of images of a single known cell type. While this project was fascinating and statistically interesting, I was ultimately able to mathematically prove that it did not work with this approach.

During this period Dr. Skala's lab ended up moving from Vanderbilt University to University of Wisconsin - Madison. Once here my collaborations were primarily with Dr. Eliceiri's lab focused on the integration of computation with microscopy. With the SETI and SSFC projects being side projects originally. Through this, it became clear that my interests were significantly more computational than I had originally expected. This led to me transitioning from Dr. Skala's lab to Dr. Eliceiri's.

Appendix: Supplemental Information

Chapter 2 Supplemental Information:

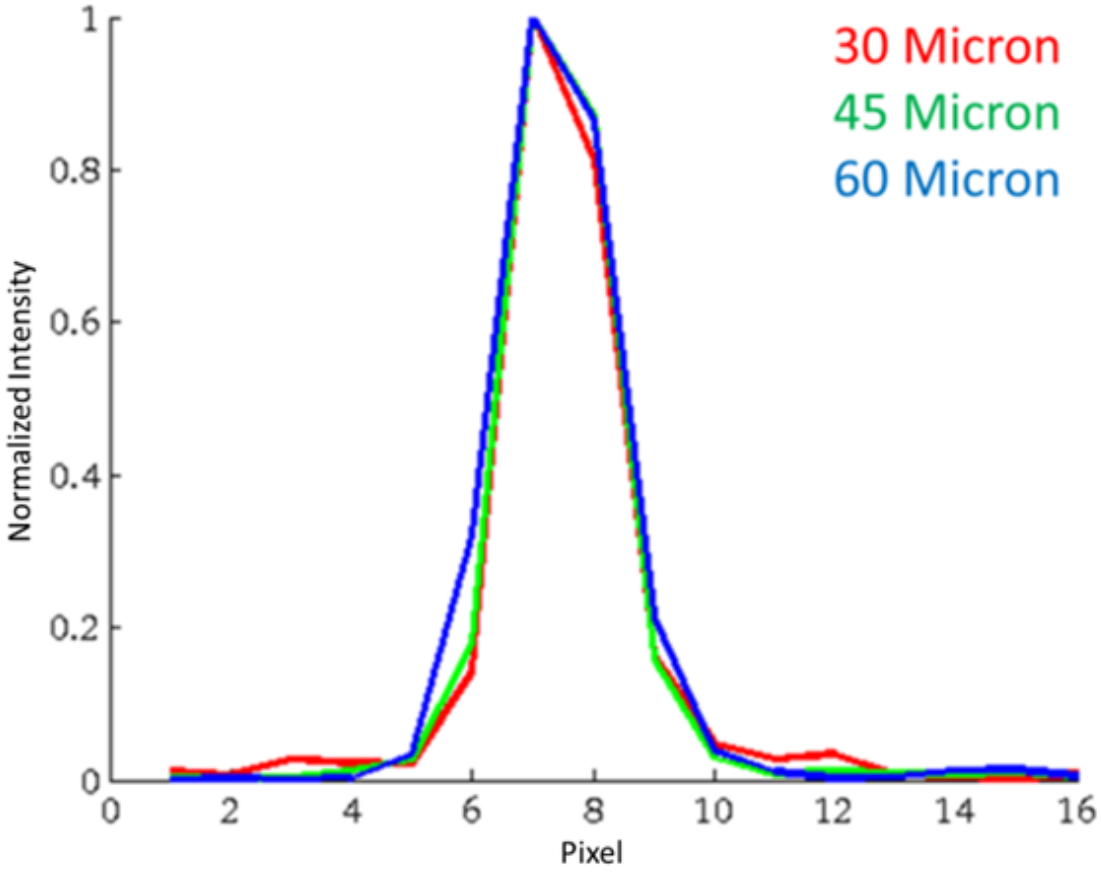

S2.1 Fig. Spectral point spread functions. The point spread functions for different size apertures are measured by shining a laser diode on a diffuser placed in the image plane of the microscope objective.

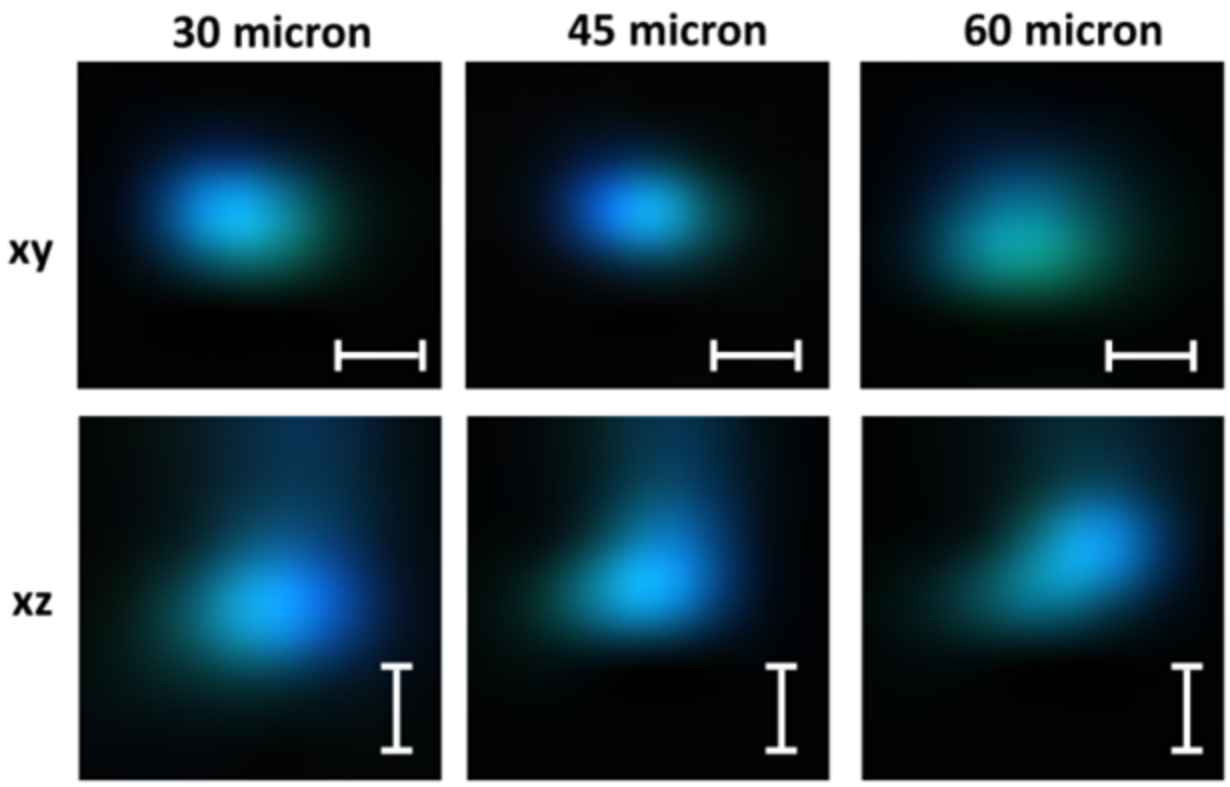

S2.2 Fig. Spatial point spread functions for different pinholes. These images are obtained by imaging 0.2 micron large fluorescent beads with a 60x oil objective (NA 1.4). The size marker indicates 1 micron. In all cases the Point Spread Function extends over only a few camera pixels.

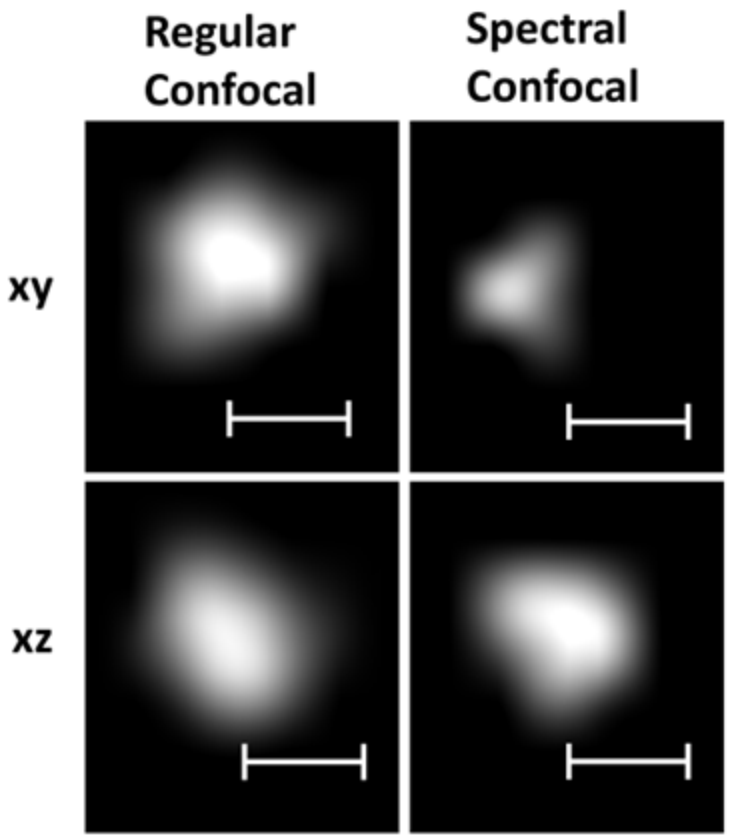

S2.3 Fig. Spatial point spread functions for regular swept field capture and spectral capture. These images are obtained by imaging 0.2 micron large fluorescent beads with a 40x oil objective. The size marker indicates 1 micron. The spectral separation does not negatively impact the point spread function of the instrument.

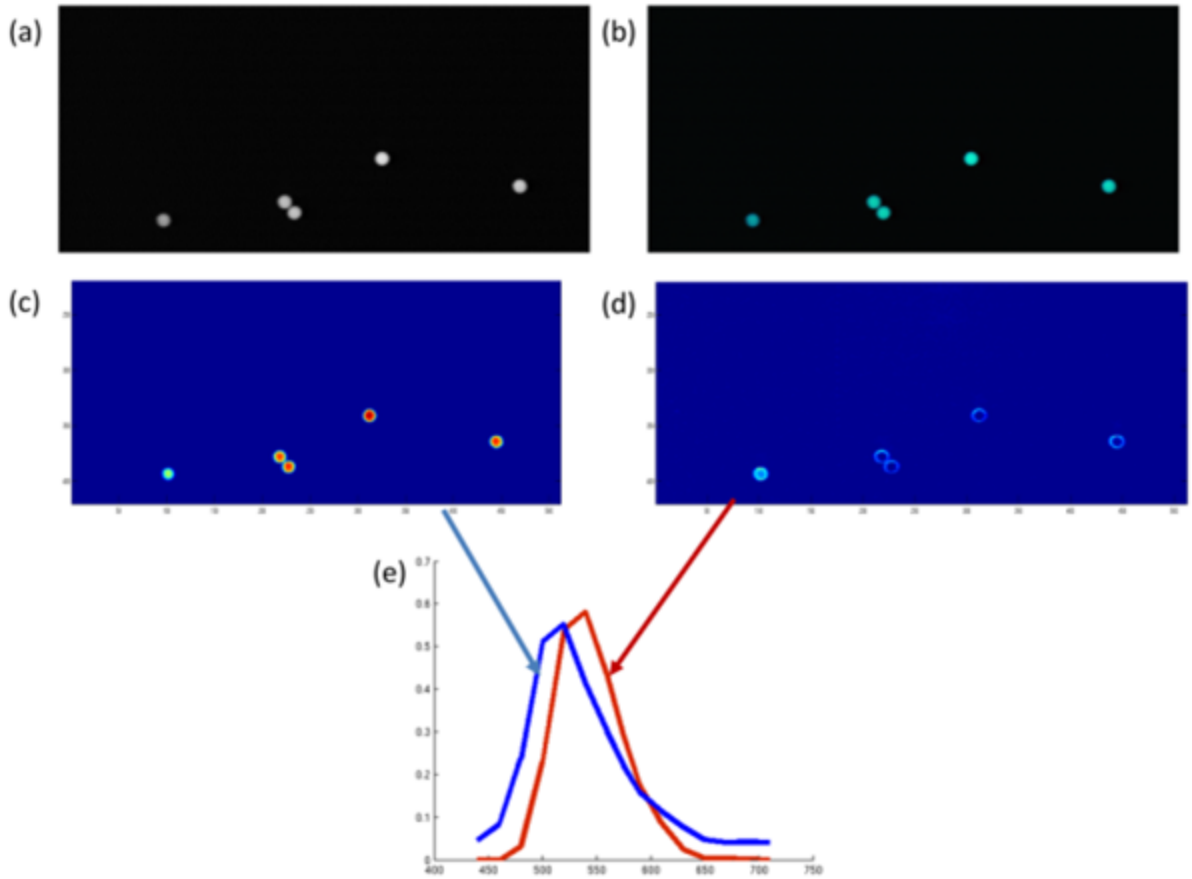

S2.4 Fig. Blind spectral analysis of Invitrogen Green-Green Beads. The beads are 6 microns in diameter and have different dyes in their core and shell. (a) Monochrome image of the beads. (b) False color spectral image of the beads. (c) First channel obtained by a NNMF spectral analysis. (d) Second channel (e) The spectra corresponding to the extracted channels. The image was collected with an EMCCD and filter configuration 1 (see section “System Dichroics and Emission Filters”).

S2.1 Movie. https://zenodo.org/record/7325050/files/S1_Movie.avi?download=1 Neuronal growth in a zebrafish embryo. Sensory neurons (green) are labeled with GFP and motor neurons (magenta) are labeled with mCherry. The video was captured with filter configuration 2 (see section "System Dichroics and Emission Filters") frames were taken every minute.

S2.2 Movie. https://zenodo.org/record/7325050/files/S2_Movie.avi?download=1 Video of mitosis in a live Xenopus laevis embryo. The cellular membranes (magenta) is labeled with mTagBFP::CAAX; chromatin (blue) is labeled with miRFP670::H2B; and mitotic spindles (green) are labeled with mCherry:α-tubulin. One frame of 75 ms exposure time was captured every 5 seconds. The video was captured with filter configuration 2 (see section "System Dichroics and Emission Filters").

Chapter 3 Supplemental Information

Resin Name	**Type**	**Why it was not tested**	**Sources**
Lowicryl HM20	Acrylic	More specialized setup than what we have. UV polymerization. Potentially not good fluorescence preservation.	[75,76]
Neutral Embedding Resin	Acrylic	Needed 4C temp environment, vacuum and completely dark conditions. Very niche formulation.	[77]
Unicryl	Acrylic	Only 50% fluorescence preservation.	[75,77]
Optimized GMA	Acrylic	Specialized setup with specific separation column.	[75]
Araldite	Epoxy	Hydrophobic resin that could mess with protein structure.	[78]
HPMA	Acrylic	Over 2 weeks penetration time for large samples (mouse brain).	[75]
Durcupan	Epoxy	80 C curing temp. Could cook the sample a bit.	[79]

Table S3.1: A mix of resins used in various literature were evaluated and subsequently were found to not fit the parameters necessary for the SETI system before testing. Corresponding papers are included for justification.

Chapter 4 Supplemental Information

Setup for the napari-live-flim plugin requires several steps (shown below).

1. OpenScan TCSPC module and all dependencies.
2. Verify FLIM electronics are compatible with OpenScan
3. Verify Python and these packages are present.
    a. FLIMLib (from github.com/flimlib)
    b. Napari package and all dependencies (from napari.org)
    c. Napari-live-flim (from github.com/uw-loci/napari-live-flim)
4. Operation
    a. In MicroManager, set a port number in the device property setting named **`OpenScanFLIM-BH-TCSPC-SendFLIMHistogramsToUDPPort`** (Fig. 9)
    b. Run **`receive_view_example.py [port]`** from the command line to run the napari-live-flim application and connect to OpenScan
5. Begin acquisition within MicroManager.
6. Interact with the FLIM data on the napari-viewer.
    a. Change FLIM fitting parameters using the options in the Lifetime Image window.
    b. Modify selections in the Lifetime Image and Phasor Plot windows.
    c. Click the `snap` button to take a snapshot.
    d. Use the scroll bar in the Lifetime Image to select specific snapshots.
7. Stop scanning at the MicroManager end to stop acquisition.

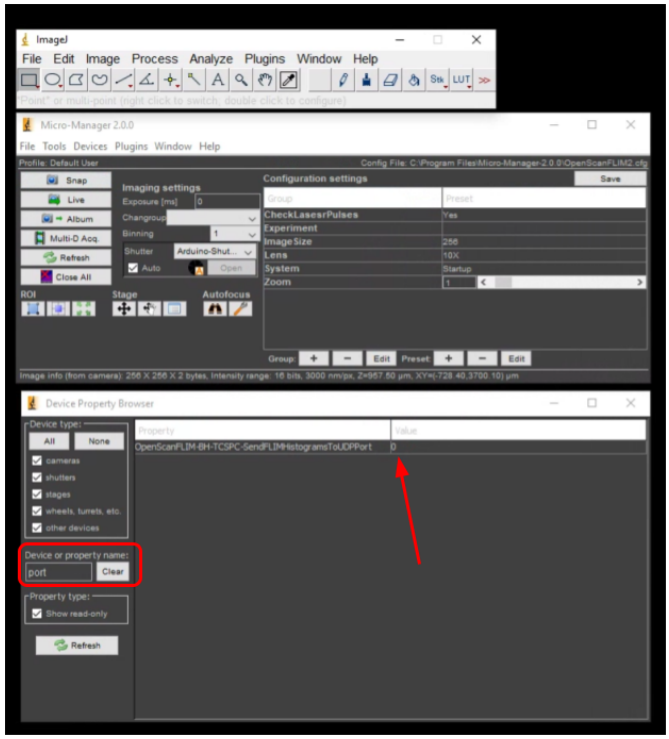

Figure S4.1. Screenshot of MicroManager showing how to set up FLIM data output

Data Availability Statement

The original contributions presented in the study are publicly available. The guidelines for usage with Openscan are provided in the Supplementary Material section.
The data can be found here:

- Example Dataset (for replay test)
- GitHub:
  - https://github.com/uw-loci/napari-live-flim
  - https://github.com/uw-loci/RT-FLIM
  - https://github.com/flimlib/flimlib
  - https://github.com/uw-loci/flimlib_python_examples

- Zenodo: https://doi.org/10.5281/zenodo.7261293
  - Video 1: Demonstration of Initializing napari-live-flim
  - Video 2: Demonstration of Real time Acquisition
  - Video 3:Demonstration of Replay of SPC file and visualization in napari-live-flim

- Additional resources:
  - https://pypi.org/project/flimlib/
  - https://www.napari-hub.org/plugins/napari-live-flim

Chapter 6 References

1. OpenScan – Laboratory for Optical and Computational Instrumentation [Internet]. [cited 2021 Aug 2]. Available from: https://eliceirilab.org/openscan/
2. Edelstein AD, Tsuchida MA, Amodaj N, Pinkard H, Vale RD, Stuurman N. Advanced methods of microscope control using μManager software. J Biol Methods. 2014;1(2):e10.
3. Edelstein A, Amodaj N, Hoover K, Vale R, Stuurman N. Computer Control of Microscopes Using μManager. Curr Protoc Mol Biol. 2010;92(1):14.20.1-14.20.17.
4. Rueden CT, Schindelin J, Hiner MC, DeZonia BE, Walter AE, Arena ET, et al. ImageJ2: ImageJ for the next generation of scientific image data. BMC Bioinformatics. 2017 Nov 29;18(1):529.
5. Schindelin J, Rueden CT, Hiner MC, Eliceiri KW. The ImageJ ecosystem: An open platform for biomedical image analysis. Mol Reprod Dev. 2015;82(7–8):518–29.
6. Fujita K, Nakamura O, Kaneko T, Oyamada M, Takamatsu T, Kawata S. Confocal multipoint multiphoton excitation microscope with microlens and pinhole arrays. Opt Commun. 2000 Jan 15;174(1):7–12.
7. Hecksher-Sørensen J, Sharpe J. 3D confocal reconstruction of gene expression in mouse. Mech Dev. 2001 Jan 1;100(1):59–63.
8. Wright SJ, Centonze VE, Stricker SA, DeVries PJ, Paddock SW, Schatten G. Chapter 1 Introduction to Confocal Microscopy and Three-Dimensional Reconstruction. In: Matsumoto B, editor. Methods in Cell Biology [Internet]. Academic Press; 1993 [cited 2022 Nov 6]. p. 1–45. (Cell Biologcal Applications of Confocal Microscopy; vol. 38). Available from: https://www.sciencedirect.com/science/article/pii/S0091679X0860998X
9. Berry MW, Browne M, Langville AN, Pauca VP, Plemmons RJ. Algorithms and applications for approximate nonnegative matrix factorization. Comput Stat Data Anal. 2007 Sep 15;52(1):155–73.
10. Demandolx D, Davoust J. Multicolour analysis and local image correlation in confocal microscopy. J Microsc. 1997;185(1):21–36.
11. Davis LM, Shen G. Extension of multidimensional microscopy to ultrasensitive applications with maximum-likelihood analysis. In: Three-Dimensional and Multidimensional Microscopy: Image Acquisition and Processing XIV [Internet]. International Society for Optics and Photonics; 2007 [cited 2021 Apr 14]. p. 64430N. Available from: https://www.spiedigitallibrary.org/conference-proceedings-of-spie/6443/64430N/Extension-of-multidimensional-microscopy-to-ultrasensitive-applications-with-maximum-likelihood/10.1117/12.702217.short
12. Juan A de, Maeder M, Hancewicz T, Tauler R. Use of local rank-based spatial information for resolution of spectroscopic images. J Chemom. 2008;22(5):291–8.
13. Yuheng S, Hao Y. Image Segmentation Algorithms Overview [Internet]. arXiv; 2017 [cited 2022 Nov 6]. Available from: http://arxiv.org/abs/1707.02051
14. Song Y, Yan H. Image Segmentation Techniques Overview. In: 2017 Asia Modelling Symposium (AMS). 2017. p. 103–7.
15. Ciritsis A, Boss A, Rossi C. Automated pixel-wise brain tissue segmentation of diffusion-weighted images via machine learning. NMR Biomed. 2018;31(7):e3931.
16. Heylen R, Parente M, Gader P. A Review of Nonlinear Hyperspectral Unmixing Methods. IEEE J Sel Top Appl Earth Obs Remote Sens. 2014 Jun;7(6):1844–68.
17. Bhatt JS, Joshi MV. Deep Learning in Hyperspectral Unmixing: A Review. In: IGARSS 2020 - 2020 IEEE International Geoscience and Remote Sensing Symposium. 2020. p. 2189–92.
18. Schindelin J, Arganda-Carreras I, Frise E, Kaynig V, Longair M, Pietzsch T, et al. Fiji: an open-source platform for biological-image analysis. Nat Methods. 2012 Jul;9(7):676–82.
19. Wood D, Feke G, Vizard D, Papineni R. Refining epifluorescence imaging and analysis

with automated multiple-band flat-field correction. Nat Methods. 2008 Apr;5(4):i–ii.
20. Boyle RP, Janusz R, Laugalys V, Philip AGD. CCD Flatfield Correction by Differential Stellar Photometry: Automated Methods. 2003 Dec 1;203:04.02.
21. Karadaglić D, Wilson T. Image formation in structured illumination wide-field fluorescence microscopy. Micron. 2008 Oct 1;39(7):808–18.
22. Neil M a. A, Juškaitis R, Wilson T. Method of obtaining optical sectioning by using structured light in a conventional microscope. Opt Lett. 1997 Dec 15;22(24):1905–7.
23. Rueden CT, Hiner MC, Evans EL, Pinkert MA, Lucas AM, Carpenter AE, et al. PyImageJ: A library for integrating ImageJ and Python. Nat Methods. 2022 Nov;19(11):1326–7.
24. MATLAB [Internet]. The Mathworks, Inc.; 2021. Available from: https://www.mathworks.com/products/matlab.html
25. Schroeder AB, Dobson ETA, Rueden CT, Tomancak P, Jug F, Eliceiri KW. The ImageJ ecosystem: Open-source software for image visualization, processing, and analysis. Protein Sci. 2021;30(1):234–49.
26. Hiner MC, Rueden CT, Eliceiri KW. ImageJ-MATLAB: a bidirectional framework for scientific image analysis interoperability. Bioinformatics. 2017 Feb 15;33(4):629–30.
27. Luo T, Deng L, Li A, Zhou C, Shao S, Sun Q, et al. Scalable Resin Embedding Method for Large-Volume Brain Tissues with High Fluorescence Preservation Capacity. iScience. 2020 Oct 20;23(11):101717.
28. Li C, Risnes S. A comparison of resins for embedding teeth, with special emphasis on adaptation to enamel surface as evaluated by scanning electron microscopy. Arch Oral Biol. 2004 Jan 1;49(1):77–83.
29. Carlemalm E, Garavito RM, Villiger W. Resin development for electron microscopy and an analysis of embedding at low temperature*. J Microsc. 1982;126(2):123–43.
30. Gros O, Maurin LC. Easy flat embedding of oriented samples in hydrophilic resin (LR White) under controlled atmosphere: Application allowing both nucleic acid hybridizations (CARD-FISH) and ultrastructural observations. Acta Histochem. 2008 Sep 8;110(5):427–31.
31. Sullivan-Brown J, Bisher ME, Burdine RD. Embedding, Serial Sectioning and Staining of Zebrafish Embryos Using JB-4™ Resin. Nat Protoc. 2011 Jan;6(1):46–55.
32. Sordillo LA, Pu Y, Pratavieira S, Budansky Y, Alfano RR. Deep optical imaging of tissue using the second and third near-infrared spectral windows. J Biomed Opt. 2014 May;19(5):056004.
33. Lemercier N, Middel V, Hentsch D, Taubert S, Takamiya M, Beil T, et al. Microtome-integrated microscope system for high sensitivity tracking of in-resin fluorescence in blocks and ultrathin sections for correlative microscopy. Sci Rep. 2017 Oct 19;7(1):13583.
34. Bacon JR, Crain JS, Vaeck LV, Williams JG. Atomic mass spectrometry. J Anal At Spectrom. 1999 Jan 1;14(10):1633–59.
35. Hu J, Yang P, Hou X. Atomic spectrometry and atomic mass spectrometry in bioanalytical chemistry. Appl Spectrosc Rev. 2019 Mar 16;54(3):180–203.
36. Digman MA, Gratton E. The phasor approach to fluorescence lifetime imaging: Exploiting phasor linear properties. :14.
37. Digman MA, Caiolfa VR, Zamai M, Gratton E. The Phasor Approach to Fluorescence Lifetime Imaging Analysis. Biophys J. 2008 Jan 15;94(2):L14–6.
38. Liao SC, Sun Y, Coskun U. FLIM Analysis using the Phasor Plots. :13.
39. Ballew RM, Demas JN. An error analysis of the rapid lifetime determination method for the evaluation of single exponential decays. Anal Chem. 1989 Jan 1;61(1):30–3.
40. Sharman KK, Periasamy A, Ashworth H, Demas JN. Error Analysis of the Rapid Lifetime Determination Method for Double-Exponential Decays and New Windowing Schemes. Anal Chem. 1999 Mar 1;71(5):947–52.

41. Silva SF, Domingues JP, Morgado AM. Can we use rapid lifetime determination for fast, fluorescence lifetime based, metabolic imaging? Precision and accuracy of double-exponential decay measurements with low total counts. PLOS ONE. 2019 May 14;14(5):e0216894.
42. Wong C, Chen AA, Behr B, Shen S. Time-lapse microscopy and image analysis in basic and clinical embryo development research. Reprod Biomed Online. 2013 Feb 1;26(2):120–9.
43. Heo YJ, Lee D, Kang J, Lee K, Chung WK. Real-time Image Processing for Microscopy-based Label-free Imaging Flow Cytometry in a Microfluidic Chip. Sci Rep. 2017 Sep 14;7(1):11651.
44. Zhu X, Zhang D. Efficient Parallel Levenberg-Marquardt Model Fitting towards Real-Time Automated Parametric Imaging Microscopy. PLOS ONE. 2013 Oct 10;8(10):e76665.
45. Brun E, Defour D, de Oliveira Castro P, Iştoan M, Mancusi D, Petit E, et al. A Study of the Effects and Benefits of Custom-Precision Mathematical Libraries for HPC Codes. IEEE Trans Emerg Top Comput. 2021 Jul;9(3):1467–78.
46. Gerritsen HC, Agronskaia AV, Bader AN, Esposito A. Chapter 3 Time domain FLIM: Theory, instrumentation, and data analysis. In: Laboratory Techniques in Biochemistry and Molecular Biology [Internet]. Elsevier; 2009 [cited 2021 Dec 1]. p. 95–132. (Fret and Flim Techniques; vol. 33). Available from: https://www.sciencedirect.com/science/article/pii/S007575350800003X
47. Kerkhoff Y, Wedepohl S, Nie C, Ahmadi V, Haag R, Block S. A fast open-source Fiji-macro to quantify virus infection and transfection on single-cell level by fluorescence microscopy. MethodsX. 2022 Jan 1;9:101834.
48. Wershof E, Park D, Barry DJ, Jenkins RP, Rullan A, Wilkins A, et al. A FIJI macro for quantifying pattern in extracellular matrix. Life Sci Alliance [Internet]. 2021 Mar 1 [cited 2022 Nov 5];4(3). Available from: https://www.life-science-alliance.org/content/4/3/e202000880
49. Ouyang W, Mueller F, Hjelmare M, Lundberg E, Zimmer C. ImJoy: an open-source computational platform for the deep learning era. Nat Methods. 2019 Dec;16(12):1199–200.
50. Pietzsch T, Preibisch S, Tomančák P, Saalfeld S. ImgLib2—generic image processing in Java. Bioinformatics. 2012 Nov 15;28(22):3009–11.
51. Pietzsch T, Saalfeld S, Preibisch S, Tomancak P. BigDataViewer: visualization and processing for large image data sets. Nat Methods. 2015 Jun;12(6):481–3.
52. Pedregosa F, Varoquaux G, Gramfort A, Michel V, Thirion B, Grisel O, et al. Scikit-learn: Machine Learning in Python. J Mach Learn Res [Internet]. 2011 Oct 12 [cited 2021 Mar 31]; Available from: https://hal.inria.fr/hal-00650905
53. Arganda-Carreras I, Kaynig V, Rueden C, Eliceiri KW, Schindelin J, Cardona A, et al. Trainable Weka Segmentation: a machine learning tool for microscopy pixel classification. Bioinformatics. 2017 Aug 1;33(15):2424–6.
54. Bray MA, Carpenter AE. Quality Control for High-Throughput Imaging Experiments Using Machine Learning in Cellprofiler. In: Johnston PA, Trask OJ, editors. High Content Screening: A Powerful Approach to Systems Cell Biology and Phenotypic Drug Discovery [Internet]. New York, NY: Springer; 2018 [cited 2021 Nov 23]. p. 89–112. (Methods in Molecular Biology). Available from: https://doi.org/10.1007/978-1-4939-7357-6_7
55. Chauhan S, Rühaak W, Khan F, Enzmann F, Mielke P, Kersten M, et al. Processing of rock core microtomography images: Using seven different machine learning algorithms. Comput Geosci. 2016 Jan 1;86:120–8.
56. Ding Y, Suffren S, Bellec P, Lodygensky GA. Supervised machine learning quality control for magnetic resonance artifacts in neonatal data sets. Hum Brain Mapp. 2019;40(4):1290–7.

57. Theriault DH, Walker ML, Wong JY, Betke M. Cell morphology classification and clutter mitigation in phase-contrast microscopy images using machine learning. Mach Vis Appl. 2012 Jul 1;23(4):659–73.
58. Usman K, Rajpoot K. Brain tumor classification from multi-modality MRI using wavelets and machine learning. Pattern Anal Appl. 2017 Aug 1;20(3):871–81.
59. Zacharaki EI, Wang S, Chawla S, Soo Yoo D, Wolf R, Melhem ER, et al. Classification of brain tumor type and grade using MRI texture and shape in a machine learning scheme. Magn Reson Med. 2009;62(6):1609–18.
60. Albarqouni S, Baur C, Achilles F, Belagiannis V, Demirci S, Navab N. AggNet: Deep Learning From Crowds for Mitosis Detection in Breast Cancer Histology Images. IEEE Trans Med Imaging. 2016 May;35(5):1313–21.
61. Albert O, Sherman L, Mourou G, Norris TB, Vdovin G. Smart microscope: an adaptive optics learning system for aberration correction in multiphoton confocal microscopy. Opt Lett. 2000 Jan 1;25(1):52–4.
62. Scherf N, Huisken J. The smart and gentle microscope. Nat Biotechnol. 2015 Aug;33(8):815–8.
63. Huang B, Li Z, Li J. An artificial intelligence atomic force microscope enabled by machine learning. Nanoscale. 2018 Nov 22;10(45):21320–6.
64. Nankivil D, Dhalla AH, Gahm N, Shia K, Farsiu S, Izatt JA. Coherence revival multiplexed, buffered swept source optical coherence tomography: 400 kHz imaging with a 100 kHz source. Opt Lett. 2014 Jul 1;39(13):3740–3.
65. Carrasco-Zevallos OM, Qian R, Gahm N, Migacz J, Toth CA, Izatt JA. Long working distance OCT with a compact 2f retinal scanning configuration for pediatric imaging. Opt Lett. 2016 Nov 1;41(21):4891–4.
66. SolidWorks [Internet]. BIOVIA, Dassault Systèmes; 2021. Available from: https://www.3ds.com/products-services/solidworks/
67. Konda PC, Konda PC, Loetgering L, Loetgering L, Loetgering L, Zhou KC, et al. Fourier ptychography: current applications and future promises. Opt Express. 2020 Mar 30;28(7):9603–30.
68. Ou X, Horstmeyer R, Zheng G, Yang C. High numerical aperture Fourier ptychography: principle, implementation and characterization. Opt Express. 2015 Feb 9;23(3):3472–91.
69. Tian L, Li X, Ramchandran K, Waller L. Multiplexed coded illumination for Fourier Ptychography with an LED array microscope. Biomed Opt Express. 2014 Jul 1;5(7):2376–89.
70. Yeh LH, Dong J, Zhong J, Tian L, Chen M, Tang G, et al. Experimental robustness of Fourier ptychography phase retrieval algorithms. Opt Express. 2015 Dec 28;23(26):33214–40.
71. Bolstad WM, Curran JM. Introduction to Bayesian Statistics. John Wiley & Sons; 2016. 617 p.
72. Gelman A, Shalizi CR. Philosophy and the practice of Bayesian statistics. Br J Math Stat Psychol. 2013;66(1):8–38.
73. Caelen O. A Bayesian interpretation of the confusion matrix. Ann Math Artif Intell. 2017 Dec 1;81(3):429–50.
74. Shankar PM. Pedagogy of Bayes' rule, confusion matrix, transition matrix, and receiver operating characteristics. Comput Appl Eng Educ. 2019;27(2):510–8.
75. Yang Z, Hu B, Zhang Y, Luo Q, Gong H. Development of a Plastic Embedding Method for Large-Volume and Fluorescent-Protein-Expressing Tissues. PLOS ONE. 2013 Apr 5;8(4):e60877.
76. Gang Y, Liu X, Wang X, Zhang Q, Zhou H, Chen R, et al. Plastic embedding immunolabeled large-volume samples for three-dimensional high-resolution imaging. Biomed Opt Express. 2017 Jul 10;8(8):3583–96.

77. Zhou H, Gang Y, Chen S, Wang Y, Xiong Y, Li L, et al. Development of a neutral embedding resin for optical imaging of fluorescently labeled biological tissue. J Biomed Opt. 2017 Oct;22(10):106015.
78. Richardson KC, Jarett L, Finke EH. Embedding in Epoxy Resins for Ultrathin Sectioning in Electron Microscopy. Stain Technol. 1960 Jan;35(6):313–23.
79. Dzurjašková Z, Blaško J, Tomori Z, Vanický I. A method to prepare large resin sections for counting myelinated axons in rodent CNS and PNS structures. Neurosci Lett. 2021 Apr 17;750:135767.